Stereoscopic Observations of Solar Radio Emissions by the S/Waves Instrument onboard the STEREO Spacecraft

Vratislav Krupař

Jointly Supervised PhD between

Charles University in Prague
Faculty of Mathematics and Physics

And

L'Observatoire de Paris
École Doctorale Astronomie et Astrophysique
d'Île-de-France

Thesis

Stereoscopic Observations of Solar Radio Emissions by the S/Waves Instrument onboard the STEREO Spacecraft

Vratislav Krupař

Directors of the thesis:

Charles University in Prague	*Paris Observatory*
Ondřej Santolík	Milan Maksimovic

Jury:	Benoit Mosser	(President)
	Säm Krucker	(Reviewer)
	Robert Wimmer-Schweingruber	(Reviewer)
	Baptiste Cecconi	(Examiner)
	František Němec	(Examiner)
	Jan Souček	(Examiner)
	Milan Maksimovic	(Co-Director)
	Ondřej Santolík	(Co-Director)

PhD Thesis

Stereoscopic Observations of Solar Radio Emissions by the S/Waves Instrument onboard the STEREO Spacecraft

Vratislav Krupař

Directors of the thesis:

Charles University in Prague
Ondřej Santolík

Paris Observatory
Milan Maksimovic

Title Stereoscopic Observations of Solar Radio Emissions by the S/Waves Instrument onboard the STEREO Spacecraft

Abstract This PhD thesis is primarily dedicated to a study of type III radio bursts observed by the S/Waves instrument onboard Solar TErrestrial RElations Observatory (STEREO). These emissions are produced by beams of suprathermal electrons escaping the corona along open magnetic field lines during increased solar activity. As fast electrons propagate in the interplanetary (IP) medium, Langmuir waves are generated at the local electron plasma frequency f_{pe} by a bump-on-tail instability and can be afterwards converted by a non-linear process into radio emissions at f_{pe} and/or $2f_{pe}$: type III radio bursts.
We have developed a goniopolarimetric (GP, also referred to as direction-finding) inversion using the Singular Value Decomposition (SVD) technique for electric measurements on three non-orthogonal antennas. It allows us to retrieve both wave vector directions and polarization properties of incident waves. We have also investigated the influence of extended sources (as a typical feature of type III radio bursts) on measured spectral matrices. We have found an empirical relation between apparent source sizes and spectral matrices decomposed by SVD. Abovementioned techniques have been extensively tested on data obtained by the High Frequency Receiver (HFR, a part of S/Waves). We have compared flux densities and GP products of several intense radio bursts observed simultaneously by the two STEREO spacecraft and the *Wind* spacecraft (using the spin demodulation method for the GP inversion) during small separation distances with satisfactory results.
We have performed statistical analysis of a large number of type III radio bursts observed by STEREO between May 2007 and September 2011. Only intense, simple, and isolated cases have been included in our data set. We have found that the maximum flux density occurs around 1 MHz. The apparent source size is very extended ($\sim$ 40°) for frequencies above 500 kHz while remaining almost constant ($\sim$ 25°) between 500 kHz and 2 MHz. Calculated positions of radio sources suggest that scattering of the primary beam pattern plays an important role in the propagation of type III radio bursts in the IP medium.

Keywords Solar radio emissions – Goniopolarimetric inversion

Název Stereoskopická pozorování slunečních rádiových emisí přístrojem S/Waves na družicích STEREO

Abstrakt Tato dizertační práce je věnována studiu slunečních rádiových emisí typu III pozorovaných přístrojem S/Waves na družicích projektu Solar TErrestrial RElations Observatory (STEREO). Tyto rádiové emise jsou generovány svazky horkých elektronů unikajících z koróny během zvýšené sluneční aktivity. Tyto elektronové svazky excitují v meziplanetárním prostoru elektrostatické Langmuirovy vlny na lokální elektronové frekvenci f_{pe} díky „bump-on-tail" nestabilitě. Langmuirovy vlny mohou být konvertovány na rádiové emise typu III na frekvenci f_{pe} anebo $2f_{pe}$.
Za pomoci metody singulárního rozkladu (SVD) jsme vyvinuli goniopolarimetrickou (GP) inverzi pro měření elektrického pole na obecně neortogonálních anténách. Tato inverze nám poskytuje jak směr vlnového vektoru tak polarizační vlastnosti příchozí vlny. Rovněž jsme prozkoumali vliv velikostí rádiových zdrojů (jež jsou typické pro rádiové emise typu III) na spektrální matice. Nalezli jsme empirický vztah mezi velikostí zdroje a rozloženou spektrální maticí za pomocí SVD. Výše zmíněné metody byly použity na datech naměřených vlnovým analyzátorem HFR (High Frequency Receiver, část přístroje S/Waves). Porovnali jsme spektrální výkony a výsledky GP analýzy několika intenzivních rádiových emisí typu III pozorovaných na družicích STEREO a *Wind* (jež používá pro GP analýzu spinovou demodulaci) při vzájemně malých vzdálenostech.
Provedli jsme statistickou analýzu velkého množství rádiových emisí typu III pozorovaných družicemi STEREO v období od května 2007 do září 2011. Do našeho datového souboru jsme zahrnuli pouze intenzivní, jednoduché a izolované případy. Zjistili jsme, že maximální spektrální výkon se vyskytuje na frekvenci okolo 1 MHz. Velikost zdrojů je velmi rozšířená ($\sim$ 40°) pro frekvence pod 500 kHz, zatímco zůstává konstantní ($\sim$ 25°) mezi 500 kHz a 2 MHz. Nalezené pozice rádiových zdrojů potvrzují, že rozptyl primárního paprsku hraje důležitou roli v šíření rádiových emisí typu III v meziplanetárním prostoru.
Klíčová slova Sluneční rádiové emise, Goniopolarimetrie

Titre Etude stéréoscopique des émissions radio solaires avec l'instrument S/WAVES embarqué sur les sondes STEREO

Résumé Cette thèse est principalement consacrée à une étude des sursauts radio de type III observés par l'instrument S/Waves à bord du satellite Solar TErrestrial RElations Observatory (STEREO). Ces émissions sont produites lors de périodes d'activité solaire accrue par des faisceaux d'électrons suprathermiques s'échappant de la couronne solaire le long de lignes de champ magnétique ouvertes. Lorsque des électrons rapides se propagent dans le milieu interplanétaire (IP), des ondes de Langmuir sont générées à la fréquence plasma locale des électrons f_{pe} par une instabilité dite «bump-on-tail». Ces instabilités peuvent ensuite être converties par un processus non-linéaire en des émissions radio à f_{pe} et/ou à $2f_{pe}$: les sursauts radio de type III.
Nous avons développé une méthode d'inversion goniopolarimétrique (GP, aussi appelée «direction-finding») en utilisant la technique de décomposition en valeurs singulières (SVD) appliquée aux mesures des trois antennes électriques non-orthogonales. Elle nous permet de retrouver la direction du vecteur d'onde des ondes radio de Type III ainsi que leur propriétés de polarisation. Nous avons également étudié l'influence des sources étendues (qui sont caractéristiques des sursauts radio de type III) sur les matrices spectrales mesurées. Nous avons trouvé une relation empirique entre la taille des sources apparentes et les matrices spectrales décomposées par SVD. Les techniques précitées ont été largement testées sur des données obtenues par le receveur haute fréquence (HFR, une composante de l'instrument S/Waves). Nous avons comparé des densités de flux et des produits GP de plusieurs sursauts radio intenses observés simultanément par les satellites STEREO et *Wind* (en utilisant la méthode de démodulation de spin pour l'inversion GP), lorsque ceux-ci étaient proches, avec des résultats satisfaisants.
Nous avons réalisé une analyse statistique d'un grand nombre de sursauts radio de type III observées par STEREO entre mai 2007 et Septembre 2011. Seuls les cas intenses, simples, et isolés ont été inclus dans notre ensemble de données. Nous avons constaté que la densité de flux maximale se produit autour de 1 MHz. La taille apparente de la source est très étendue ($\sim 40°$) pour les fréquences inférieures à 500 kHz tout en restant à peu près constante ($\sim 25°$) entre 500 kHz et 2 MHz. Les positions calculées des sources radio suggèrent que la diffusion de la configuration primaire du faisceau joue un rôle important dans la propagation de sursauts radio de type III dans l'environnement IP.
Mots-clés Sursauts radio solaires, Goniopolarimétrie

Contents

List of Figures

List of Tables

List of Abbreviations

AKR Auroral Kilometric Radiation

AR Active Region

AU Astronomical Unit

CDPP Centre de Données de la Physique des Plasmas

CIR Corotating Interaction Region

CME Coronal Mass Ejection

DAM Nançay Decameter Array

DF Direction Finding

EDF Electron Distribution Function

ESA European Space Agency

GP Gonipolarimetric

HEE Heliocentric Earth Ecliptic

HEEQ Heliocentric Earth Equatorial

HFR High Frequency Receiver

IMF Interplanetary Magnetic Field

IP Interplanetary

NASA National Aeronautics and Space Administration

NRT Nançay Radioheliograph

QTN Quasi-Thermal Noise

RPW Radio and Plasma Wave

RTN Radial-Tangential-Normal

SECCHI Sun Earth Connection Coronal and Heliospheric Investigation

SDO Solar Dynamic Observatory

SNR Signal-to-Noise Ratio

STEREO Solar TErrestrial RElations Observatory

SVD Singular Value Decomposition

WL White-Light

Preface

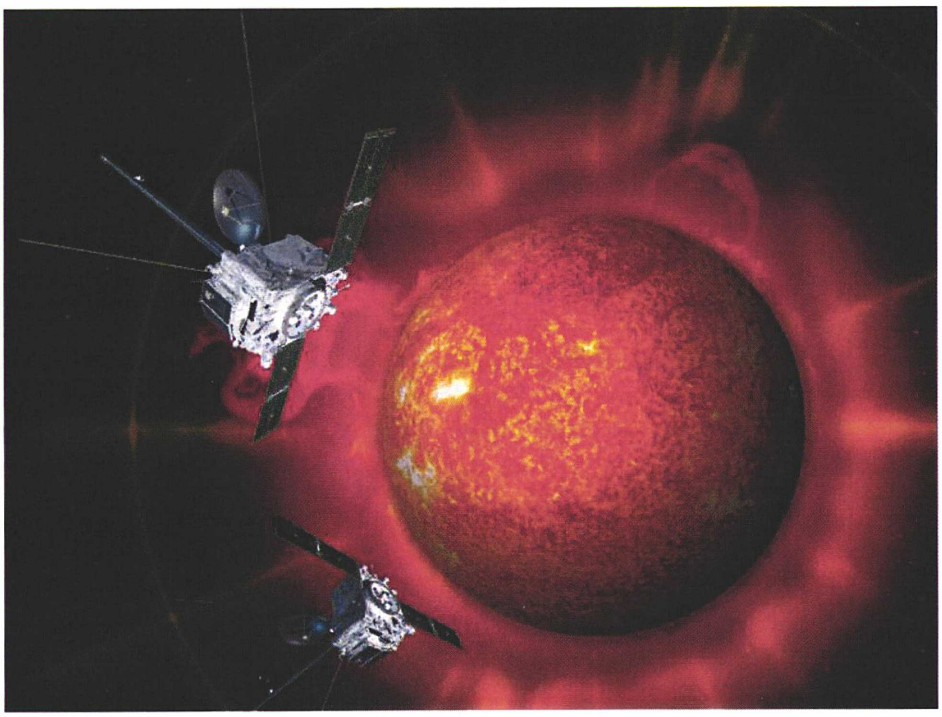

Figure 1: Artist's impression of the STEREO spacecraft and the Sun. Adapted from `http://stereo.gsfc.nasa.gov/`.

The Sun fascinates mankind since its very beginning. Although our closest star has been studied for thousands of years, many questions still remain without answers (*e.g.* the solar dynamo and tachoclines). Our desire for a better understanding of processes associated with the Sun and new available technologies cause that solar physics experiences a strong development during last decades. Comparing to other stars the Sun's proximity to the planet Earth allows us to perform complex investigations of processes forming the stellar life.
The main goal of this thesis is a study of type III radio bursts using measurements of the S/Waves instruments onboard the Solar TErrestrial RElations Observatory (STEREO).

Type III radio bursts belong among the most intense electromagnetic emissions in the heliosphere and can be observed from tens of kHz up to several GHz on time scales from seconds up to hours. They are thought to be generated by beams of suprathermal electrons ($\sim$ 0.1c) accelerated near the Sun's surface streaming outward in the solar corona and in the Interplanetary (IP) medium on the open magnetic field lines associated with solar flares. This abrupt change of plasma parameters can lead to generation of electrostatic Langmuir waves at the local plasma frequency f_p which is proportional to the electron density. These waves can be afterward converted into electromagnetic waves either at f_p (the fundamental emission, F) or $2f_p$ (the harmonic emission, H): type III radio bursts. As type III radio burst triggering electron beams propagate outward from the Sun, emissions are generated at lower frequencies corresponding to a radial decrease of f_p.
The investigation of type III radio bursts is interesting for the scientific community for several particular reasons. Type III radio bursts provide us with information on properties of the solar corona and the IP space at inaccessible distances from the Sun by spaceborne instruments. In a comparison with other electromagnetic emissions, they have very extended apparent sources, which can be explained by either properties of an intrinsic beaming pattern or by scattering density fluctuations of the IP medium. Hence their apparent source sizes can potentially yield important information about density fluctuations when scattering of a primary beam pattern is considered. Moreover understanding of generation mechanisms of type III radio bursts may bring new insights to wave-particle interactions with applications in laboratory plasmas. Although type III radio bursts have been discovered more than 60 years ago many questions on their properties still remain without answer due to missing *in situ* measurements at distances closer to the Sun and difficulties in proper interpretations of existing observations.
We have studied type III radio bursts using data measured by STEREO which consists of two identical spacecraft orbiting the Sun providing us for the first time with a unique stereoscopic view of the Solar-Terrestrial system (Figure 1). The STEREO spacecraft have been launched on October 26, 2006 and after series of highly eccentric Earth orbits followed by close flybys of the moon they escaped into orbits about the Sun near 1 AU in the ecliptical plane. STEREO-A moves ahead of the Earth whereas STEREO-B trails behind. The two STEREO separate at $\sim 45°$ per year with respect to the Sun. In February 2011 the separation angle reached 180° providing us with a 360° view of the Sun for the first time. Below we summarize the main scientific objectives of STEREO (*Kaiser et al.*, 2008):

- Understanding of the causes and mechanisms of Coronal Mass Ejection (CME) initiation.
- Characterization of the propagation of CMEs through the heliosphere.
- Discovery of the mechanisms and sites of solar energetic particle acceleration in the low corona and the IP medium.
- Development of a 3-D, time-dependent model of the magnetic topology, temperature, density and velocity structure of the ambient solar wind.

While previous solar spacecraft were all spinning stabilized (ISEE-3, Ulysses, Wind, etc.), STEREO is the first three-axis stabilized solar mission. On the top of that the STEREO/Waves instrument onboard provides us with the Gonipolarimetric (GP) measurements encompassing both the Direction Finding (DF) and polarization which is needed for a comprehensive electromagnetic waves analysis. It allows us to investigate not only flux densities of solar radio emissions but we can localize their radio sources including apparent source sizes.

For a GP inversion of the STEREO/Waves data we have extended the the Singular Value Decomposition (SVD) analysis by (*Santolík et al.*, 2003) to electric field measurements performed on generally non-orthogonal antennas. We have studied an impact of extended sources on a polarization ellipsoid geometry. We have found an empirical relation between apparent source sizes and decomposed spectral matrices for various source shapes and polarization states. The aforementioned method has been applied on type III radio bursts observed by the High Frequency Receiver (HFR) which is a part of the S/Waves instrument onboard. We have compared our results with measurements of the Waves instrument (using a spin modulation methods for the GP analysis) embarked by the *Wind* spacecraft during short separation distances in an early phase of the STEREO mission (May 2007). The obtained GP products from HFR are planned to be archived in Centre de Données de la Physique des Plasmas (CDPP) which is the French national data center for natural plasmas of the solar system (`http://cdpp.cesr.fr/`).

Using extensive simulations we have investigated the influence of an antenna tilt to the GP inversion for the future Solar Orbiter mission. We have confirmed that the GP analysis will be possible by the RPW instrument.

We have performed statistical analysis of 156 simple and isolated type III radio bursts observed by STEREO between May 2007 and September 2011 The maximum flux density occurs ~ 1 MHz corresponding to radio sources located at ~ 8 $R_\odot$ and ~ 14 $R_\odot$ from the Sun for the F and H component, respectively. The apparent source size is statistically very extended (up to $\sim 40°$) suggesting that a scattering of the primary beam pattern is important in the propagation of type III radio bursts in the IP medium.

Plan of the Thesis

Chapter 1 presents a general introduction to solar physics. We focus on solar activity and its radio signatures with an emphasis on type III radio bursts.

Chapter 2 contains principles of radio astronomy at kilometric wavelengths and the SVD inversion of magnetic measurements.

Chapter 3 contains an application of the SVD method to radio sources. It includes an empirical relation for apparent source sizes, HFR data processing and comparison between STEREO and *Wind* measurements.

Chapter 4 is dedicated to a study of solar radio emissions by the S/Waves instrument. Three examples of type III radio burst observations are followed by a statistical survey. We also present a type II radio burst associated with a CME — CME interaction.

Chapter 5 summarizes our results presented in this thesis.

Appendix A contains four articles related to this thesis. Two of them have been published in the impacted journals (Journal of Geophysical Research and the Astrophysical Journal). Coordinate systems used in this thesis are described in Appendix B.

Chapter 1

Introduction

Contents

This chapter contains a brief introduction to solar physics with a special attention to type III radio bursts. A short description of the Sun and its atmosphere is followed by a discussion on the solar activity and its radio signatures. Finally, we summarize the currently known facts about the type III radio bursts.

1.1 The Sun and the Solar Wind

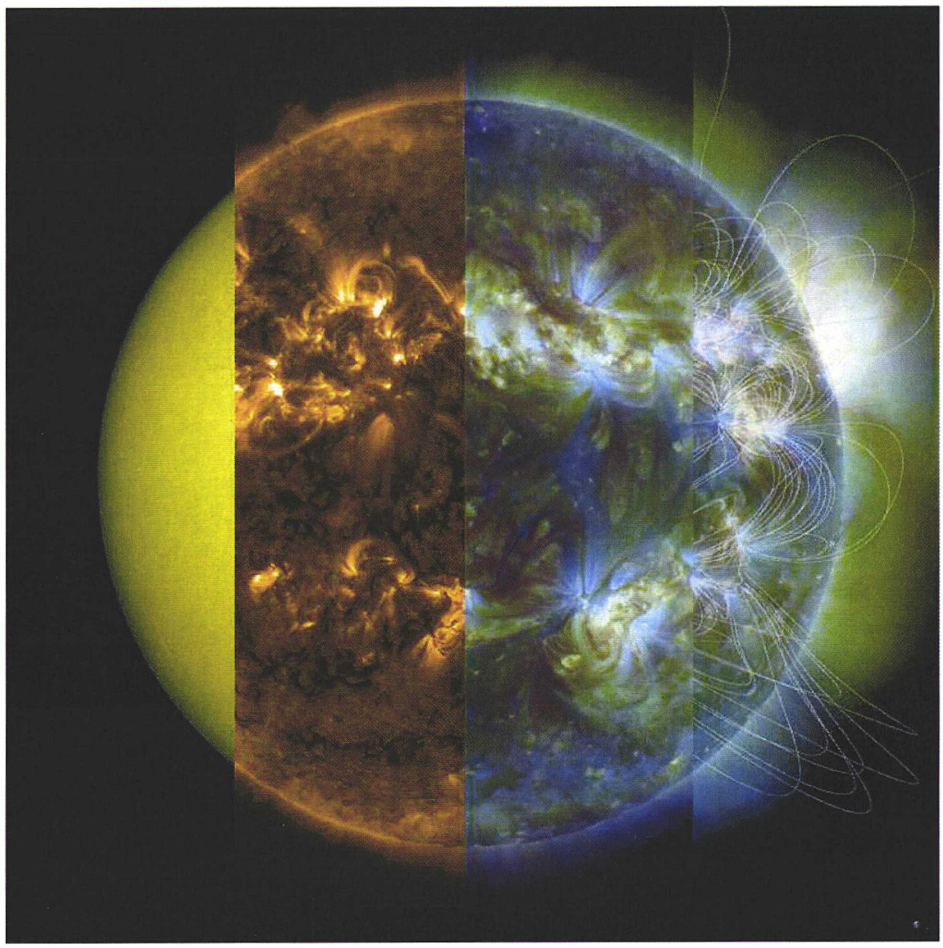

Figure 1.1: Observation of the Sun in various wavelengths recorded by SDO on December 7, 2011. Adapted from `http://sdo.gsfc.nasa.gov/`.

Being the central body of our solar system, the Sun (Figure 1.1) exerts a significant influence on many aspects of the human environment. A comprehensive investigation of solar activity variations in the heliosphere are important not only for better understanding of processes in plasma physics, but also for space weather forecasting in a vicinity of the planet Earth. Table 1.1 summarizes its basic properties.

Structure of the Sun

The Sun is composed of two global regions: the interior and the solar atmosphere. These domains have substantially different properties being divided in layers where both density and temperature change abruptly (Figure 1.2). We may divide the interior of the Sun into three layers: the core, the radiative zone, and the convective

Radius	$r_\odot = 696,000$ km
Mass	$M_\odot = 1.99 \times 10^{31}$ kg
Luminosity	$L_\odot = 3.86 \times 10^{23}$ kW
Magnetic field	
general	10^{-4} T
protuberance	10^{-3} — 10^{-2} T
sunspot	3×10^{-1} T
Temperature	
core	15,000,000 K
photosphere	5780 K
sunspot	4200 K
chromosphere	800,000 K

Table 1.1: Properties of the Sun. Adapted from *Kallenrode* (2004).

zone. The extremely dense and hot solar core holds more than half of the Sun's mass while filling only about 1.5% of its volume. In this layer a nuclear fusion takes a place by combining hydrogen nuclei into helium one while releasing vast amount of energy by a conversion of mass into radiation. The next layer is the radiative zone where energy is transported by a radiative diffusion: γ photons lose their energy and increase wavelength by a multiple absorption and re-emission. Above the radiative layer there is the convective layer where the temperature decreases and energy is transported outward mainly by a convection. A plasma circulation in the convective layer generates significant magnetic field which may emerge on the Sun's surface forming sunspots and solar flares.

Solar Atmosphere

The solar atmosphere consists of the photosphere, chromosphere, transition region, corona, and solar wind. The photosphere produces most of visible light being almost the coolest layer with temperature $\sim$ 6000 K. Periodically large magnetic field bundles may break up through this layer and create cool, dark regions known as sunspots. The chromosphere is located above the photosphere being transparent to most visible radiation. The transition region is characterized by a large gradient of temperature and density between rather dense and cold chromosphere and hot and sparse corona. The corona is the part of the solar atmosphere with extremely high temperatures. A coronal heating mechanism is still under debate, however a scenario favored today highlights a crucial role of the magnetic field. At a distance of $0.5 - 1$ $R_\odot$ above the photosphere a topology of magnetic field lines changes from mostly closed to the open one. Moreover the hydrostatic equilibrium breaks down and the corona produces a stream of charged particles escaping the upper atmosphere of the Sun: the solar wind.

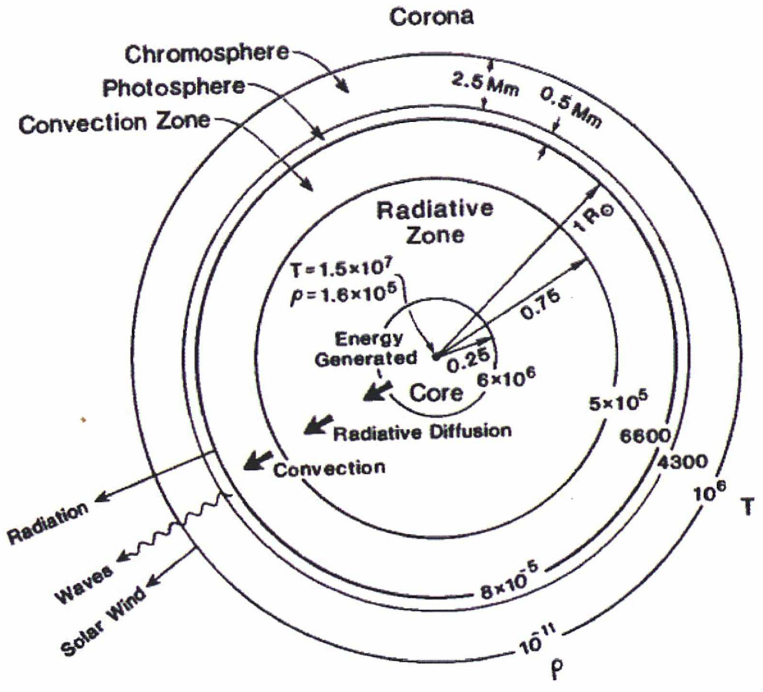

Figure 1.2: Structure of the Sun. Adapted from *Kivelson and Russell* (1995).

The Solar Wind

The solar wind is an outward flow of hot collisionless plasma ($\sim 10^5$ K) of Sun's origin filling the IP medium. *Parker* (1958) has proposed a gas dynamic model of solar wind which remains valid until these days. This model assumes that the outflow must be steady, spherically symmetric and isothermal. Thereafter an existence of the solar wind has been confirmed by Soviet spacecraft Luna-1 and Luna-2 in 1959. We may distinguish two components of the solar wind: the slow solar wind and fast solar wind. During solar minima the slow solar wind ($\sim$ 400 km/s, 1.6×10^6 K) originates mostly from a region around the solar equator along closed magnetic field lines and the fast solar wind ($\sim$ 800 km/s, 8×10^5 K) streams from coronal holes at higher latitudes along open magnetic lines. The solar wind is very dynamic medium reflecting processes occurring in the Sun. Hence during solar maxima the slow solar wind may originates at higher latitutes and vice versa. As the solar wind is a flow of collisionless charged particles it carries solar magnetic field frozen into the plasma. This magnetic field is then curved due to a combined motion of the outflow and solar sidereal rotation into the Archimedean spiral or hereafter the Parker spiral. The space filled with the solar wind is called the heliosphere extending up to $\sim$ 200 AU.

1.2 Solar Activity and its Radio Signatures

As the Sun is an active star it demonstrates its activity in various spatial and temporal scales (*Kivelson and Russell*, 1995). The most obvious periodic phenomena is the solar "sunspot" cycle lasting approximately 22 years. The sunspots are dark regions with temperatures of 2000 K lower than the surroundings, where the magnetic field from the convective layer emerge on the Sun's surface (Table 1.1). The sunspots usually appear in pairs with opposite polarities at latitudes of $\sim 30°$ both in the northern and southern hemispheres moving towards the equator where they disappear. Their number varies in a period of roughly 11 years, but the magnetic field switches its polarity hence the solar cycle lasts about 22 years (*Kallenrode*, 2004).
Active regions are located above sunspots and can be observed as bright areas by X-ray imagers. They can release an energy of 10^{24} J to the IP medium on timescales from seconds to hours (*Lang*, 2001). Such eruptions are called the solar flares. The mechanism of this energy release is related to the reconnection of the magnetic field lines (*Priest*, 1984). The magnetic field creates the current sheet which represents an efficient particle accelerator due to DC electric field and microturbulances (*Martens and Kuin*, 1989). The downward moving particles radiate in the hard X-ray spectra, whereas the particles propagating outward the Sun along open magnetic field lines may produce intense radio emission.
CMEs are very spectacular events when huge amount of solar mass with a loop-like structure (its diameter may exceed the solar radius) is released into the IP medium (*Kallenrode*, 2004). They are thought to be accelerated by a conversion of the magnetic energy into the kinetic energy of ejected solar plasma by a sudden simplification of the magnetic field. CMEs may trigger severe geomagnetic storms if they are Earth-directed. Therefore their observation is crucial for space weather forecasting.

Solar Radio Bursts

Solar radio emissions associated with solar flares or CMEs are called solar radio bursts (*Lang*, 2001). We may categorize them into five types according to their spectral features which reflect the generation mechanisms (Figure 1.3).

- **Type I Radio Bursts (Noise Storms):** are short ($\sim 1s$), narrow-bandwidth (no frequency drift) emissions usually occurring in large numbers with underlying continuum which form noise storms lasting from hours to days. They are thought to be associated with electrons accelerated to modest energies within large scale magnetic loops.

- **Type II Radio Bursts:** are slow frequency drift emissions usually occurring in pairs (fundamental and harmonic emissions). They are excited by fast electrons accelerated on shock fronts of propagating CMEs.

- **Type III Radio Bursts:** are fast frequency drift emissions occurring singularly, in groups, or storms. They are triggered by beams of suprathermal

electrons propagating in the IP medium associated with solar flares.

- **Type IV Radio Bursts:** are broad-band continuum radiations. They are thought to be generated by energetic electrons trapped within magnetic clouds.
- **Type V Radio Bursts:** are smooth and short lived (1 — 3 minutes) continua following some type III radio bursts with opposite sense of polarization compering to the associated type III radio bursts.

Therefore solar radio bursts provide us with important diagnostics of processes occurring in the corona and the IP medium.

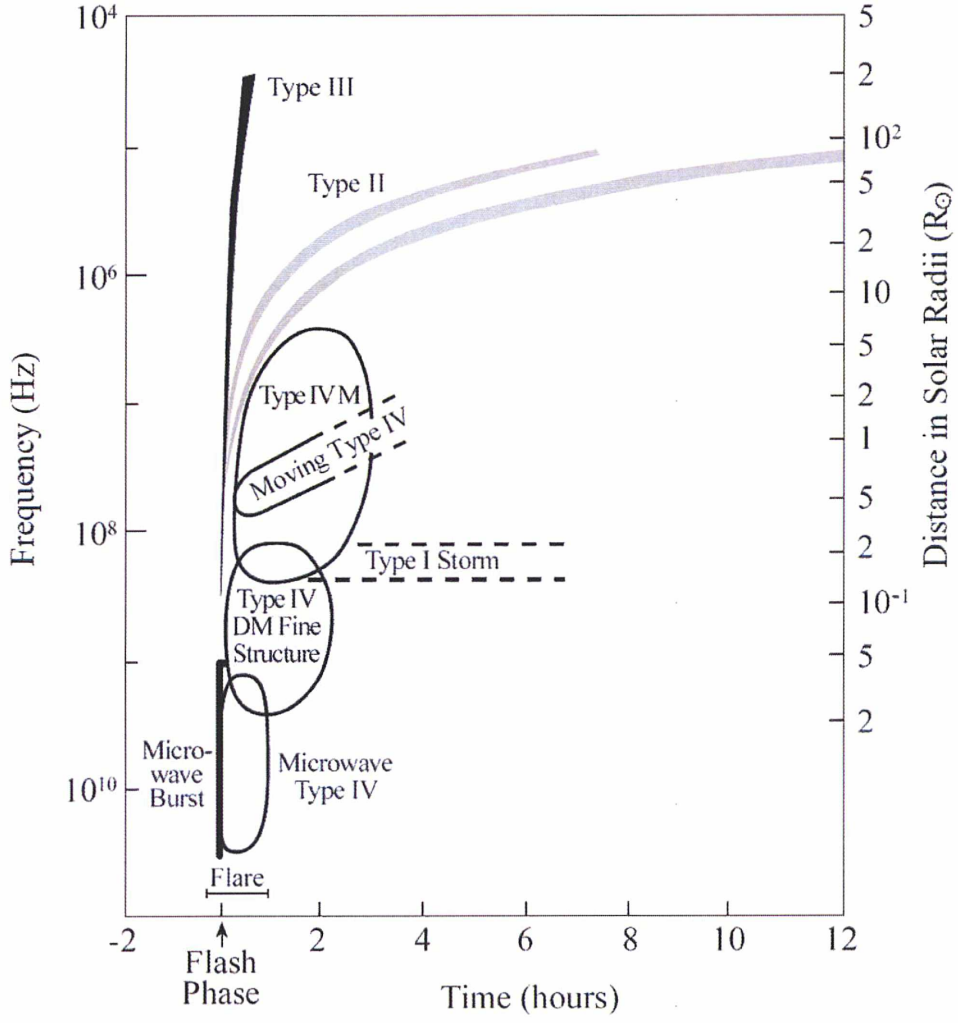

Figure 1.3: Spectral signatures of type I — V solar radio bursts. Adapted from *Lang* (2001).

1.3 Type III Radio Bursts

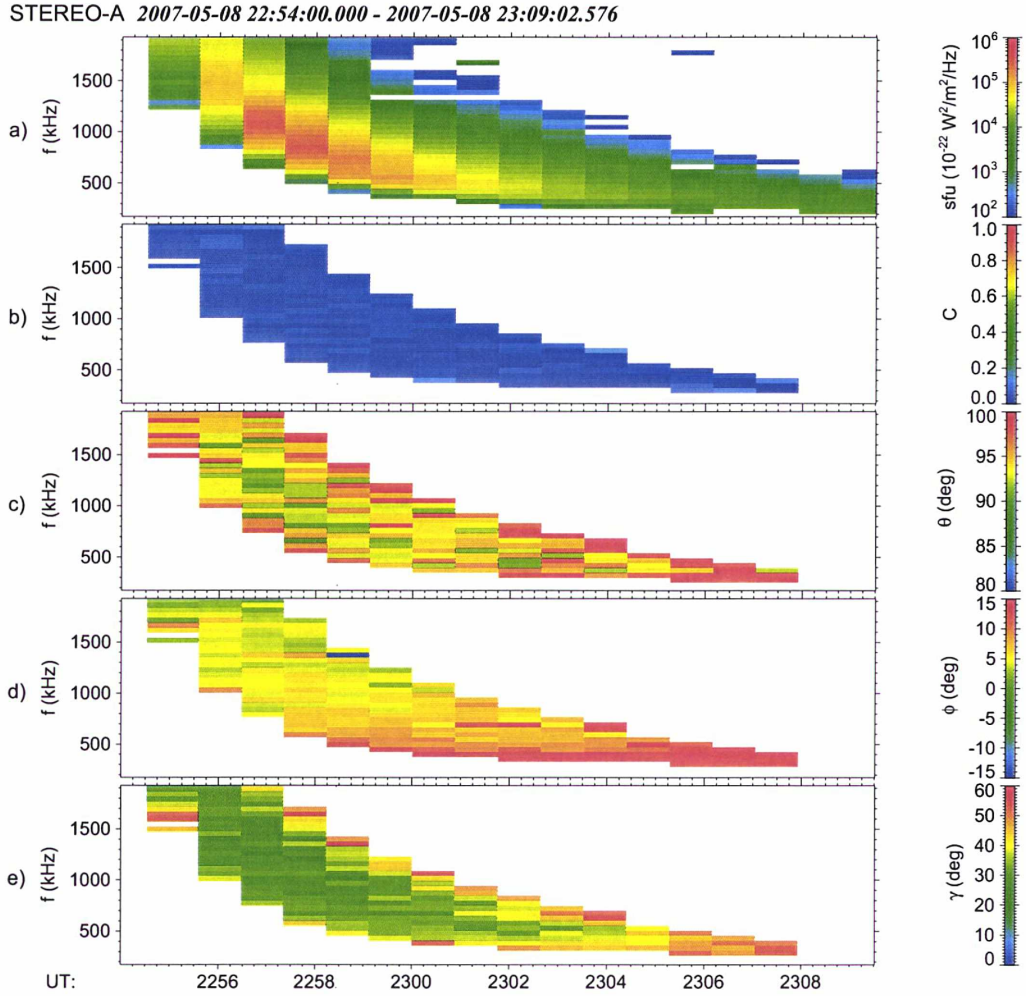

Figure 1.4: An intense type III radio burst recorded from 22:53 to 23:09 UT on the 8 May, 2007: a) the electric field spectral density, b) the coherence, c) the polar angle θ, d) the azimuthal angle ϕ , e) the apparent source size γ for STEREO-A. Adapted from *Krupar et al.* (2012).

Type III radio bursts (Figure 1.4) are consequence of suprathermal electrons ($\sim$ 0.14c) accelerated near the Sun's surface during solar flares and belong among the most intense electromagnetic emissions observed in the heliosphere (*Wild*, 1950, *Dulk et al.*, 1987). Type III-generating electron beams propagate outward the Sun along an open magnetic field line in the corona and the IP medium at large distances beyond 1 AU where suprathermal electrons can be detected *in situ* by spacecraft. These electron beams produce a bump-on-tail instability. This abrupt change of plasma parameters can lead to generation of electrostatic Langmuir waves at the local plasma frequency f_{pe} which is proportional to the local electron density as

$f_{pe}(\mathrm{kHz}) \approx 9\sqrt{\mathrm{n}(\mathrm{cm}^{-3})}$. Since electron beams propagate outward from the Sun, these emissions are generated at lower frequencies corresponding to a decreasing of f_{pe}. Langmuir waves can be afterward converted by nonlinear interactions into electromagnetic waves: type III radio bursts at f_{pe} (the fundamental emission, F) or $2f_p$ (the harmonic emission, H). This conversion involves the wave-wave interactions of Langmuir (L and L'), ion-acoustic (S) and electromagnetic (T) waves (*Ginzburg and Zhelezniakov*, 1958):

$$\begin{aligned} L &\longrightarrow T(f_{pe}) \pm S \\ L &\longrightarrow L' \pm S \\ L + L' &\longrightarrow T(2f_{pe}) \end{aligned}$$

However principles of the conversion has been formulated more than 50 years ago it is still not clear how electron beams can preserve the bump-on-tail instability over distances beyond 1 AU (*Sturrock*, 1964) and several theories remain under debate (*Melrose*, 1980, *Cairns and Robinson*, 1995, *Abalde et al.*, 1998).

Type III radio bursts can be observed from metric (or even shorter) to kilometric wavelengths (*Reiner et al.*, 2000). Multipoint observations of type III radio bursts using GP measurements have already been obtained by spinning spacecraft (*Gurnett et al.*, 1978, *Manning and Fainberg*, 1980, *Hoang et al.*, 1981) and recently also by STEREO which is three-axis stabilized (*Reiner et al.*, 2009, *Krupar et al.*, 2010, 2012, *Martínez-Oliveros et al.*, 2012).

The flux density of type III radio bursts may vary over six orders of magnitude (*Dulk*, 2000). *Weber* (1978) has found in data from the IMP-6 spacecraft (30 kHz — 10 MHz) that the maximum flux density occurs at $\sim$ 1 MHz. This result has been recently confirmed by *Bonnin* (2008) based on joint observations performed by the Ulysses and *Wind* spacecraft.

Although coronal type III radio bursts ($f \sim 200$ MHz) can have up to 35% of the circular polarization being always the o-mode, type V radio burst extensions exhibit the opposite sense (*Dulk and Suzuki*, 1980). Nevertheless the degree of polarization of type III radio bursts at long wavelengths ($f \sim 1$ MHz) is negligible (*Dulk*, 2000).

In a comparison with other electromagnetic emissions, sources of type III radio bursts are apparently extended (*Steinberg et al.*, 1984, 1985, *Bonnin et al.*, 2008), which can be explained by either properties of an intrinsic beaming pattern or scattering by density fluctuations in the IP medium. Propagation of type III radio bursts is affected both by refraction in density gradients and by scattering by inhomogeneities in the solar wind. It results in the shifted position of a source location and enlargement of the source size. *Thejappa et al.* (2007) have performed extensive simulations to study the effects of refraction and scattering at $f = 120$ kHz suggesting the latter is responsible for very extended sources of type III radio bursts.

Chapter 2

Radio Wave Measurements in Space

Contents

The first part of this chapter is dedicated to the principles of radio astronomy at long wavelengths. The second part deals with the SVD inversion of a magnetic spectral matrix whose application will be extended to electric measurements in the following chapter.

2.1 Radio Astronomy at Kilometric Wavelengths

Measurements of solar radio emissions at kilometric wavelenghts from ground based observatories are limited by the ionospheric cut-off (typically at 10 MHz) and terrestrial radio frequency interferences. Therefore we need instruments in space despite their high requirements on design (*e.g.* low mass, small size, low power consumption, immunity to vibration and radiation, *etc.*). Since the magnetic field is fainter by a factor of the speed of light than the electric field component, very efficient preamplifiers are needed in this frequency range for measuring the magnetic component. We will thus focus on electric antennas only in this section. Spacecraft may embark electric monopole or dipole antennas. Two non-collinear monopoles form a dipole. A monopole located perpendicular to an infinite flat conducting surface is the equivalent of a dipole. Hence we consider as an approximation that a monopole placed on a spacecraft body with a conductive surface (however, neither infinite nor planar) behaves as a dipole.

2.1.1 Short Electric Dipole

If the wavelength λ of an electromagnetic wave is significantly larger comparing to the length of a dipole antenna h (*i.e.* $\lambda/10 > h$) used to observe it, we can assume that the electric field of an incident wave $\mathbf{E}$ is spatially homogeneous along an antenna itself (*Kraus*, 1966). This frequency range is called the quasi-static range or the short dipole range and an incoming electromagnetic wave induces a voltage V_k at antenna feeds:

$$V_k = \mathbf{E} \cdot \mathbf{h}_k \tag{2.1}$$

where $\mathbf{E}$ is the electric field of the wave and $\mathbf{h}_k$ represents an effective antenna vector (*Schelkunoff*, 1952).

2.1.2 GP Measurement Expressions

The main goal of a GP analysis is to retrieve flux, polarization state and direction of arrival of an incident electromagnetic wave. In order to perform the GP analysis we need to measure both auto- and cross-correlations between three antennas resulting in a correlation matrix:

$$P_{ij} = \langle \hat{V}_i \hat{V}_j^* \rangle, \tag{2.2}$$

where $\hat{V}_k$ is a vector of complex amplitudes of induced voltages, indices i and j represent three antennas, $\langle \ldots \rangle$ means averaging over a time interval much longer than the observed wave period and * corresponds to complex conjugacy. *Ladreiter et al.* (1995) have derived a relation between measured correlation P_{ij} and properties of an incident electromagnetic wave considering non-orthogonal antennas:

$$\begin{aligned} P_{ij} = \frac{Z_0 G h_i h_j S_0}{2} [&(1+Q)A_iA_j - U(A_iB_j + A_jB_i) + \\ &(1-Q)B_iB_j + \imath V(-A_iB_j + A_jB_i)], \end{aligned} \tag{2.3}$$

$$A_k = -\sin\theta_k \cos\theta \cos(\phi - \phi_k) + \cos\theta_k \sin\theta, \tag{2.4}$$

$$B_k = -\sin\theta_k \sin(\phi - \phi_k). \tag{2.5}$$

The right hand side of equation (2.3) contains the impedance of free space (Z_0); the parameters of the electrical antennas: effective lengths (h_k), directions (θ_k and ϕ_k) and gain (G); and incident wave properties: the **k**-vector directions (θ and ϕ), the Stokes parameters (*Kraus*, 1966): the energy flux S_0, the linear polarization degrees Q and U, and the circular polarization degree V. A_k and B_k represent projections of the effective antenna vector on the wave plane axes. We may thus have up to nine measurements for a determination of six unknown wave parameters (four Stokes parameters and two angles defining a wave vector direction).

2.1.3 Spin Demodulation GP

The basic idea of spin demodulation GP is very simple: when a spinning antenna points toward a source, the smallest signal is measured (*Lecacheux*, 1978). This spin modulation method has been used onboard *e.g.* Hawkeye 1, IMP 8 and HELIOS 2 spacecraft (*Kurth et al.*, 1975, *Gurnett et al.*, 1978). In case of a spinning spacecraft with two antennas (one axial and one equatorial) we can sum their responses with a phase shift (*i.e.* antenna switching) in order to obtain an additional inclined synthetic antenna (*Manning and Fainberg*, 1980). This technique has been implemented onboard ISEE-3, *Wind* and Ulysses (*Stone et al.*, 1992, *Bougeret et al.*, 1995). Spinning spacecraft do not provide reasonable GP results on timescales shorter than their spin period.

2.1.4 Instantaneous GP

For instantaneous GP we need three spatially fixed non-coplanar antennas and a multi-channel receiver which retrieve both auto- and cross-correlations. Two-channel receivers have been used onboard *e.g.* Cassini (*Gurnett et al.*, 2004) and STEREO (*Bougeret et al.*, 2008, *Cecconi et al.*, 2008). These receivers provide us with four independent measurements (two auto-correlations between two antennas and real and imaginary parts of the cross-correlation) per one measurement, *i.e.* instantaneously. Hence we need three measurements to build a spectral matrix containing the whole GP information. *Lecacheux* (1978) has found a solution for an ideal case of an orthogonal triad of antennas. However, effective parameters of antennas never achieve this condition due to their electromagnetic coupling with a spacecraft body. Hence *Ladreiter et al.* (1995) proposed a GP inversion taking into account real antenna specifications based on a lest-square model fitting using SVD. *Vogl et al.* (2004) has adopted a Powell minimization algorithm for a GP inversion. *Cecconi and Zarka* (2005) have developed analytical inversions for the GP data. *Martínez-Oliveros et al.* (2012) have recently developed a simple eigenvalue decomposition technique for determination of source direction dedicated for the STEREO spacecraft.

2.1.5 Influence of Extended Sources

Cecconi (2007) has studied a correlation response to an extended source measured on three-axis stabilized spacecraft. The following equations represent an extension of equations (2.3) — (2.5) taking into account an extended source:

$$\begin{aligned} P_{ij} &= \frac{Z_0 G h_i h_j S_0}{2}\left[(1+Q)\left(A_iA_j\frac{\Gamma_2}{2}+C_iC_j\left(\Gamma_1-\frac{\Gamma_2}{2}\right)\right)\right. \\ &\quad +(U-iV)\left(A_iB_j\frac{\Gamma_2}{2}\right)+(U+iV)\left(A_jB_i\frac{\Gamma_2}{2}\right) \\ &\quad +(1-Q)\left(A_iA_j\frac{1}{2}\left(\Gamma_1-\Gamma_2+\frac{\Gamma_3+\Gamma_1}{4}\right)+B_iB_j\frac{1}{2}\left(\Gamma_1+\frac{\Gamma_3+\Gamma_1}{4}\right)\right. \\ &\quad \left.\left.+C_iC_j\left(\frac{\Gamma_2}{2}-\frac{\Gamma_3+\Gamma_1}{4}\right)\right)\right], \end{aligned} \tag{2.6}$$

$$C_k = \sin\theta_k \sin\theta\cos(\phi-\phi_k)+\cos\theta_k\cos\theta, \tag{2.7}$$

$$\Gamma_k^a(\gamma) = \frac{1}{1-\cos\gamma}\int_0^\gamma \sin(k\theta'_M)d\theta'_M = \frac{1-\cos(k\gamma)}{k(1-\cos\gamma)}, \tag{2.8}$$

$$\Gamma_k^b(\gamma) = \frac{3}{2}\frac{1}{1-\cos\gamma}\int_0^\gamma \left(1-\frac{\tan^2\theta'_M}{\tan^2\gamma}\right)^{1/2}\cdot\sin(k\theta'_M)d\theta'_M, \tag{2.9}$$

$$\Gamma_k^c(\gamma) = \frac{\ln 2}{1-\cos\gamma}\int_0^{\pi/2} \exp\left(-\ln(2)\frac{\tan^2\theta'_M}{\tan^2\gamma}\right)\cdot\sin(k\theta'_M)d\theta'_M. \tag{2.10}$$

The angular half aperture of the source (γ) as seen by the spacecraft is contained in the Γ_k coefficients. The shape of the source (see Figure 2.1), that reflects a radial cut of a source brightness distribution, is considered to be either uniform (equation (2.8): model 2.1a), spherical (equation (2.9): model 2.1b) or Gaussian (equation (2.10): model 2.1c).

2.2 Singular Value Decomposition of the Magnetic Spectral Matrix

The SVD method is an efficient tool for a wave analysis of multi-component measurements of the magnetic field with a point source (*Santolík et al.*, 2003). We define a Hermitian spectral matrix $\hat{S}_{ij}$ composed from magnetic complex amplitudes $\hat{B}_k$ (in a given orthogonal frame) at a given frequency obtained by the multidimensional spectral analysis (*Priestley*, 1989):

$$\hat{S}_{ij} = \langle \hat{B}_i \hat{B}_j^* \rangle \tag{2.11}$$

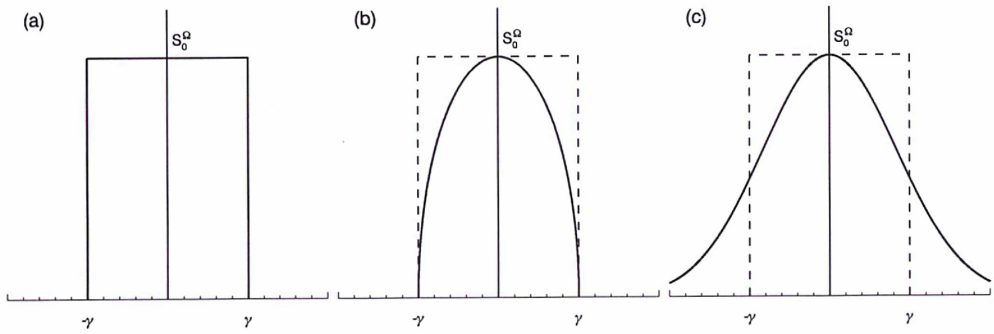

Figure 2.1: Radial cuts of three source brightness distributions: (a) uniform source, (b) spherical source, and (c) Gaussian source. Adapted from *Cecconi* (2007).

From the **S** matrix we calculate the **A** matrix by separating its real and imaginary parts:

$$\mathbf{A} = \begin{pmatrix} S_{11} & \mathcal{R}e(S_{12}) & \mathcal{R}e(S_{13}) \\ \mathcal{R}e(S_{12}) & S_{22} & \mathcal{R}e(S_{23}) \\ \mathcal{R}e(S_{13}) & \mathcal{R}e(S_{23}) & S_{33} \\ 0 & -\mathcal{I}m(S_{12}) & -\mathcal{I}m(S_{13}) \\ \mathcal{I}m(S_{12}) & 0 & -\mathcal{I}m(S_{23}) \\ \mathcal{I}m(S_{13}) & \mathcal{I}m(S_{23}) & 0 \end{pmatrix}. \tag{2.12}$$

Applying SVD on this special real form of the complex spectral matrix we obtain real matrices **U**, **W** and $\mathbf{V}^T$ (*Golub and Van Loan*, 1996):

$$\mathbf{A} = \mathbf{U} \cdot \mathbf{W} \cdot \mathbf{V}^T. \tag{2.13}$$

The matrix **U** is a 6×3 matrix with orthonormal columns used in the decomposition of **A** with columns in the system of principal polarization axes. The diagonal nonnegative 3×3 matrix **W** contains three singular values. Direction of polarization axes are in rows of the 3×3 matrix $\mathbf{V}^T$ (*Santolík et al.*, 2003). For further description it is convenient to order columns of these matrices into an ascending order of singular values w_{kk}:

$$\mathbf{A} = \begin{pmatrix} U_{11} & U_{12} & U_{13} \\ U_{21} & U_{22} & U_{23} \\ U_{31} & U_{32} & U_{33} \\ U_{41} & U_{42} & U_{43} \\ U_{51} & U_{52} & U_{53} \\ U_{61} & U_{62} & U_{63} \end{pmatrix} \begin{pmatrix} w_{11} & 0 & 0 \\ 0 & w_{22} & 0 \\ 0 & 0 & w_{33} \end{pmatrix} \begin{pmatrix} V_{11} & V_{21} & V_{31} \\ V_{12} & V_{22} & V_{32} \\ V_{13} & V_{23} & V_{33} \end{pmatrix}, \tag{2.14}$$

where the condition $w_{11} \leq w_{22} \leq w_{33}$ is fulfilled. As **W** is diagonal we will denote its components as w_1, w_2, and w_3.

2.2.1 Polarization Ellipsoid Geometry

Lengths

The diagonal nonnegative matrix $\mathbf{W}$ in equation (2.14) contains three singular values that represent relative lengths of the axes of the polarization ellipsoid. These singular values reveal magnetic field variances along axes of the polarization ellipsoid. Therefore we can calculate planarity F of polarization of the magnetic field by comparing amplitudes of the smallest and the largest singular values (*Santolík et al.*, 2003):

$$F = 1 - \sqrt{w_1/w_3}. \tag{2.15}$$

In a case of a monochromatic plane wave $F = 1$, *i.e.* the polarization ellipsoid degenerates to an ellipse, while for $F = 0$ it becomes a sphere. Ratio of the middle and the largest components of $\mathbf{W}$ yields information on ellipticity L_p of polarization of the wave magnetic field (*Santolík et al.*, 2003):

$$L_p = w_2/w_3. \tag{2.16}$$

Additionally, we can define the sense of elliptical polarization h in the direction of –X axis (direction Sun – spacecraft in Radial-Tangential-Normal (RTN) coordinates, see Appendix B.3) as:

$$h = A_{53}/|A_{53}|. \tag{2.17}$$

The right-handed sense of polarization is represented as $h = 1$, while the left-handed one as $h = -1$.

Directions

SVD provides us with three characteristic directions of the polarization ellipsoid in the rows of the $\mathbf{V}^T$ matrix: the wave vector, minor polarization axis, and major polarization axis directions. These three directions are mutually orthogonal. The wave vector direction $\boldsymbol{\kappa} = \mathbf{k}/|\mathbf{k}|$ is in the row that corresponds to w_1, *i.e.* to the shortest axis of the polarization ellipsoid:

$$\kappa = \begin{pmatrix} V_{11} \\ V_{21} \\ V_{31} \end{pmatrix}. \tag{2.18}$$

In a similar way we can retrieve the direction of the major polarization axis ($\mathbf{a}$) as the row that corresponds to w_3, *i.e.* the largest axis of the polarization ellipsoid:

$$\mathbf{a} = \begin{pmatrix} V_{13} \\ V_{23} \\ V_{33} \end{pmatrix}. \tag{2.19}$$

The direction of the minor polarization axis ($\mathbf{b}$) is in the row that corresponds to w_2, *i.e.* the middle axis of the polarization ellipsoid:

$$\mathbf{b} = \begin{pmatrix} V_{12} \\ V_{22} \\ V_{32} \end{pmatrix}. \tag{2.20}$$

For description of directions we define the colatitude θ and azimuth ϕ as:

$$\begin{aligned} \theta &= \arctan(\sqrt{\kappa_1^2 + \kappa_2^2}/\kappa_3) \text{ for } \kappa_3 \geq 0, \\ \theta &= \pi - \arctan(\sqrt{\kappa_1^2 + \kappa_2^2}/\kappa_3) \text{ for } \kappa_3 < 0, \\ \phi &= \arctan(\kappa_2/\kappa_1), \end{aligned} \tag{2.21}$$

where κ_1, κ_2, and κ_3 are the components of the vector $\boldsymbol{\kappa}$. Hence θ ranges between 0° and 180° while ϕ varies from −90° to 90° Directions of **a** and **b** are defined likewise.

2.2.2 Triangulation

Aforementioned determination of the wave vector direction $\boldsymbol{\kappa}$ allows us to estimate a source location if an electromagnetic emission is observed by two (or more) spacecraft. This process is called triangulation and the source location can be found as an intersection of lines $\mathbf{L_A}$ and $\mathbf{L_B}$ in three dimensional space:

$$\mathbf{L_A} = \mathbf{P_A} + t_A \boldsymbol{\kappa}_A, \tag{2.22}$$

$$\mathbf{L_B} = \mathbf{P_B} + t_B \boldsymbol{\kappa}_B, \tag{2.23}$$

where $\mathbf{P_k}$ denotes spacecraft position vector, $\boldsymbol{\kappa_k}$ represents a wave vector direction and t_k is a free parameter. Two lines may intersect in one point only if they lie in the same plane. However, we may consider the intersection to be the closest point between two lines which can be estimated as a mean distance between $\mathbf{p_A}$ (the closest point on line A) and $\mathbf{p_B}$ (the closest point on line B) calculated from following equations:

$$\mathbf{P_{AB}} = \mathbf{P_B} - \mathbf{P_A}, \tag{2.24}$$
$$\mathbf{M} = \boldsymbol{\kappa}_B \times \boldsymbol{\kappa}_A, \tag{2.25}$$
$$\mathbf{R} = \mathbf{P_{AB}} \times \mathbf{M}, \tag{2.26}$$
$$t_{AI} = \mathbf{R} \cdot \boldsymbol{\kappa}_B, \tag{2.27}$$
$$t_{BI} = \mathbf{R} \cdot \boldsymbol{\kappa}_A, \tag{2.28}$$
$$\mathbf{p_A} = \mathbf{P_A} + t_{AI} \boldsymbol{\kappa}_A, \tag{2.29}$$
$$\mathbf{p_B} = \mathbf{P_B} + t_{BI} \boldsymbol{\kappa}_B. \tag{2.30}$$

2.2.3 Stokes Parameters

In order to obtain Stokes parameters I, Q, U, and V we need to transform a spectral matrix into a matrix in the primary axial system (*i.e.* the polarization plane): The 6×3 matrix R_{kl} represents the spectral matrix $\mathbf{A}$ in this system with separated real and imaginary parts:

$$R_{kl} = \sum_{m=1}^{3} W_{ll} U_{ml} V_{mk} \text{ for } k = 1, 2, 3 \text{ and } l = 1, 2, 3 \tag{2.31}$$

$$R_{kl} = \sum_{m=4}^{6} W_{ll} U_{ml} V_{m-3k-3} \text{ for } k = 4, 5, 6 \text{ and } l = 1, 2, 3. \tag{2.32}$$

The matrix R_{kl} allows us to directly calculate Stokes parameters that provide alternative description of the polarization state of the generally complex vector $\hat{\mathbf{B}}$. This approach can be efficient for ground based observations of electric waves as each of the above parameters is connected to a sum or difference of the measurable quantity. The polarization ellipse (see Figure 2.2) can be determined by its major and minor polarization axes, its orientation in space, and the sense of rotation in a given fixed $(\mathbf{x}, \mathbf{y})$ basis.

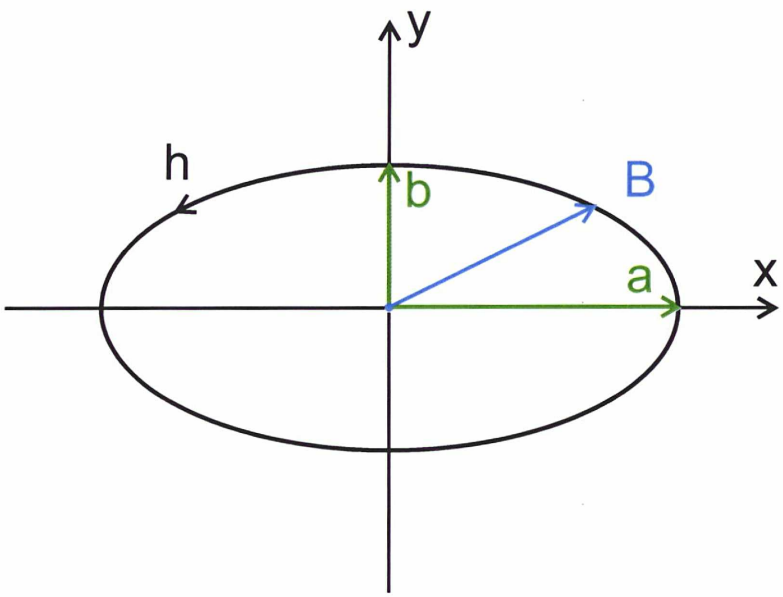

Figure 2.2: The polarization ellipse geometry in a primary axes system retrieved by SVD.

The first Stokes parameter I is defined as:

$$I = |B_x|^2 + |B_y|^2. \tag{2.33}$$

The I represents flux density and can be calculated from the matrix R_{kl}:

$$I = R_{22} + R_{33}. \tag{2.34}$$

The Stokes parameter Q describes the preponderance of linear horizontal over linear vertical polarization:

$$Q = \frac{|B_x|^2 - |B_y|^2}{|B_x|^2 + |B_y|^2}. \tag{2.35}$$

The Q can be retrieved from the matrix R_{kl}:

$$Q = \frac{R_{33} - R_{22}}{R_{33} + R_{22}}. \tag{2.36}$$

As the matrix R_{kl} is in the primary axial system, the **x** basis is identical with the direction of the major polarization axis **a** (Figure 2.2). Therefore Q retrieved by SVD ranges from 0 to 1 instead of a general case when it varies between -1 to 1. The Stokes parameter U describes the preponderance of skew polarization:

$$U = \frac{2\Re(B_x B_y^*)}{|B_x|^2 + |B_y|^2}. \tag{2.37}$$

The U can be also calculated from the matrix R_{kl} as:

$$U = \frac{2R_{23}}{R_{33} + R_{22}}. \tag{2.38}$$

In a case of the SVD inversion the parameter U is null as both axes of the polarization ellipse **a** and **b** correspond to the fixed (**x**, **y**) basis. Hence the contribution of skew polarization dismisses in this frame (Figure 2.2). Finally the parameter V denotes the preponderance of right circularly polarized over the left one:

$$U = \frac{2\Im(B_x B_y^*)}{|B_x|^2 + |B_y|^2}. \tag{2.39}$$

We can retrieve V from the matrix R_{kl}:

$$V = \frac{2R_{53}}{R_{33} + R_{22}}. \tag{2.40}$$

2.2.4 Estimators of the Degree of Polarization

The degree of polarization describes a quantity of an electromagnetic wave which is polarized and can be estimated by several ways. For instance we can directly calculate it from Stokes parameters:

$$p = \sqrt{Q^2 + U^2 + V^2}. \tag{2.41}$$

Alternatively we can also define the two dimensional degree of polarization in the polarization plane (*Santolík et al.*, 2002):

$$C = \sqrt{2\frac{R_{33}^2 + R_{22}^2 + 2|R_{23}|}{R_{33} + R_{22}} - 1}. \tag{2.42}$$

Chapter 3

The SVD Method for Electric Radio Measurements

Contents

First we extent a direct application of SVD to electric field measurements in a case of radio waves. Then results of simulated data are presented (a source size estimation and influence of antenna tilt angle). We describe HFR data processing. As a test of our method we compare STEREO and *Wind* measurements.

3.1 SVD of the Electric Spectral Matrix

The SVD method can directly solve a problem of GP inversion for magnetic field measurements (*Santolík et al.*, 2003). We have extended its application to electric field measurements of radio waves when observed far from their propagation cutoff (*Krupar et al.*, 2010, 2012). In this case, electric field fluctuations **E** are perpendicular to the wave vector direction **k**:

$$\mathbf{E} \cdot \mathbf{k} = 0. \tag{3.1}$$

This condition is fulfilled when a wave frequency f is significantly larger than the local electron plasma frequency f_p. We can thus rewrite definition of the spectral matrix **S** from equation (2.11) to:

$$\hat{S}_{ij} = \langle \hat{E}_i \hat{E}_j^* \rangle, \tag{3.2}$$

where $\hat{E}_k$ represents a complex vector of electric field fluctuations in a given orthogonal system. Equations (2.12) — (2.42) are then valid for electric field fluctuations as well.

3.2 The SVD Analysis of Simulated Data

3.2.1 Empirical Relation for the Source Size

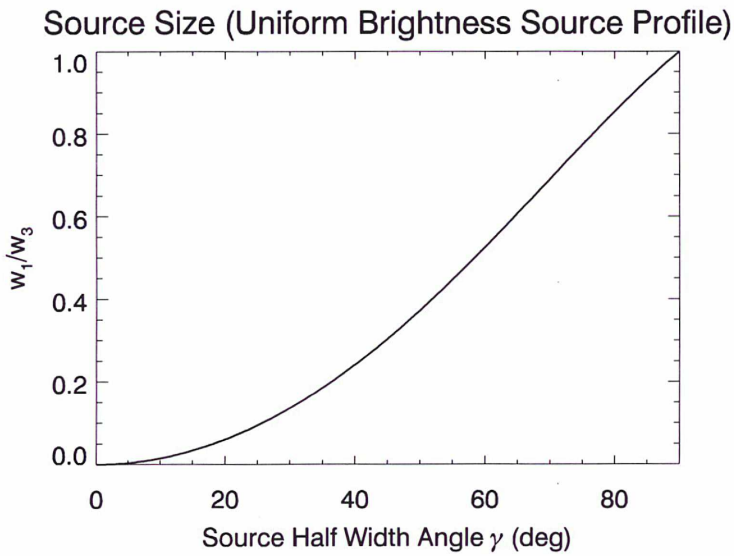

Figure 3.1: The ratio of the smallest and largest components of the diagonal matrix **W** (w_1/w_3) as a function of the apparent source size (γ). A uniform brightness of the source and an unpolarized emission have been assumed. Adapted from *Krupar et al.* (2012).

Type III radio bursts at kilometric wavelengths have typically low degree of polarization and very extended sources (see chapter **??**). In an ideal case of wave with a point source $w_1 = 0$, whereas for wave coming from all directions simultaneously all singular values are equal: $w_1 = w_2 = w_3$. Therefore we have assumed that information about the apparent source size γ is hidden in the ratio w_1/w_3. Figure 3.1 shows w_1/w_3 vs γ (*Krupar et al.*, 2010, 2012). Equations (2.6 – 2.10) have been used for modeling spectral matrices with different γ. Afterwards we have applied the SVD inversion and retrieved w_1/w_3 assuming unpolarized waves ($Q = 0$, $U = 0$, and $V = 0$) and a uniform source shape. For a point source ($\gamma = 0°$) the polarization ellipsoid changes to an ellipse, while for very extended source ($\gamma = 90°$) the polarization ellipsoid becomes a sphere. This empirical relation allows us to estimate γ for unpolarized emissions with uniform source shapes from the ratio w_1/w_3 obtained by SVD.

In the same manner we have performed extensive simulations with various initial parameters. We have modeled spectral matrices with different source shapes, various types and degrees of polarization. This degree of polarization has been calculated as a normalization of Stokes parameters (*i.e.* 100% polarized wave corresponds to $\sqrt{Q^2 + U^2 + V^2} = 1$, whereas 10% polarized wave represents $\sqrt{Q^2 + U^2 + V^2} = 0.1$). Figure 3.2 shows w_1/w_3 vs γ for three source shapes (in columns: uniform, spherical and Gaussian) and five degrees of polarization (in rows: 100%, 30%, 10%, 1% and 0%). Three types of polarization have been investigated: the linear polarization (dashed line: 100%: $Q = \sqrt{2}/2$, $U = \sqrt{2}/2$, $V = 0$), the right-handed circular polarization (dotted line: 100%: $Q = 0$, $U = 0$, $V = 1$) and the elliptical polarization (dashed dotted line: 100%: $Q = \sqrt{3}/3$, $U = \sqrt{3}/3$, $V = \sqrt{3}/3$). Solid lines in the last row denote unpolarized emissions. When the degree of polarization is appreciable (>10%), γ is related to w_1/w_3 and the degree and type of polarization. However this dependence dismisses when the degree of polarization is negligible. Differences between particular source shapes are minor. We can efficiently describe empirical relations for unpolarized emissions (the last row of Figure 3.2) as a 4th order polynomial regression with the independent variable as the square root of w_1/w_3:

$$\gamma(°) = a_0 + a_1\sqrt{\frac{w_1}{w_3}} + a_2\left(\frac{w_1}{w_3}\right) + a_3\left(\sqrt{\frac{w_1}{w_3}}\right)^3 + a_4\left(\frac{w_1}{w_3}\right)^2, \tag{3.3}$$

where a_k are coefficients given in Table 3.1.

3.2.2 Error Analysis of the GP Inversion

Wave Vector Direction

Using equations (2.6 — 2.10) we have performed an error analysis taking into account inaccuracies of the effective antenna directions (2°) and lengths (3%) and an uncertainty on the receiver gain (0.5 dB). These error amplitudes correspond to properties of the S/Waves HFR receiver which has been used for a confirmation of validity of the SVD as a method for GP inversion of extended radio sources (Section

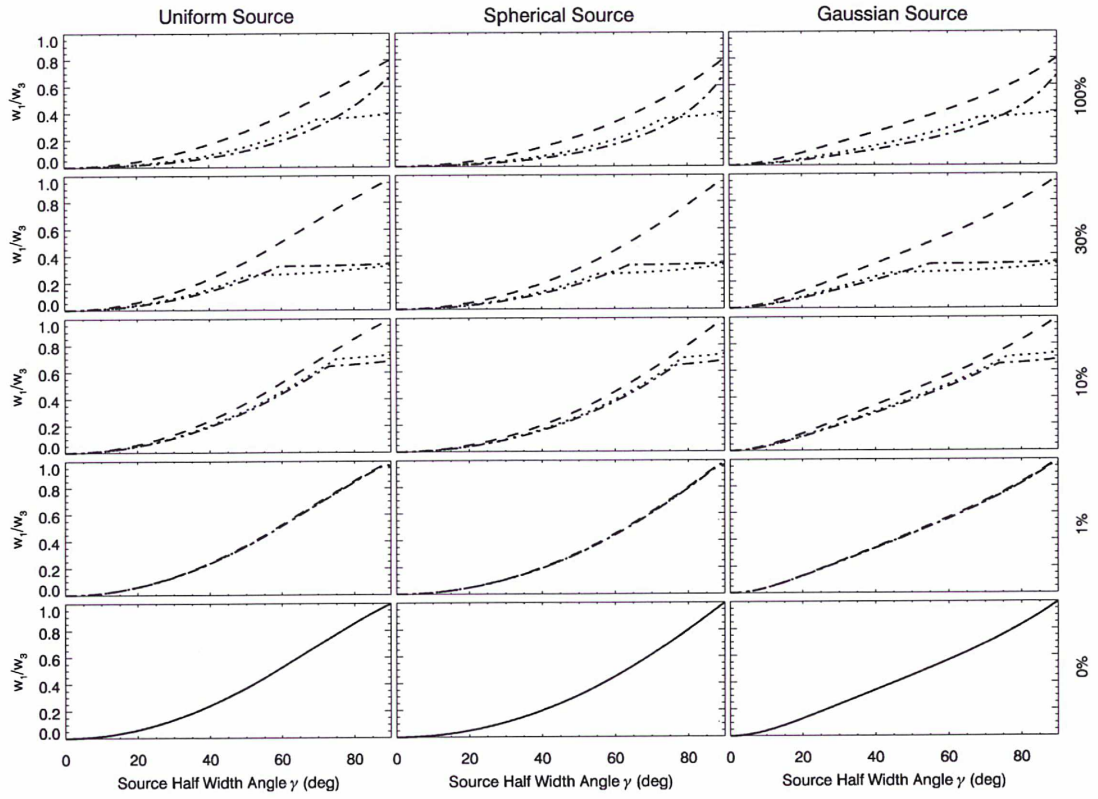

Figure 3.2: The ratio of the smallest and largest components of the diagonal matrix **W** as a function of the apparent source size (γ) with the assumption of no error of the measurements. Results for uniform, spherical and Gaussian brightness source profiles are shown in the left, middle, and right columns,respectively. Degree of polarization is 100% (the first row), 30% (the second row), 10% (the third row), 1% (the fourth row) and 0% (the last row). The type of polarization has been considered to be linear (dotted lines), circular (dashed lines), or elliptical (dash-dotted lines). In case of an unpolarized emission a solid line has been used. Adapted from *Krupar et al.* (2012).

3.4.2). We have simulated antenna directions with normal distributions of absolute deviations centered on the nominal direction with sigma of 2°, and uniform distributions of azimuth. We have also applied the Gaussian noise with a standard deviation of 3% on antenna lengths. We have considered an uncertainty on the receiver gain as another source of an error by applying the Gaussian noise on the final auto/cross-correlation products (normal distributions of the uncertainties in dB centered at 0 dB). This way we have simulated an angle difference between an input **k**-vector direction and an output one obtained by SVD as a function of the apparent source size with an assumption of the errors mentioned above (Figure 3.3). As the apparent source size γ becomes larger, the uncertainty of estimation of the **k**-vector direction increases (*Krupar et al.*, 2012).

a_k	Uniform	Spherical	Gaussian
a_0	0.20	-0.01	-0.42
a_1	75.51	90.35	60.30
a_2	32.70	2.86	-80.3
a_3	-67.62	-12.85	240.53
a_4	48.79	9.61	-129.53

Table 3.1: Coefficients of a polynomial regression for a case of an unpolarized wave for equation (3.3). Adapted from *Krupar et al.* (2012).

Source Size

We have also investigated an angle difference between an input γ and an output one obtained by SVD vs an input γ (Figure 3.5). For small sources ($\gamma < 5°$) the empirical relation overestimates the source size γ whereas it underestimates the source size γ for very large sources ($\gamma > 60°$). Regarding Figures 3.3 and 3.5 we conclude that an uncertainty on the receiver gain has the largest influence affecting our analysis. Therefore we have considered it to be a main source of errors in the GP analysis (*Krupar et al.*, 2012).

3.2.3 Influence of the Antenna Tilt

The techniques developed for S/Waves can also be applied to other instruments onboard three-axis stabilized spacecraft. Especially the Radio and Plasma Wave (RPW) instrument for Solar Orbiter (*Maksimovic et al.*, 2007) for which we need to evaluate if we can do GP even if the chosen antenna configuration is inappropriate. Solar Orbiter is an M-class mission in the European Space Agency (ESA) Science Programme Cosmic Vision 2015 — 2025 which will have an orbit with a perihelion as low as 0.28 AU. The RPW instrument will provide new insights into both the micro-scale wave phenomena and IP emissions produced by energetic electrons and shocks.(*Boudjada et al.*, 2005). Due to high requirements on the low frequency electric field measurements demanding equal illuminations of the three antennas (each 5 m), the latter will be coplanar, limiting thus the possibilities of the GP inversion (see Section 2.1.4). An electric coupling with the spacecraft body and thermal bending will result in their tilted directions with respect to the antenna plane. Their effective parameters have been investigated considering various antenna placements on the spacecraft body (*Rucker et al.*, 2011, *Sampl et al.*, 2011). The electric coupling with the spacecraft body will result in tilted effective antenna directions of $\sim 20°$ towards the Sun. The influence of thermal bending will be minor ranging between $\sim 2°$ and $\sim 5°$ in the opposite direction when 70 — 100 cm bending at the top of the antennas has been considered. We thus expect the effective antennas directions to be tilted towards the Sun of 15° — 18°.
We discuss a possible accuracy of the GP inversion with respect to this tilt angle considering uncertainties of the effective antenna parameters (*Krupar et al.*, 2011). Using equations (2.6 – 2.10) we have modeled spectral matrices that represent an

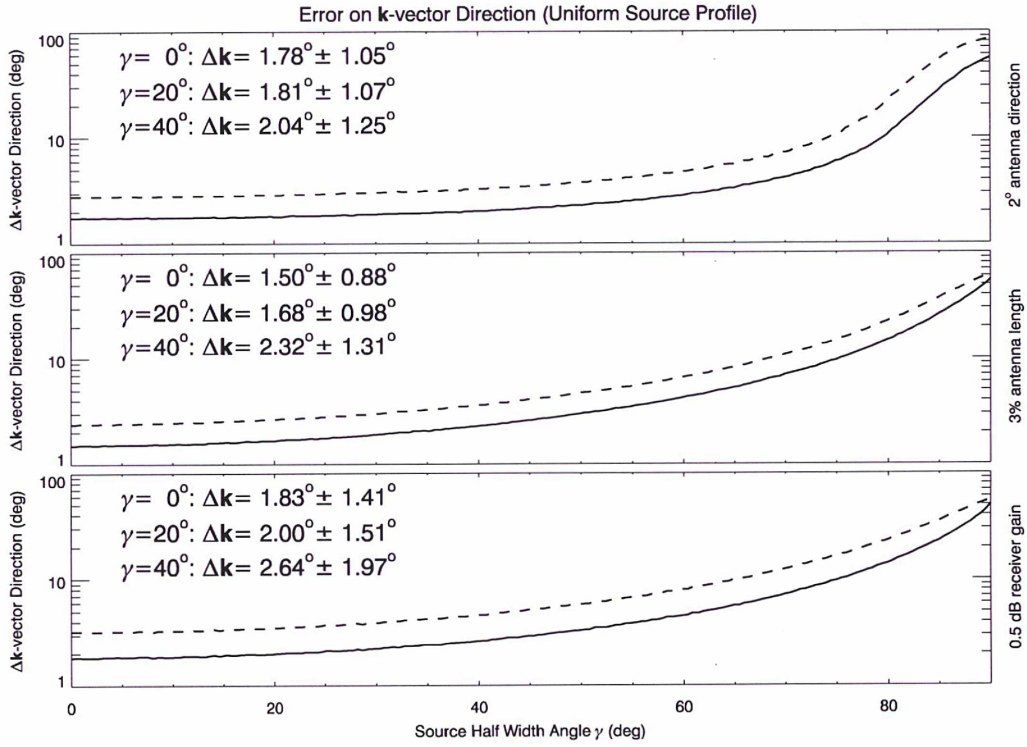

Figure 3.3: An average angle difference between an input **k**-vector direction and the obtained one by SVD as a function of the apparent source size γ is represented by a solid line, a dashed line is the average plus its standard deviation. First panel: an inaccuracy of effective antenna directions of 2°; Second panel: an inaccuracy of effective antenna lengths of 3%; Last panel: an uncertainty on the receiver gain of 0.5 dB. Adapted from *Krupar et al.* (2012).

unpolarized wave (Stokes parameters: $Q = 0$, $U = 0$, and $V = 0$) propagating from a point source located on the Sun (an apparent source size: $\gamma = 0°$, a wave vector direction κ: $\theta = 90°$, and $\phi = 0°$). We have considered effective antenna lengths to be equal ($h_1 = h_2 = h_3$), while effective antenna directions are varying with respect to the tilt angle ($\xi_1 = 0°$, $\xi_2 = -125°$, and $\xi_3 = 125°$; $\zeta_1 = \zeta_2 = \zeta_3 \in < 90°, 65° >$). ζ is the colatitude from the X axis and ξ the azimuth from the Z axis. Various simulations have been performed for each set of parameters considering different sources of errors. The wave vector directions κ have been estimated by the SVD method.

Figure 3.5a shows mean deviations of the wave vector directions κ from from the Sun direction as a function of the tilt angle ζ. We have modeled normal distributions of lengths centered on the nominal lengths h_j with sigma$(h_j)/h_j = 0.01, 0.03,$ and 0.05 (dotted, dashed, and solid line, respectively). We have also performed an error analysis for uncertainty of the effective antenna direction (Figure 3.5b). In this case normal distributions of absolute deviations centered on the nominal directions with sigma$(h_j)/h_j = 0.01, 0.03,$ and 0.05 (dotted, dashed, and solid line, respectively)

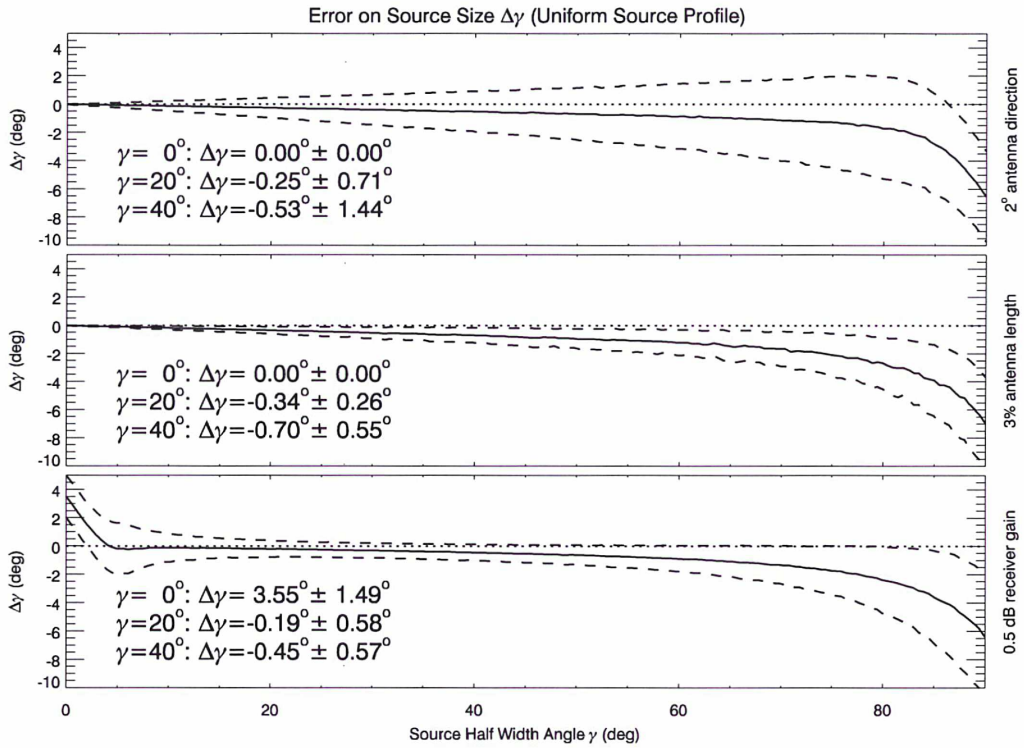

Figure 3.4: An average angle difference between an input γ and the obtained one by SVD as a function of the apparent source size γ is represented by a solid line, a dashed line is the average plus/minus its standard deviation. First row: an inaccuracy of effective antenna directions of 2°; Second row: an inaccuracy of effective antenna lengths of 3%; Third row: an uncertainty on the receiver gain of 0.5 dB. Adapted from *Krupar et al.* (2012).

and uniform distributions of the azimuth angles have been considered.

We have found that the effective antenna tilt angle of at least 5° — 10° is needed for obtaining the GP accuracy better than 10° (*Krupar et al.*, 2011). It has been shown by *Rucker et al.* (2011) that the tilt of 15° — 18° towards the Sun should occur for the effective antenna directions because of the combined effects of the spacecraft body and the antenna thermal bending. We have demonstrated that GP should thus be possible with RPW onboard Solar Orbiter.

3.3 HFR (S/Waves) Data Processing

This Section describes methods for converting measured voltages by HFR (a part of S/Waves) into the waves parameters.

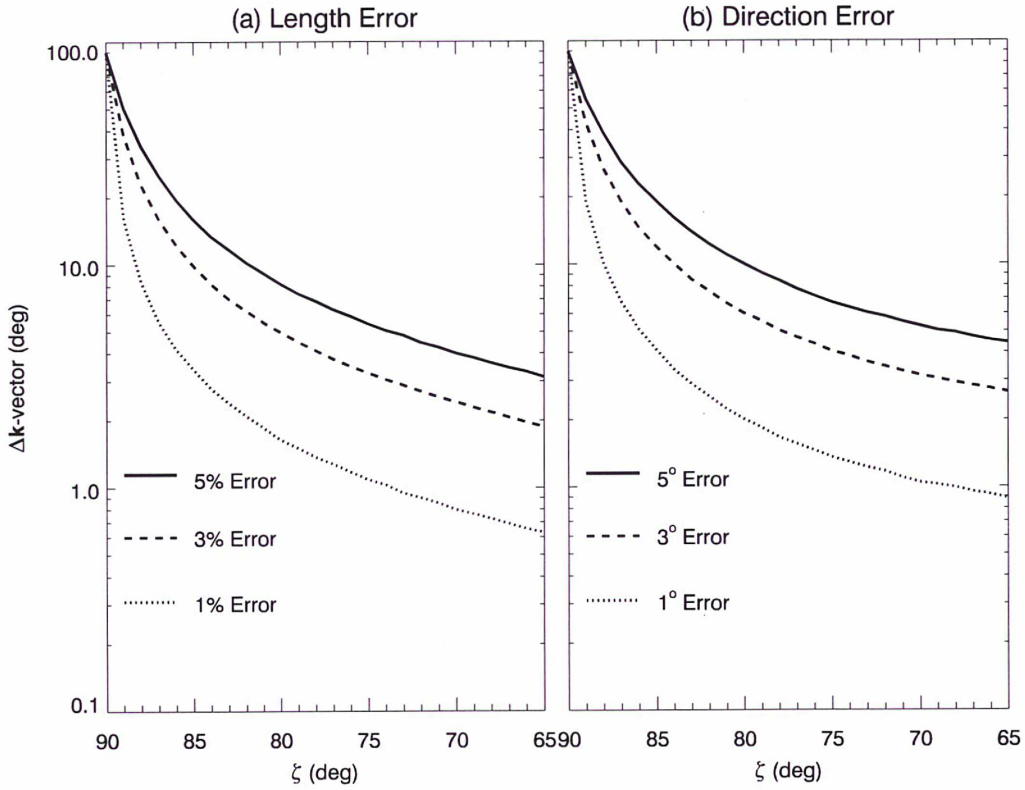

Figure 3.5: The average difference between input and output wave vector direction as a function of antenna tilt angle ζ. Adapted from *Krupar et al.* (2011).

Source Data Set

The HFR is a dual-channel receiver (connected to two antennas at one time) operating in the frequency range 125 kHz – 16.025 MHz with a 25 kHz effective bandwidth (*Bougeret et al.*, 2008). HFR has instantaneous GP capabilities (see Section 2.1.4 for details) between 125 kHz and 1975 kHz allowing us to retrieve the direction of arrival of an incoming electromagnetic wave, its flux and its polarization properties (*Cecconi et al.*, 2008). HFR consists of two receivers: HFR1 (125 kHz – 1975 kHz, 38 frequency channels) and HFR2 (2025 kHz – 16.025 MHz, 281 frequency channels). HFR1 provides us with auto- and cross-correlation on all antennas (three monopoles), while HFR2 retrieves only two auto-correlations (one monopole and one dipole) most of the time since May 2007.

The three monopole antenna elements (6 meters long), made from Beryllium Copper, are used by S/Waves to measure the electric field of radio waves (*Bale et al.*, 2008). The effective length of antenna is only about 1 meter (*Rucker et al.*, 2005, *Macher et al.*, 2007, *Oswald et al.*, 2009, *Zaslavsky et al.*, 2011). Figure 3.6 shows their accommodation on the spacecraft bodies.

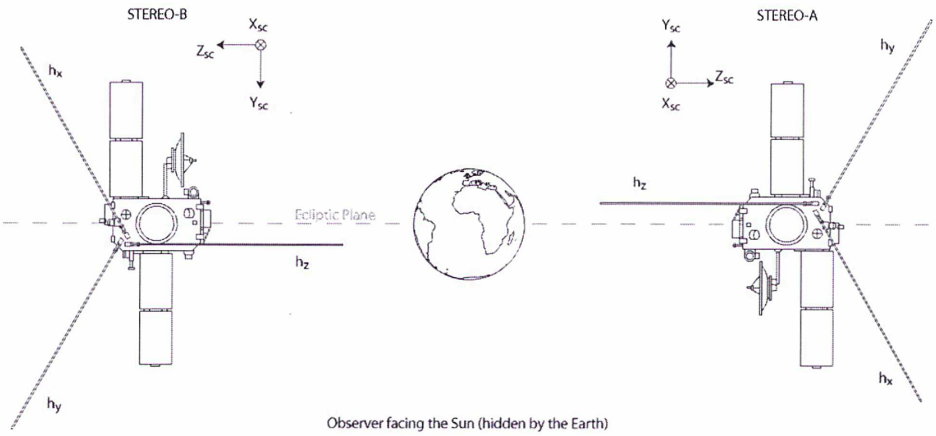

Figure 3.6: Antenna configurations in the spacecraft frame. Adapted from `http://typhon.obspm.fr/stereo/antenna.php`. Credits: B. Cecconi, LESIA, Observatoire de Paris

HFR1

For HFR1 three successive measurements with antenna switching are needed to obtain complete GP information, hence we are interested in a mode when the instrument is rapidly (each 200 ms) switching between these channel/antenna configurations:

- ANT12 = Channel 1: +X/Channel 2: −Y
- ANT21 = Channel 1: −Y/Channel 2: +Z
- ANT11 = Channel 1: +X/Channel 2: +Z

Each channel/antenna configuration provides two real auto-correlations from two antennas and one complex cross-correlation of the voltages induced by the wave electric field between these antennas (*Bale et al.*, 2008). From three quasi-instantaneously acquired measurements we can build a spectral matrix that yields the GP information (*Lecacheux*, 1978, *Bale et al.*, 2008).
We use calibrated (V^2/Hz at preamplifier) level 2 data archived at the CDPP website (`http://cdpp.cesr.fr/`). For ANT12, ANT21, and ANT11, one data record (for each channel/antenna configuration) consists of four values:

- AUTO1: Auto-correlation Channel 1 (V^2/Hz)
- AUTO2: Auto-correlation Channel 2 (V^2/Hz)
- CROSR: Normalized Cross-correlation (real part)
- CROSI: Normalized Cross-correlation (imaginary part)

HFR2

HFR2 provides us with only two auto-correlations from one dipole (X—Y) and one monopole (–Z):

- ANT31 = Channel 1: X—Y/Channel 2: –Z

We use calibrated data from the CDPP as in the case of HFR1. For ANT31, one data record consists of two values:

- AUTO1: Auto-correlation Channel 1 (V^2/Hz)
- AUTO2: Auto-correlation Channel 2 (V^2/Hz)

As no cross-correlations are measured, we use HFR2 data only for estimation of the flux density.

3.3.1 Background Removal

Prior to data processing we need to subtract background levels from the data in order to improve the Signal-to-Noise Ratio (SNR). These background levels consist of the receiver noise V^2_{noise}, the Quasi-Thermal Noise (QTN), and the radio background of galaxy. A major contribution below 500 kHz is the QTN generated by the ambient plasma (*Meyer-Vernet and Perche*, 1989):

$$V^2_{\text{QTN}} \cong 5.10^{-5} \frac{n_e T_e}{f^3 l_{\text{ph}}}, \tag{3.4}$$

where n_e and T_e are the local electron density (cm^{-3}) and temperature (K), f is frequency (Hz), and l_{ph} the physical length (m) of the antenna. On the other hand the galactic background V^2_{galaxy} has larger influence for higher frequencies (*Novaco and Brown*, 1978).

As it is difficult to distinguish particular contributions of V^2_{noise}, V^2_{QTN}, and V^2_{galaxy} we have estimated a receiver background level as a median value over one day of the given auto-correlation for each channel/antenna configuration separately, *e.g.* for the configuration 12 on the channel 1:

$$BKG1_{12} = \text{median}[AUTO1_{12}]. \tag{3.5}$$

We subtract this background level from a signal:

$$\widetilde{AUTO1}_{12} = AUTO1_{12} - BKG1_{12} \tag{3.6}$$

If a signal is below the background, we set the result to zero. This approach is efficient when the instrument measures background values most of the day which is a case the HFR data. However another treatment is needed when this assumption is invalid, *e.g.* during long lasting type III radio burst storms.

Spectral Matrix

From three successive measurements of HFR1 (the ANT12, ANT21, ANT11 configurations) we can build the 3×3 spectral matrix:

$$P_{ij} = \begin{pmatrix} P_{11} & P_{12} & P_{13} \\ P_{12}^* & P_{22} & P_{23} \\ P_{13}^* & P_{23}^* & P_{33} \end{pmatrix}. \tag{3.7}$$

Components of P_{ij} are calculated from corresponding auto- and cross-correlations:

$$P_{11} = \frac{\widetilde{AUTO1}_{12} + \widetilde{AUTO1}_{11}}{2} \tag{3.8}$$

$$P_{22} = \frac{\widetilde{AUTO1}_{21} + \widetilde{AUTO2}_{12}}{2} \tag{3.9}$$

$$P_{33} = \frac{\widetilde{AUTO2}_{21} + \widetilde{AUTO2}_{11}}{2} \tag{3.10}$$

$$P_{12} = (CROSR_{12} + \imath CROSI_{12}) \sqrt{\widetilde{AUTO1}_{12} \widetilde{AUTO2}_{12}} \tag{3.11}$$

$$P_{13} = (CROSR_{11} + \imath CROSI_{11}) \sqrt{\widetilde{AUTO1}_{11} \widetilde{AUTO2}_{11}} \tag{3.12}$$

$$P_{23} = (CROSR_{21} + \imath CROSI_{21}) \sqrt{\widetilde{AUTO1}_{21} \widetilde{AUTO2}_{21}}, \tag{3.13}$$

where $\imath$ represents square root of -1. The P_{ij} matrix is in V^2/Hz calculated in the antenna frame (see Figure 3.6).

3.3.2 Effective Antenna Parameters

Although we use three orthogonal antennas, their effective antenna directions (ζ_{eff} and ξ_{eff}) and lengths (l_{eff}) are different from the physical ones (ζ_{ph}, ξ_{ph}, and l_{ph}) due to their electric coupling with the spacecraft body. These parameters can be modeled by computer simulations, estimated by rheometric measurements (*Macher et al.*, 2007, *Rucker et al.*, 2005, *Oswald et al.*, 2009) or obtained by an in-flight calibration.

The effective antenna directions used in this thesis have been obtained by observations of the non-thermal Auroral Kilometric Radiation (AKR) during STEREO-B roll maneuvers (*Panchenko et al.*, 2010, *Krupar et al.*, 2012). As no AKR has been surveyed by STEREO-A, the effective directions have been assumed to be the same.

The galactic background, as a nearly stable isotropic source, allows us to determine reduced effective antenna lengths (*Manning and Dulk*, 2001, *Zaslavsky et al.*, 2011):

$$h_{\text{eff}} = \left| \frac{Z_s}{Z_s + Z_a} \right| l_{\text{eff}}, \tag{3.14}$$

where Z_a and Z_s represent the antenna impedance and the stray impedance, respectively (*Zouganelis et al.*, 2010, *Zaslavsky et al.*, 2011). The physical and effective antenna parameters are summarized in Table 3.2. For description of antenna direc-

	X	Y	Z
h_{ph} (m)	6.00	6.00	6.00
ζ_{ph} (°)	125.26	125.26	125.26
ξ_{ph} (°)	−120.00	120.00	0.00
h_{eff} (m)	1.46	1.85	1.14
ζ_{eff} (°)	119.00	115.10	123.70
ξ_{eff} (°)	−135.10	124.80	13.40

Table 3.2: Physical and effective antenna parameters (*Panchenko et al.*, 2010, *Zaslavsky et al.*, 2011, *Krupar et al.*, 2012).

tions we use a spherical coordinate system, where ζ is the colatitude from the +X axis and ξ the azimuth from the −Z axis. As the short dipole approximation is valid as long as the wavelength is much larger than the antenna length, these parameters have been used for HFR1 only (*Kraus and Marhefka*, 2002, *Schelkunoff*, 1952). For frequencies above 2 MHz (HFR2) we have performed the same analysis as *Zaslavsky et al.* (2011) in order to obtain accurate reduced effective antenna lengths h_{eff} as a function of frequency (see Figures 3.7 and 3.8). These parameters have been retrieved by comparing the lowest 1% of the data observed within one day (January 13, 2007) and the modeled galactic background V^2_{galaxy} (*Novaco and Brown*, 1978).

Transformation of the Measured Voltages into the Electric Field

For HFR1 we transform the spectral matrix $\mathbf{P}$ containing measured voltages (V^2/Hz) on the antennas into an electric field ($\text{V}^2/\text{m}^2/\text{Hz}$) in the spacecraft coordinate system (*Bale et al.*, 2008):

$$\mathbf{C} = \mathbf{M_2} \cdot \mathbf{P} \cdot \mathbf{M_2}^{\text{T}}, \tag{3.15}$$

where M_2 has been calculated from:

$$\mathbf{M_2}^{-1} = \begin{pmatrix} h^X_{\text{eff}} \cos\zeta^X_{\text{eff}} & h^X_{\text{eff}} \sin\zeta^X_{\text{eff}} \sin\xi^X_{\text{eff}} & -h^X_{\text{eff}} \sin\zeta^X_{\text{eff}} \cos\xi^X_{\text{eff}} \\ h^Y_{\text{eff}} \cos\zeta^Y_{\text{eff}} & h^Y_{\text{eff}} \sin\zeta^Y_{\text{eff}} \sin\xi^Y_{\text{eff}} & -h^Y_{\text{eff}} \sin\zeta^Y_{\text{eff}} \cos\xi^Y_{\text{eff}} \\ h^Z_{\text{eff}} \cos\zeta^Z_{\text{eff}} & h^Z_{\text{eff}} \sin\zeta^Z_{\text{eff}} \sin\xi^Z_{\text{eff}} & -h^Z_{\text{eff}} \sin\zeta^Z_{\text{eff}} \cos\xi^Z_{\text{eff}} \end{pmatrix} \tag{3.16}$$

Thereafter the $\mathbf{C}$ matrix can be transformed into the specific coordinate system (Appendix B):

$$\mathbf{S} = \mathbf{F} \cdot \mathbf{C} \cdot \mathbf{F}^{\text{T}}, \tag{3.17}$$

where the $\mathbf{F}$ matrix has been obtained from the website of the Space Radiation Lab at California Institute of Technology (`http://www.srl.caltech.edu/STEREO/docs/pointing.html`).

Finally the $\mathbf{S}$ matrix contains an electric field ($\text{V}^2/\text{m}^2/\text{Hz}$) in the given coordinate system that is suitable for further wave analysis. From the matrix $\mathbf{S}$ we can calculate

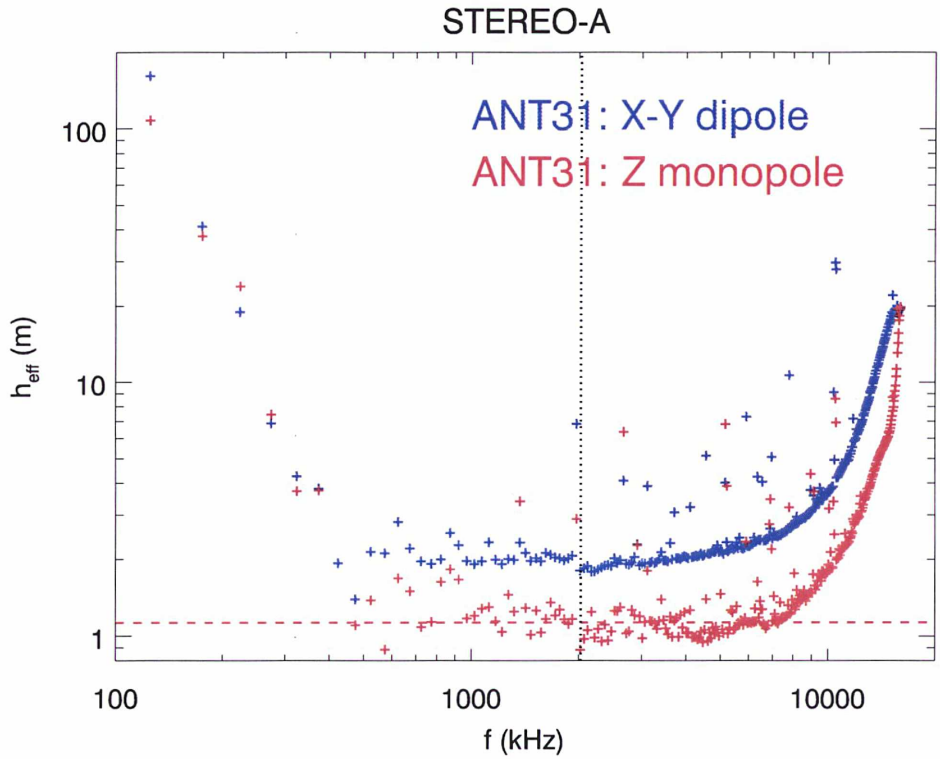

Figure 3.7: Reduced effective antenna lengths of X—Y dipole (in blue) and Z monopole (in red) for STEREO-A vs frequency obtained from measurements on January 13, 2007. A black dotted line separates frequency coverage of HFR1 (< 2 MHz) and HFR2 (> 2 MHz). A dashed red line indicates a h_{eff} of Z monopole used for HFR1 data where the short dipole approximation remains valid. For more details of this analysis see *Zaslavsky et al.* (2011).

sum of power spectral densities of electric field fluctuations ($V^2/m^2/Hz$):

$$E^2_{\text{SUM}} = \sum_{i=1}^{3} S_{ii}. \tag{3.18}$$

For HFR2 (ANT31) we calculate E^2_{SUM} as a sum of the dipole and monopole auto-correlations divided by their reduced effective lengths:

$$E^2_{\text{SUM}} = \frac{\widetilde{AUTO1}_{31}}{h^{XY}_{\text{eff}}} + \frac{\widetilde{AUTO2}_{31}}{h^{Z}_{\text{eff}}}. \tag{3.19}$$

The reduced effective antenna parameters h^{XY}_{eff} and h^{XY}_{eff} have been retrived from Figures 3.7 and 3.8.

From E^2_{SUM} we can derive the flux density S in Solar Flux Units (1 sfu=10^{-22} $W^2/m^2/Hz$) as:

$$S = \frac{10^{22} \times E^2_{\text{SUM}}}{Z_0}, \tag{3.20}$$

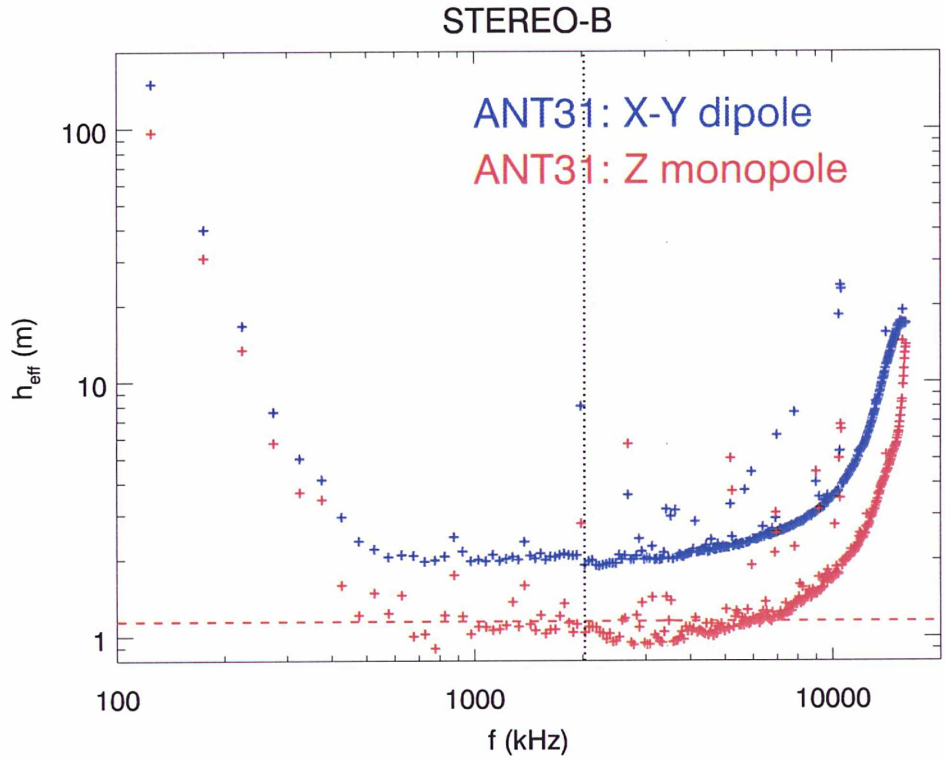

Figure 3.8: Reduced effective antenna lengths of X—Y dipole (in blue) and Z monopole (in red) for STEREO-B vs frequency obtained from measurements on January 13, 2007. A black dotted line separates frequency coverage of HFR1 (< 2 MHz) and HFR2 (> 2 MHz). A dashed red line indicates a h_{eff} of Z monopole used for HFR1 data where the short dipole approximation remains valid. For more details of this analysis see *Zaslavsky et al.* (2011).

where $Z_0 = \sqrt{\mu_0/\epsilon_0} \cong 120\pi$ denotes the impedance of vacuum.

3.4 S/Waves (STEREO) and Waves (*Wind*) Intercalibration

3.4.1 Flux Density

In order to intercalibrate the HFR1 receivers on-board STEREO, we have investigated six intense type III radio bursts observed during May 2007 after the instruments started to operate in the GP mode while separation distances between two STEREO were below 0.2 AU (a separation angle of 12°). We have compared peak fluxes from all frequency channels separately. Since the separation angles between STEREO A/B varied between 6.5° and 11°, radio sources cannot be located by a triangulation. Hence we have applied a correction of the radiation intensity ($1/R^2$) for the slightly different distances of the two spacecraft from the Sun.

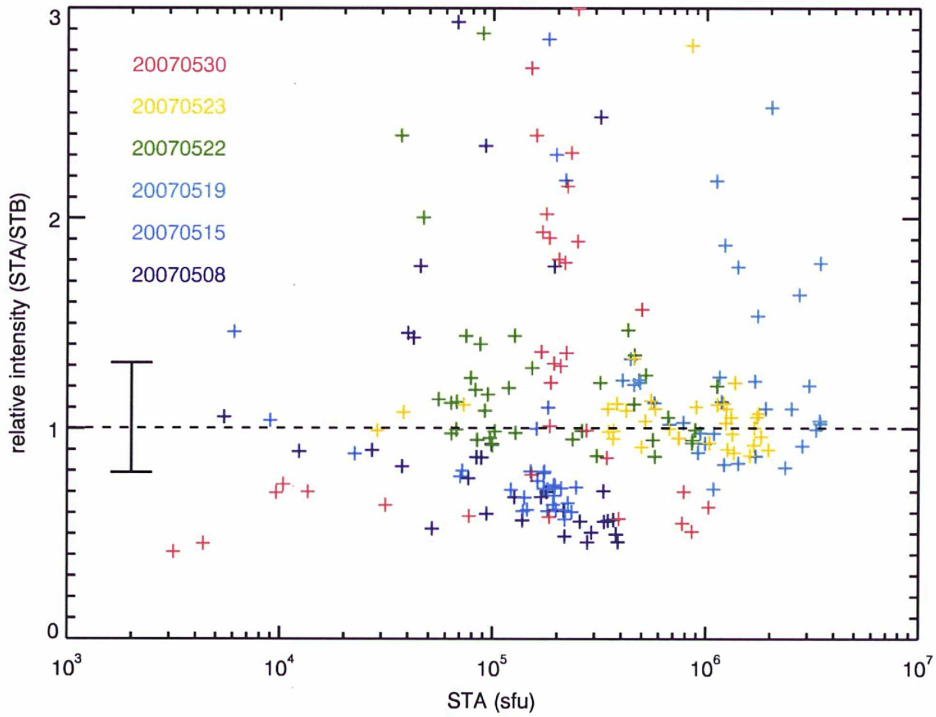

Figure 3.9: Relative intensities between STEREO-A and STEREO-B as a function of the intensity of STEREO-A for six type III radio bursts observed during May 2007. Dashed line represents a median value of the relative intensities. The error bar indicates the 25% and 75% quartiles. We have added a correction of the radiation intensity for the slightly different distances of the two spacecraft from the Sun.

Figure 3.9 shows the relative intensities between STEREO-A and STEREO-B as a function of the intensity measured on STEREO-A in sfu. Dashed line represents a median value of the relative intensities. Although data points are quite scattered, the median value exhibits at ~ 1. We have thus concluded that both receivers are well intercalibrated and can provide an additional input for the GP analysis when one compares an estimated source position and a relative intensity between two spacecraft.

Figure 3.10 displays relative intensities for STEREO-A/ *Wind* and STEREO-B/ *Wind* for peak fluxes on close frequency bands as a function of the intensity measured on *Wind* in sfu. Dotted and dashed lines indicate median values of STEREO-A/ *Wind* and STEREO-B/ *Wind*, respectively. Our results show that differences in the intensity between STEREO and *Wind* are minor. Although receivers on-board STEREO and *Wind* use different methods, the obtained flux densities are comparable during short separation distances. Our results suggest that both HFR1 on-board STEREO-A and STEREO-B are well calibrated with effective antenna lengths given in Table 3.2.

However that this latter conclusion is valid only for signal above the typical galactic

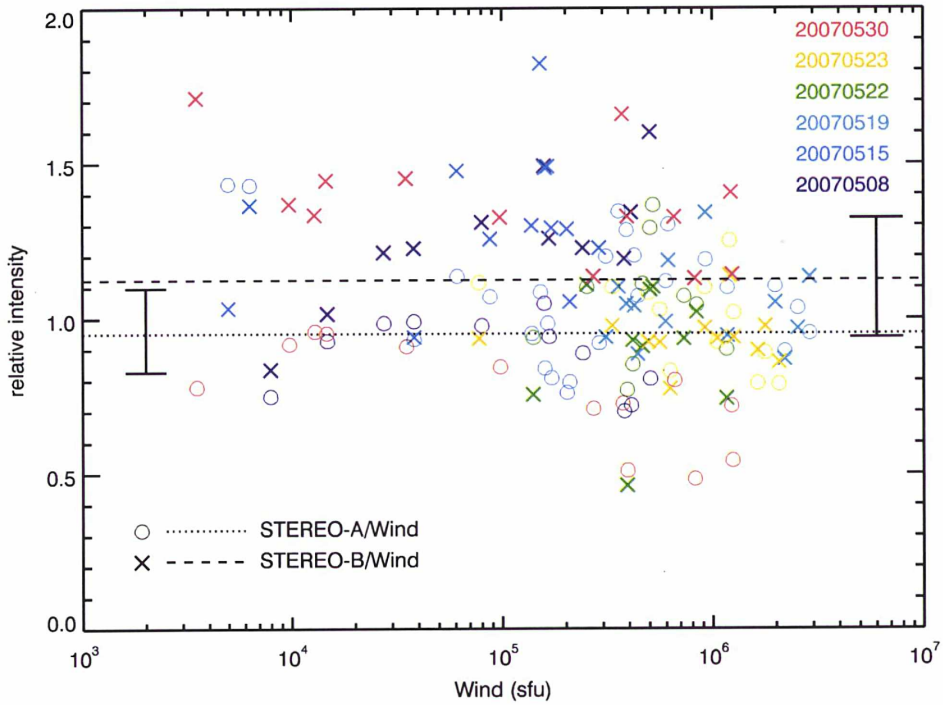

Figure 3.10: Relative intensities STEREO-A/Wind and STEREO-B/Wind as a function of the intensity of Wind for six type III radio bursts observed during May 2007. Dotted and dashed lines indicate median values of STEREO-A/*Wind* and STEREO-B/*Wind*, respectively. The error bars indicate the 25% and 75% quartiles. We have added a correction of the radiation intensity for the slightly different distances of the two spacecraft from the Sun.

background levels, such as it is the case for type III radio bursts. For weak signal, the receiver fine calibration still needs to be improved at the time of the writing of this thesis.

3.4.2 GP Products

As an experimental confirmation of validity of the SVD method for extended radio sources we present an analysis of one type III radio burst from May 8, 2007 observed simultaneously by STEREO and *Wind* during short separation distances. To define the spacecraft positions for this event the Heliocentric Earth Ecliptic (HEE) coordinate system has been used (see Appendix B.1):

- STEREO-A: $[0.96, 0.08, 0.00]_{\mathrm{HEE}}$ AU
- *Wind*: $[0.99, 0.00, 0.00]_{\mathrm{HEE}}$ AU
- STEREO-B: $[1.05, -0.04, -0.01]_{\mathrm{HEE}}$ AU

That day all spacecraft observed an intense type III radio burst from 22:53 to 23:09 UT. It has been the first intense type III radio burst recorded after STEREO started to operate in the GP mode.

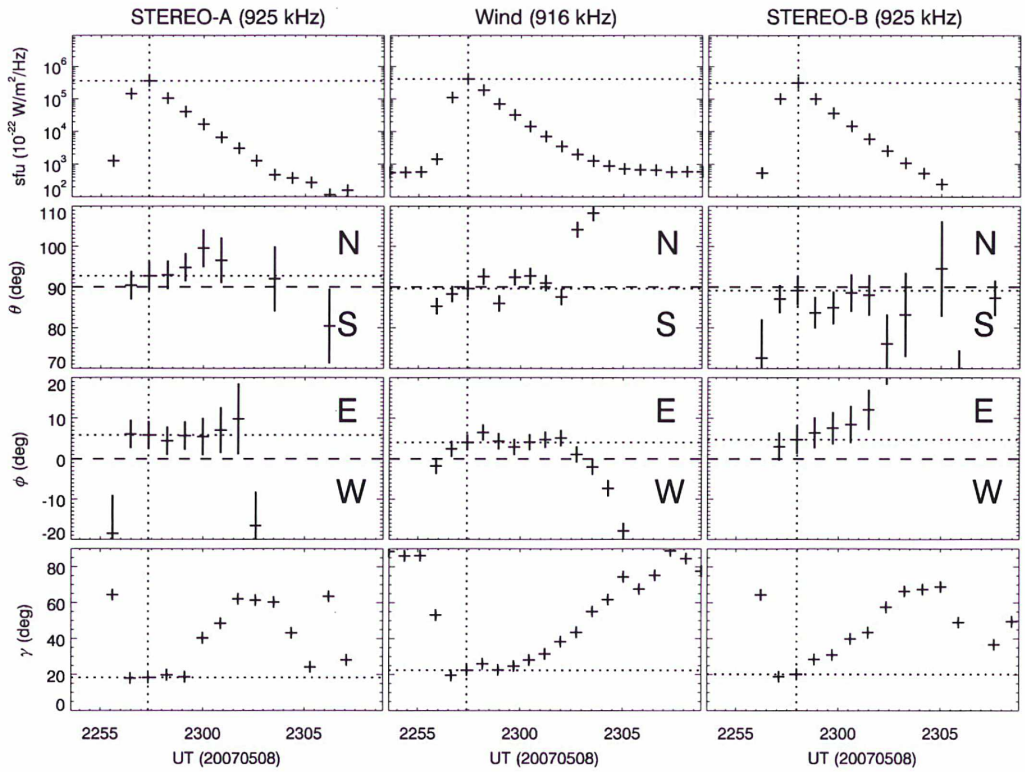

Figure 3.11: Analysis of measurements recorded from 22:53 to 23:09 UT on the 8 May, 2007: the electric field spectral density, the polar angle θ, the azimuthal angle ϕ (in the RTN coordinate system) and the apparent source size γ for STEREO-A (925 kHz), Wind (916 kHz) and STEREO-B (925 kHz). Dashed lines represent the direction to the Sun. Dotted lines indicate values corresponding to the maximum flux at the given spacecraft. Adapted from *Krupar et al.* (2012).

Figure 3.11 shows type III radio burst recorded at the 925 kHz (916 kHz for *Wind*) frequency channel from both STEREO and *Wind*. The STEREO error bars have been retrieved from Figures 3.3 and 3.5 with an uncertainty of the receiver gain of 0.5 dB (see chapters 3.2.2 and 3.2.2 for details) whereas the *Wind* error bars correspond to the standard deviation of 2°. The second and the third row display the polar angle θ and the azimuth angle ϕ, respectively. Dashed lines represent the direction to the Sun. The last row displays the apparent source γ with the assumption of a uniform source brightness distribution. Dotted lines indicate values corresponding to peak fluxes at the given spacecraft. We have achieved a good agreement between the results from STEREO and *Wind*: the apparent source size γ is $\sim 20°$ on all three spacecraft although it has been estimated by different method in the case of *Wind*. Figure 3.12 shows same data but without a background removal

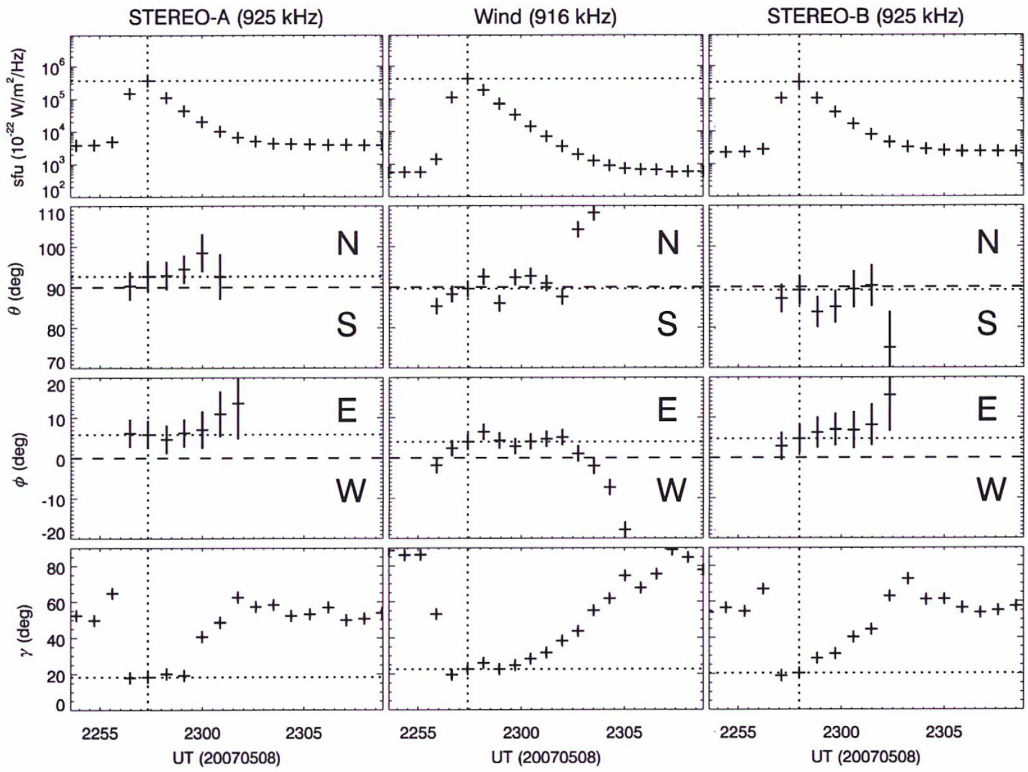

Figure 3.12: Analysis of measurements recorded from 22:53 to 23:09 UT on the 8 May, 2007: the electric field spectral density, the polar angle θ, the azimuthal angle ϕ (in the RTN coordinate system) and the apparent source size γ for STEREO-A (925 kHz), Wind (916 kHz) and STEREO-B (925 kHz). Dashed lines represent the direction to the Sun. Dotted lines indicate values corresponding to the maximum flux at the given spacecraft. We have not performed any background subtraction in equation (3.6).

(Section 3.3.1, equation 3.6). By a comparison with Figure 3.11 it can be seen that results of the GP analysis for peak fluxes are identical.

We have performed the same analysis of several type III radio bursts observed in May 2007, when separation angles between all spacecraft were below 12°. Table 3.3 summarizes results suggesting that SVD can be generally used for estimation of the apparent source sizes.

$\text{Time}_{\text{STEREO-A}}$	f_{STEREO} (kHz)	f_{Wind} (kHz)	$\gamma_{\text{STEREO-A}}$ (°)	γ_{Wind} (°)	$\gamma_{\text{STEREO-B}}$ (°)
2007-05-08T23:07	225	224	35.67	41.30	49.06
2007-05-08T22:58	625	624	17.28	24.30	22.68
2007-05-08T22:57	925	916	18.28	22.50	20.20
2007-05-15T15:46	225	224	52.12	39.10	57.18
2007-05-15T15:39	625	624	21.16	25.30	11.75
2007-05-15T15:37	925	916	24.33	23.90	24.41
2007-05-19T13:11	225	224	35.07	33.90	25.13
2007-05-19T12:57	625	624	24.69	24.90	14.10
2007-05-19T12:56	925	916	17.09	23.80	23.47
2007-05-22T14:37	225	224	42.58	49.00	43.09
2007-05-22T14:31	625	624	24.74	24.50	16.71
2007-05-22T14:30	925	916	19.57	23.70	14.51
2007-05-23T07:35	225	224	44.91	34.90	37.43
2007-05-23T07:23	625	624	23.54	23.70	22.73
2007-05-23T07:22	925	916	21.03	19.90	11.78
2007-05-30T20:44	225	224	45.94	45.40	50.13
2007-05-30T20:36	625	624	21.51	28.20	17.73
2007-05-30T20:34	925	916	19.96	24.00	11.67

Table 3.3: Apparent source sizes γ calculated for six intense type III radio bursts from May 2007 during peak fluxes. The first column corresponds to peak fluxes observed by STEREO-A. Adapted from *Krupar et al.* (2012). The VOTable (the Virtual Observatory format, for more details see `http://www.ivoa.net/Documents/VOTable/`) version of this table can be found as a supplementary material of *Krupar et al.* (2012).

Chapter 4

Solar Radio Bursts Observed by STEREO/Waves

Contents

In this chapter we summarize our observations of solar radio emissions by the S/Waves instrument. First we present an analysis of three type III radio bursts to demonstrate a benefit of a stereoscopic capability of STEREO. Then we provide results of a statistical survey of 156 events. In the end we discuss a type II radio burst triggered by a CME — CME interaction including a comparison with White-Light (WL) observations.

4.1 Type III Radio Bursts: Case Studies

We present three observations of type III radio bursts as examples from a statistical study discussed in Section 4.2. We have selected only events from May 2009 when the separation angle between the two STEREO spacecraft exceeded 90° which is ideal for triangulation of radio sources. Although it was a period of a low solar activity several type III emissions have been detected.

4.1.1 Event 1: 2009-05-01 08:55 — 09:40

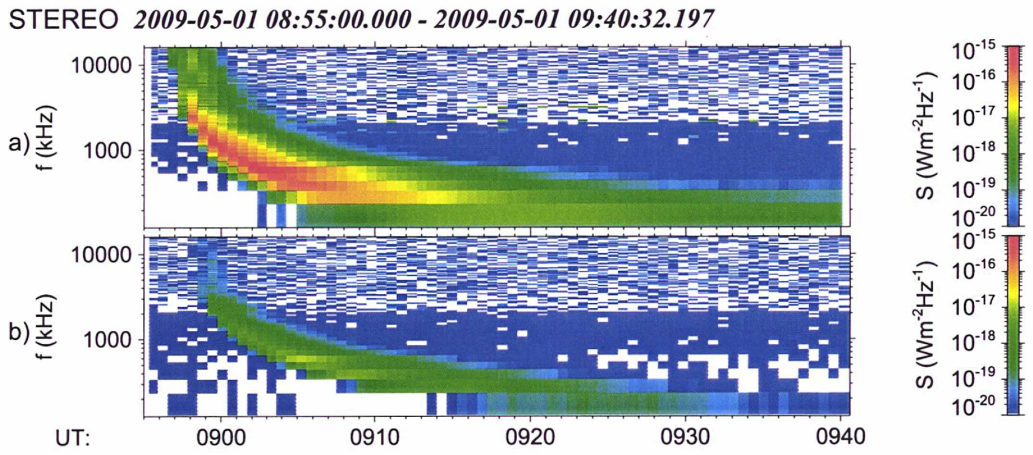

Figure 4.1: Analysis of measurements recorded from 08:55 to 09:40 UT on May 1, 2009: dynamic spectra for STEREO-A (panel a) and STEREO-B (panel b).

We present an observation of a type III radio burst on May 1, 2009 which has been linked to a B2.2 solar flare which started at 08:54 UT reaching maximum at 08:58 UT. For this association we have used data base of solar events compiled by the Lockheed Martin Solar and Astrophysics Laboratory (`http://www.lmsal.com/solarsoft/latest_events_archive.html`). The flare site was at S05°W89° in the HEEQ coordinate system (Appendix B.2).

During this event STEREO-A was located 47.7° west from a Sun-Earth line at 0.96 AU from the Sun whereas STEREO-B was at 46.9° east and 1.01 AU from the Sun. Figure 4.1 contains the flux density S from STEREO-A and STEREO-B. Both STEREO detected a simple and isolated type III radio burst with a starting time of about 8:56 UT (STEREO-A) and 8:58 UT (STEREO-B). Figure 4.2 shows peak fluxes as a function of frequency for STEREO-A and STEREO-B. The flux density measured at STEREO-A is larger of two orders of magnitude than at STEREO-B suggesting an importance of the beaming effects (*Bonnin et al.*, 2008). A high frequency cutoff of $\sim$ 10 MHz appears at the latter spacecraft while the maximum flux density occurs at $\sim$ 500 kHz at both spacecraft.

We have performed a triangulation of radio sources (for details see Section 2.2.2) using wave vector directions during peak fluxes in the Heliocentric Earth Equato-

rial (HEEQ) coordinates (Figure 4.3). Results of the triangulation confirm an assumption that suprathermal electrons triggering the type III burst propagate along the Parker spiral. Source regions of higher frequencies are located closer to the Sun as it can be expected. We have included circles around three intersections (425 kHz, 1175 kHz, and 1875 kHz) denoting error bars of the triangulation. Their diameters correspond to a projections of points $\mathbf{p_A}$ and $\mathbf{p_B}$ in the XY/XZ planes (Section 2.2.2). In the case of XY (Figure 4.3a) we have achieved a very good agreement as differences between $\mathbf{p_A}$ and $\mathbf{p_B}$ are negligible. However these differences are significantly larger ($\sim 20\times$) in the XZ plane (Figure 4.3b). It demonstrates that a separation angle between the two STEREO plays a crucial role in a localization of radio sources. Best results can be obtained for values ranging from 60° to 120°.

We conclude that calculated radio sources are located closer to STEREO-A being in agreement with location of the solar flare site (S05°W89°), detected lower signal at STEREO-B (Figure 4.2), and an observed difference of onset times between two spacecraft (Figure 4.1).

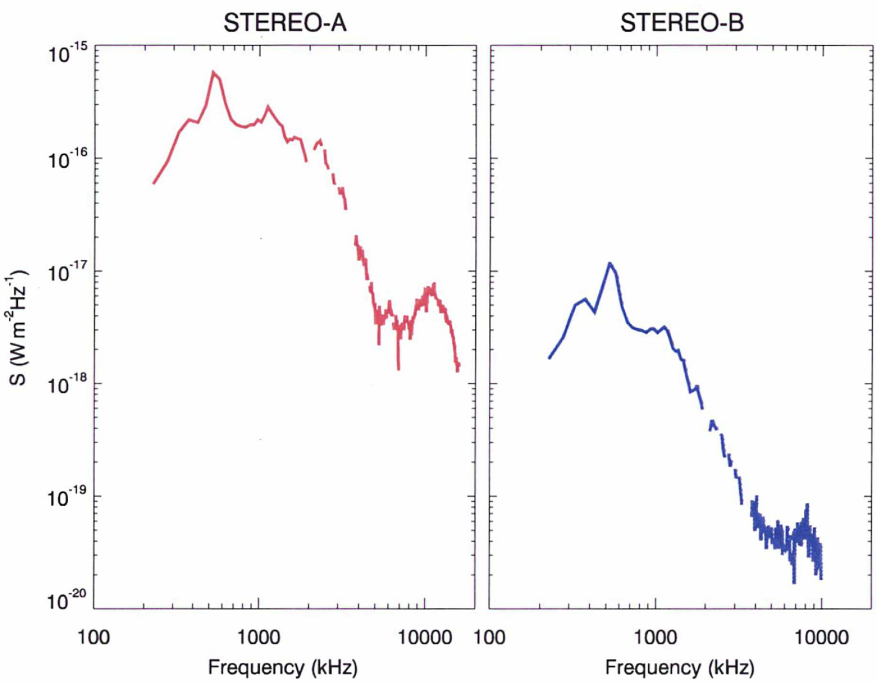

Figure 4.2: Analysis of measurements recorded from 08:55 to 09:40 UT on May 1, 2009: flux density (peak flux values) vs frequency for STEREO-A (on the left) and STEREO-B (on the right).

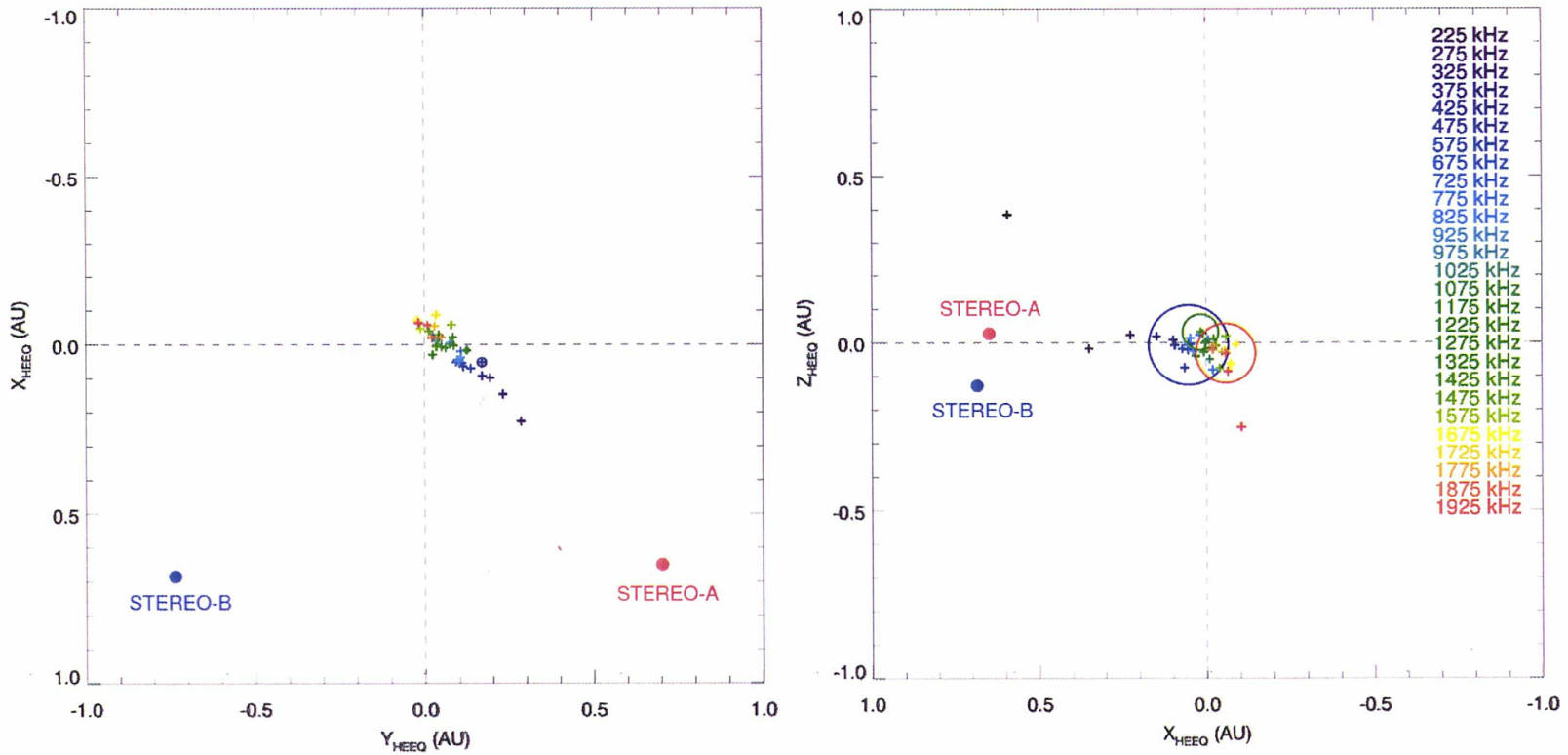

Figure 4.3: Analysis of measurements recorded from 08:55 to 09:40 UT on May 1, 2009: Crosses show intersections between wave vector directions (peak flux values) from STEREO-A and STEREO-B in XY (panel a) and XZ (panel b) planes in the HEEQ coordinate system. Colors represent frequency. Circles around three intersections (425 kHz, 1175 kHz, and 1875 kHz) reprepsent error bars of the triangulation. Positions of STEREO-A and STEREO-B are denoted by blue and red circles, respectively.

4.1.2 Event 2: 2009-05-02 19:30 — 20:20

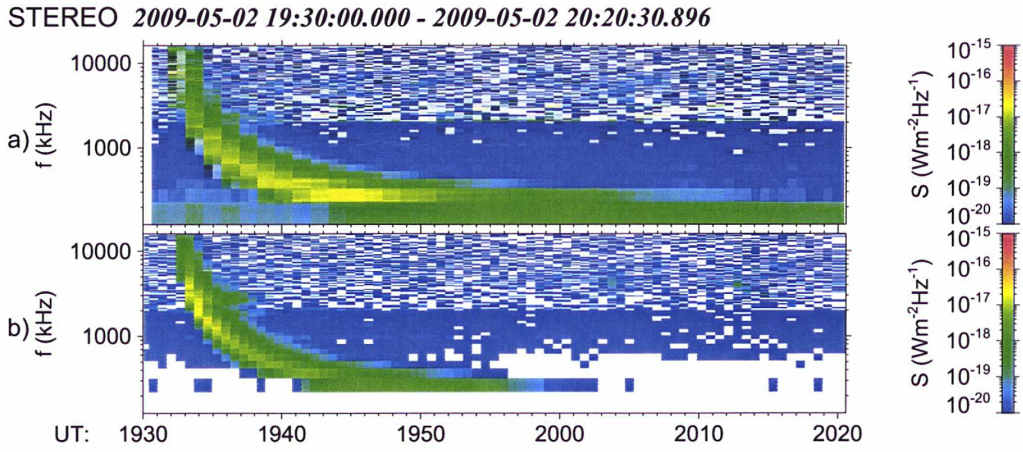

Figure 4.4: Analysis of measurements recorded from 19:30 to 20:20 UT on May 2, 2009: dynamic spectra for STEREO-A (panel a) and STEREO-B (panel b).

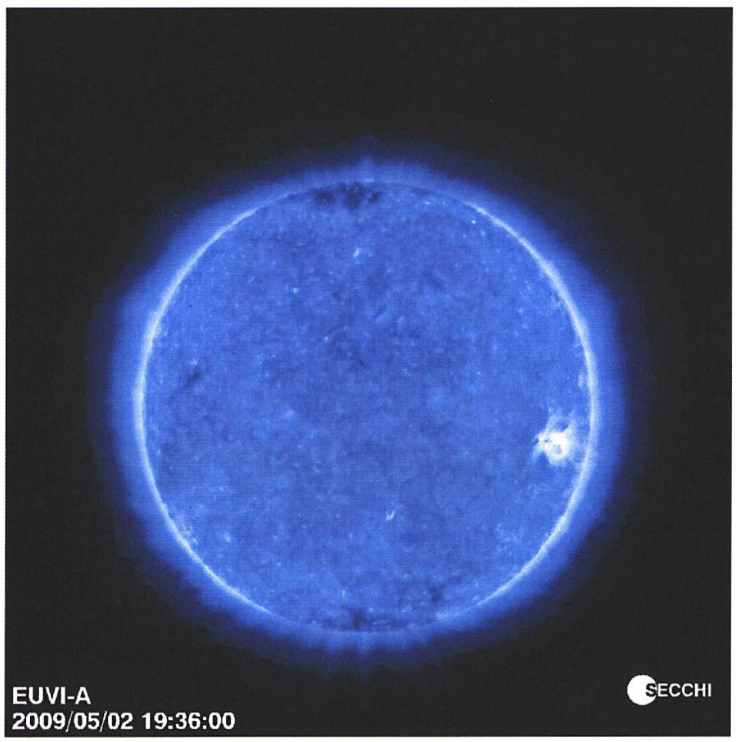

Figure 4.5: Image of the Sun's surface obtained by the SECCHI instrument (EUVI 171) on-board STEREO-A at 19:33 UT on May 2, 2009.

This type III radio burst occured on May 2, 2009 at around 19:30 UT. STEREO-A was at 47.8° west from a Sun-Earth line at 0.95 AU from the Sun while STEREO-B

was located 46.9° east at 1.02 AU from the Sun. Figure 4.4 shows flux density S from STEREO-A and STEREO-B when an intense type III radio burst has been detected at around 19:30 UT. Both spacecraft observed the emission at the same time suggesting that radio sources are located roughly between them. A solar flare triggering this emission has been located on the far side of the Sun from a view of the Earth. Hence we cannot retrieve its intensity and an exact location as spacecraft embarking X-ray imagers orbit the Earth. The solar flare has been observed on the west limb of the Sun close to the equator by EUVI/Sun Earth Connection Coronal and Heliospheric Investigation (SECCHI) (*Howard et al.*, 2008) on-board STEREO-A (Figure 4.5). Figure 4.6 displays peak fluxes vs frequency for STEREO-A and STEREO-B. The maximum flux density at STEREO-B occurs at $\sim$ 1.5 MHz. In a case of STEREO-A we observe the maximum flux at the lowest frequency channel which is .

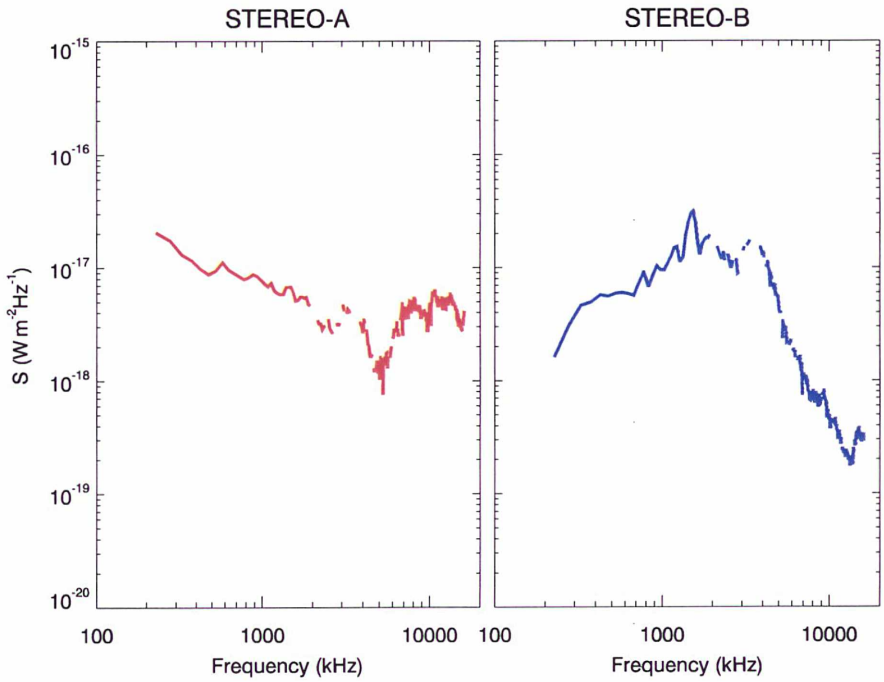

Figure 4.6: Analysis of measurements recorded from 19:30 to 20:20 UT on May 2, 2009: flux density (peak flux values) vs frequency for STEREO-A (on the left) and STEREO-B (on the right).

Figure 4.7 shows positions of radio sources calculated by the triangulation (Section 2.2.2). Our results confirm that the triggering solar flare is located on the far side of the Sun from a perspective of the Earth being in agreement with the EUVI/SECCHI observation (Figure 4.5). As frequency increases radio sources are located further from the Sun. We have also calculated apparent source sizes assuming a Gaussian source brightness distribution (*Krupar et al.*, 2012). Ellipsis around two intersections (225 kHz, and 1925 kHz) represent these apparent source sizes as seen from both spacecraft (STEREO-A: $\gamma_{225} = 17°/\gamma_{1925} = 19°$ and STEREO-B:

$\gamma_{225} = 35°/\gamma_{1925} = 14°$). As apparent sources of type III radio bursts are very extended, scattering by density fluctuations blurs actual radio sources.

4.1.3 Event 3: 2009-05-06 11:30 — 12:20

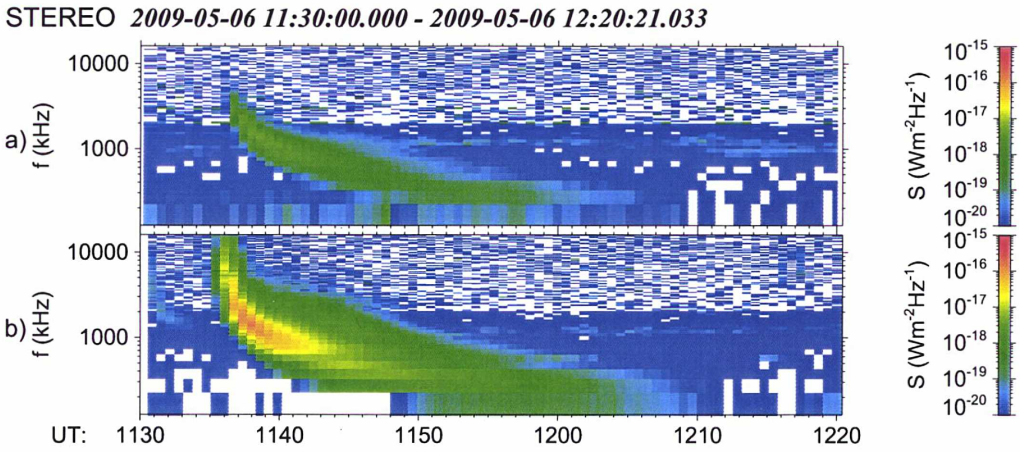

Figure 4.8: Analysis of measurements recorded from 11:30 to 12:20 UT on May 6, 2009: dynamic spectra for STEREO-A (panel a) and STEREO-B (panel b).

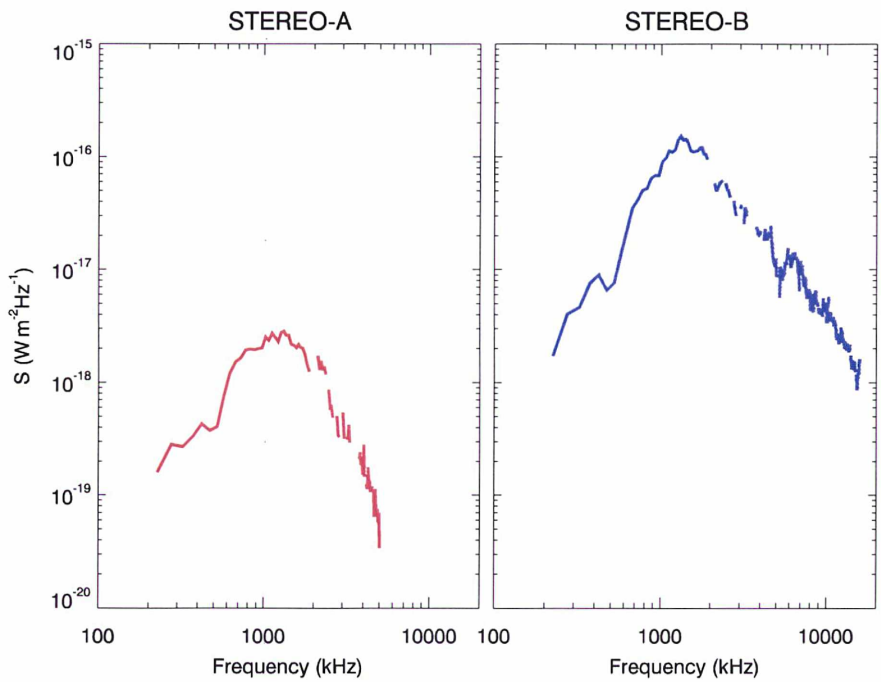

Figure 4.9: Analysis of measurements recorded from 11:30 to 12:20 UT on May 6, 2009: flux density (peak flux values) vs frequency for STEREO-A (on the left) and STEREO-B (on the right).

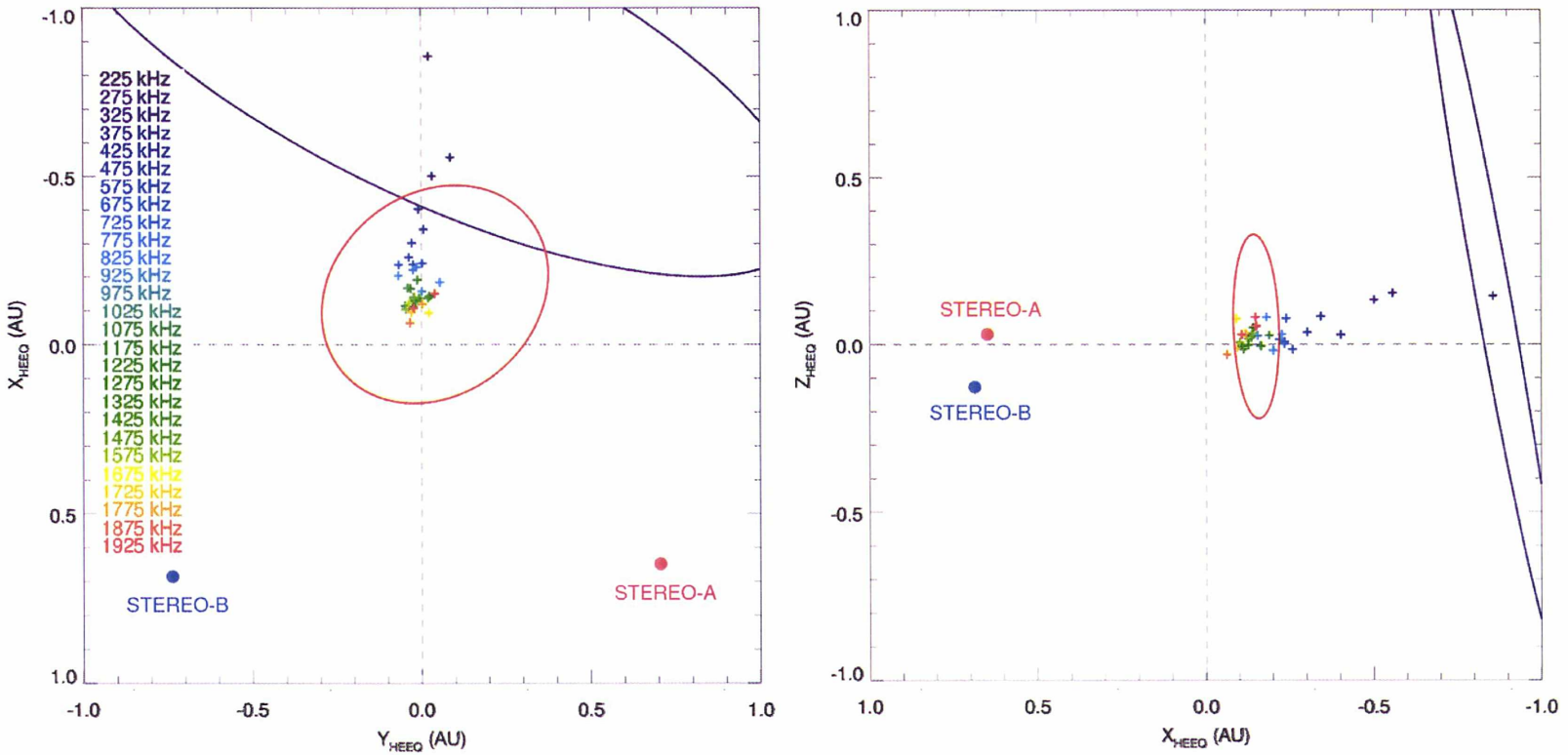

Figure 4.7: Analysis of measurements recorded from 19:30 to 20:20 UT on May 2, 2009: Crosses show intersections between wave vector directions (peak flux values) from STEREO-A and STEREO-B in XY (panel a) and XZ (panel b) planes in the HEEQ coordinate system. Colors represent frequency. Ellipses around two intersections (225 kHz, and 1925 kHz) represent apparent source sizes as seen from both spacecraft. Positions of STEREO-A and STEREO-B are denoted by blue and red circles, respectively.

A faint A3.8 X-ray flare located at N20°E65° triggered a type III radio bursts observed by the two STEREO spacecraft on May 6, 2009. During this event STEREO-A was at 48.2° west from a Sun-Earth line at 0.96 AU from the Sun whereas STEREO-B was located at 46.9° east and 1.02 AU from the Sun. Figure 4.8 show the flux density S from STEREO-A and STEREO-B. This type III radio burst was observed about one minute earlier at STEREO-B than at STEREO-A. Figure 4.9 displays peak fluxes as a function of frequency for STEREO-A (on the left) and STEREO-B (on the right). A signal detected at STEREO-B is about 100× larger than at STEREO-A. The maximum flux density at both spacecraft occurs at $\sim$ 1.5 MHz.

Figure 4.10 shows radio sources determined by triangulation (Section 2.2.2) located closer to STEREO-B. It is in agreement with position of the solar flare site (N20°E65°), detected lower signal at STEREO-A (Figure 4.9), and an observed difference of onset times between two spacecraft (Figure 4.8). Triangulation error bars and apparent source sizes are about the same as at two previous events (Figures 4.3 and 4.7) and thus not shown here.

This type III radio burst has been also observed by Nançay Decameter Array (DAM) and Nançay Radioheliograph (NRT) in France (geographical longitude 2° east, latitude 47° north). DAM operates in the 10 — 80 MHz frequency range and consists of two antenna arrays with a 4000 m^2 effective aperture each (*Lecacheux*, 2000). NRT is composed of 44 antennas of size ranging from 2 — 10 meters spread over two arms (east-west and north-south). NRT provides us with two dimensional images of the Sun in the EW and NS directions at 150 and 432 MHz (*Kerdraon and Delouis*, 1997). Figure 4.11 shows the type III radio detected by DAM and NRT at 11:37 UT. We have observed an ionospheric frequency cutoff at $\sim$ 20 MHz (top panel of Figure 4.11). Results of NRT 150 MHz measurements indicate that the source region of this radio emission is located on the northeast side of the Sun (second and third panels of Figure 4.11) being in agreement with positions of radio sources obtained by the triangulation. Last two panels of Figure 4.11 suggest a high frequency cutoff occurring between 150 MHz and 432 MHz since no emission has been observed at 432 MHz.

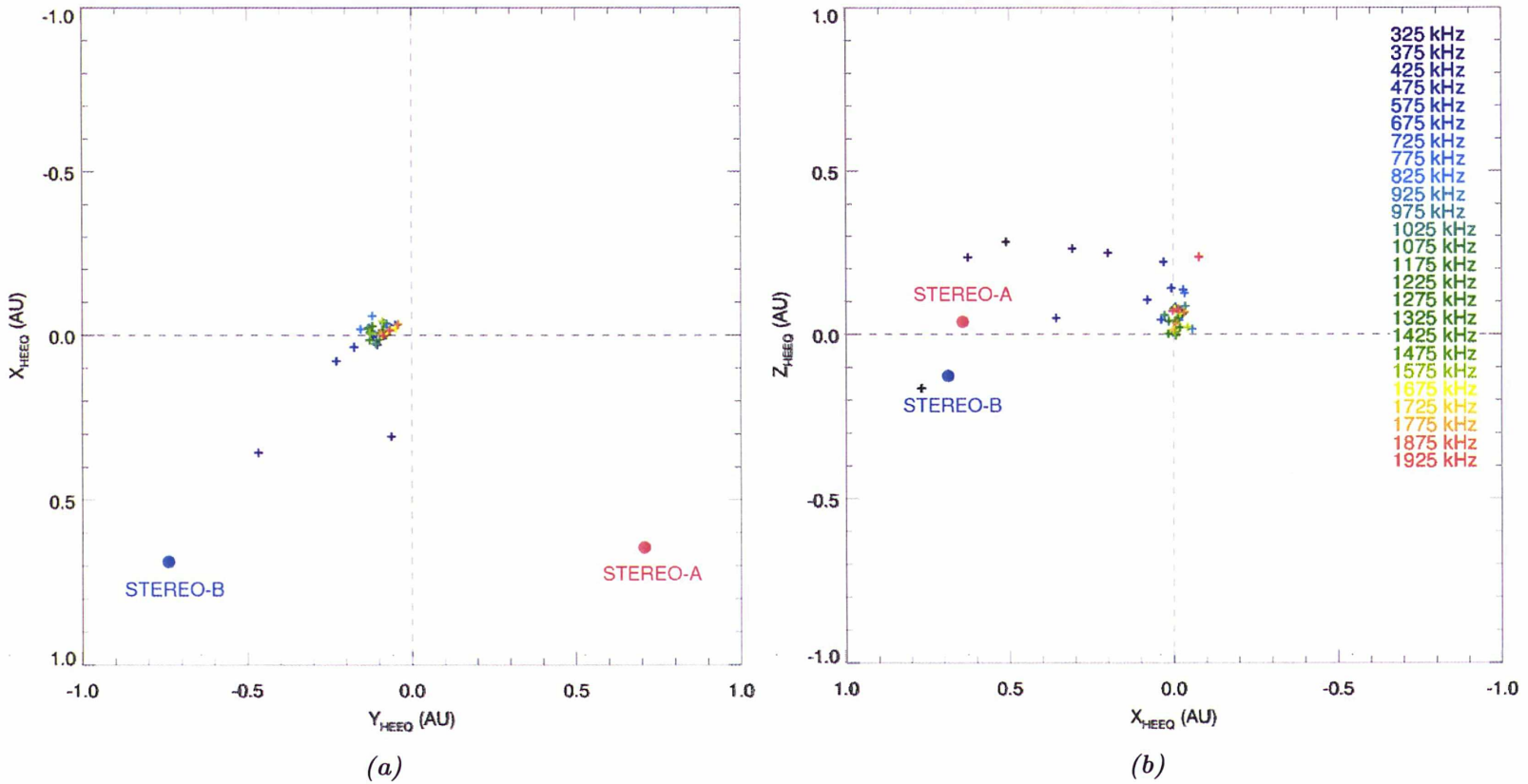

Figure 4.10: Analysis of measurements recorded from 11:30 to 12:20 UT on May 6, 2009: Crosses show intersections between wave vector directions (peak flux values) from STEREO-A and STEREO-B in XY (panel a) and XZ (panel b) planes in the HEEQ coordinate system. Colors represent frequency. Positions of STEREO-A and STEREO-B are denoted by blue and red circles, respectively.

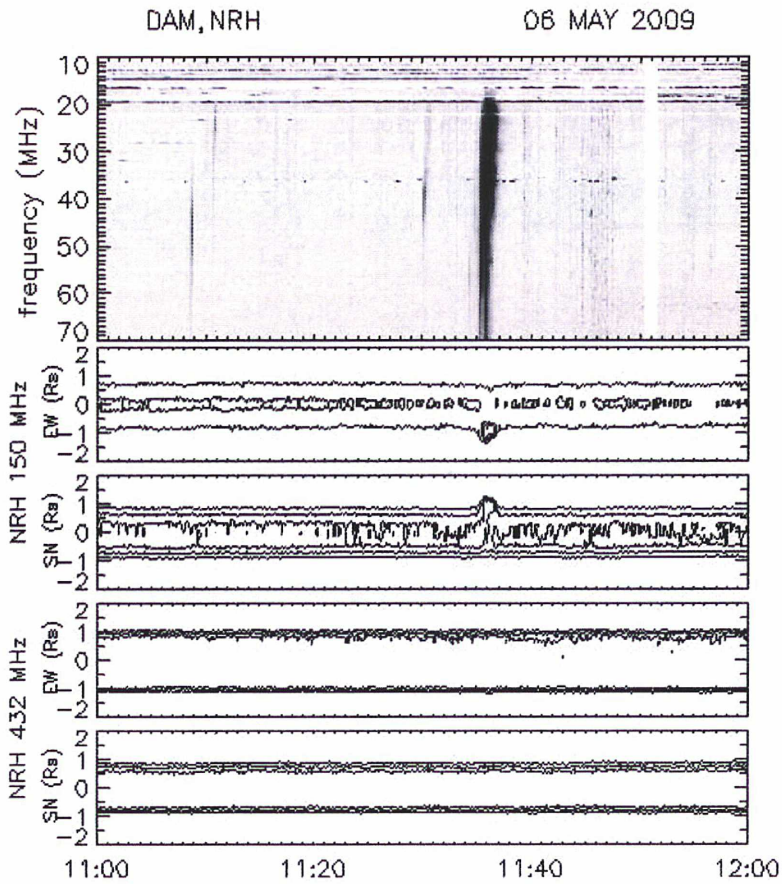

Figure 4.11: Analysis of measurements recorded from 11:00 to 12:00 UT on May 6, 2009: power spectrum from DAM, contour plots of EW and NS brightness distributions from NRT at 150 MHz and 432 MHz (the normalization is made on the maximum intensity in one day, contour levels are then chosen in order to distinguish the quiet sun from intense bursts). Adapted from `http://secchirh.obspm.fr/survey.php?hour=1100&dayofyear=20090506&composite=3`.

4.2 Type III Radio Bursts: Statistical Results

We have manually selected 156 time-frequency intervals when type III radio bursts have been observed by STEREO/Waves between May 2007 and September 2011. The separation angle between spacecraft in the ecliptic plane ranged between 7° (May 2007) and 180° (February 2011). We have included only simple and isolated events (by a visual inspection) when flux density was intense enough for the GP analysis. In order to improve a signal-to-noise ratio we have subtracted receiver background levels from the data before we performed our analysis. These levels have been calculated as median values over one day of the given auto-correlation for each channel/antenna configuration separately (see Section 3.3.1). Finally, we have excluded data points when the difference between maximum and minimum flux density has not exceeded a threshold of 5 dB in the selected time interval for each frequency channel separately. We have investigated only values corresponding to peak fluxes.

Table 4.1 summarizes type III radio bursts included in our statistical survey. The

STEREO-A events	128
STEREO-B events	125
STEREO-A and STEREO-B	97
STEREO-A and not STEREO-B	31
STEREO-B and not STEREO-A	28
Total number of events	**156**

Table 4.1: Number of type III radio bursts included in the statistical survey.

number of radio bursts detected at STEREO-A, and at STEREO-B are in the first and second row, respectively. The third row contains a count of simultaneously observed events. The fourth and fifth rows show events that have been observed only by one spacecraft. The total number of type III radio bursts in our survey is in the last row.

The topmost panel of Figure 4.12 displays the histogram of the observed type III radio bursts vs time at STEREO-A (red line) and STEREO-B (blue line). The bottom panel is the separation angle between STEREO-A and STEREO-B. Although the Sun exhibited an increased activity in 2011 we do not have many events from this period since we include only simple and isolated emissions.

4.2.1 Source Size, Wave Vector Direction, and Polarization

Figure 4.13 summarizes GP results of type III radio bursts during peak fluxes for each frequency channel separately between 125 and 1975 kHz. The topmost panel contains median values of the apparent source size γ vs frequency. We have used the GP inversion described in Section 3.2.1 with an assumption of a Gaussian source brightness distribution (*Krupar et al.*, 2012). The apparent source size γ is very

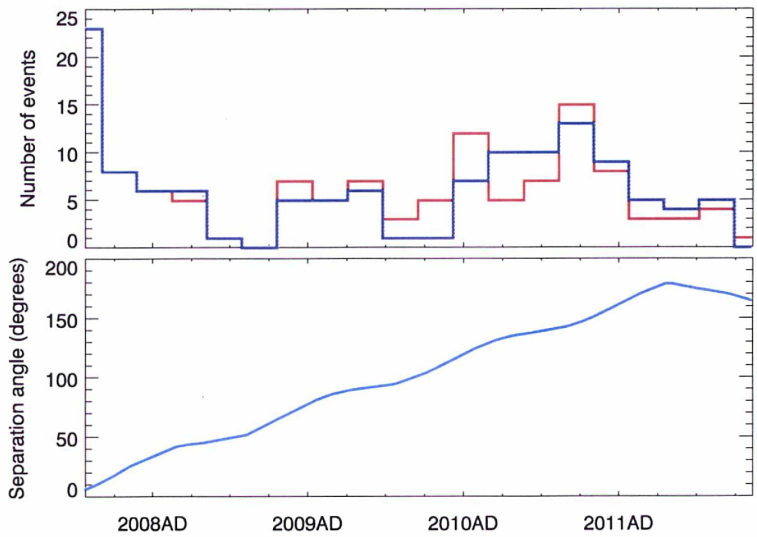

Figure 4.12: The topmost panel is histogram of observed type III radio bursts at STEREO-A (red line) and STEREO-B (blue line) between May 2007 and September 2011. The lower panel displays a separation angle between STEREO-A and STEREO-B.

extended ($\sim$ 40°) for low frequencies ($<$ 500 kHz), while remaining almost constant between 500 kHz and 2 MHz ($\sim$ 25°). It confirms that type III radio bursts have apparently extended sources which can be explained by either properties of an intrinsic beaming pattern and scattering by density fluctuations in the solar wind. We need extensive modeling of refraction and scattering to explain our observations. *Thejappa et al.* (2007) have already performed this modeling for emissions at 120 kHz.

Statistical results on the absolute values of polar angle $|\theta|$ and azimuthal angle $|\phi|$ are shown in the second and third panels, respectively (calculated in RTN coordinates, see Appendix B.3 for details). Deviations of wave vectors κ from the Sun – spacecraft line for the lowest frequencies occur to be about twice larger in the ecliptic plane ($|\phi| \sim 40°$) than in the directions perpendicular to it ($|\theta| \sim 20°$). It confirms that electrons triggering type III bursts statistically propagate along the Parker spiral in the ecliptic.

The fourth panel of Figure 4.13 is the median value of the 2D degree of polarization in the polarization plane C. The 2D degree of polarization is very low ($\sim$ 0.1) being in agreement with previous observations at long wavelengths when type III radio bursts have very low degree of polarization (*Dulk*, 2000). A slight increase of C at low frequencies ($<$ 400 kHz) can be explained by a larger error of the **k**-vector direction estimation in this frequency range (where sources are apparently very extended, see Figure 3.5) as the source position and its polarization are determined simultaneously. However one should note that low values of C being $\sim$ 0.1 are probably linked to the noise. Therefore we can conclude that observed type III radio bursts are nearly unpolarized.

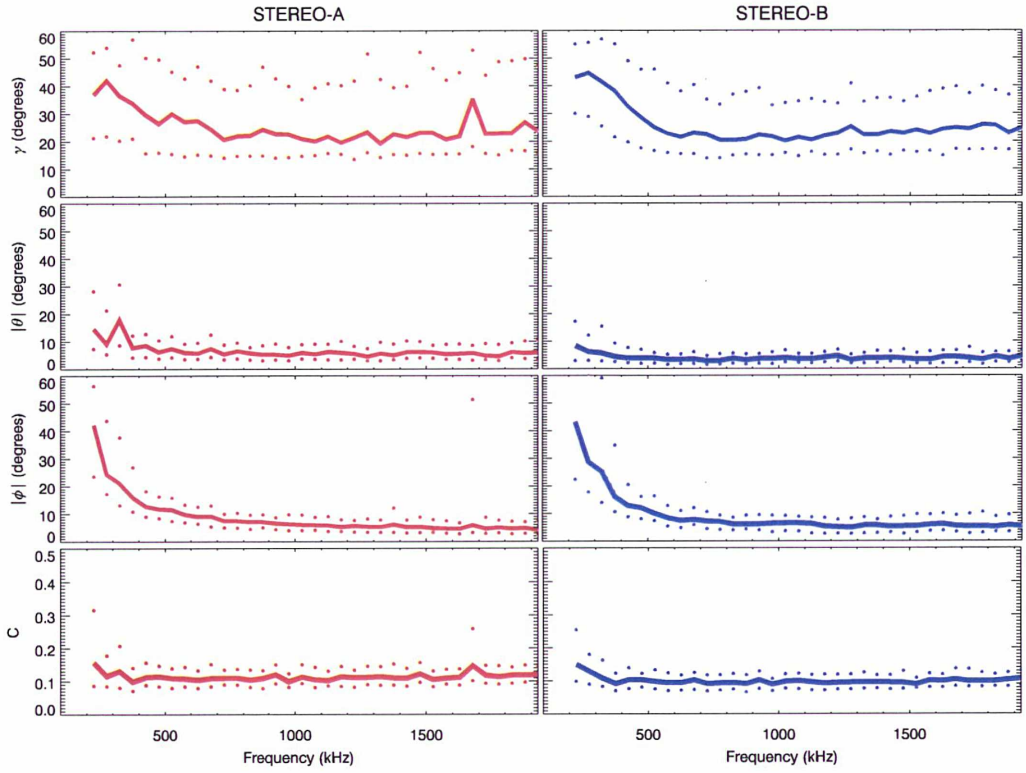

Figure 4.13: Results of the GP inversion at STEREO-A and STEREO-B for 156 type III radio bursts. The topmost row displays the apparent source sizes γ vs frequency. The second row shows deviations of the wave vector from the from the Sun-spacecraft line vs frequency in the ecliptic plane. The third row contains deviations of the wave vector from the from the Sun-spacecraft line vs frequency in the plane perpendicular to the ecliptic one. The last row shows 2D degree of polarization in the polarization plane vs frequency. Solid line are medians and dotted lines represent 25% and 75% quartiles.

4.2.2 Flux Density

First we have identified frequencies corresponding to the maximum flux density for each type III radio burst separately. Table 4.2 contains statistical properties of these maximal frequencies.

We have investigated median values of the flux density S vs frequency between 125 kHz and 16 MHz (Figure 4.14). As the distribution of S at a given frequency has a log-normal character, we have used median values instead of mean ones. The maximum flux density (3×10^{-18} W/m^2/Hz or 3×10^4 sfu) occurs at $\sim$ 1 MHz on both spacecraft. *Bonnin* (2008) has also found maximum around 1 MHz from the *Wind* and Ulysses combined observations.

In order to explain this maximum we have used a simple model of the beam electron density n_{beam} as a function of radial distance from the Sun r:

$$n_{\mathrm{beam}} = \alpha r^{\beta}, \tag{4.1}$$

	STEREO-A	STEREO-B
Mean (kHz)	1505	1435
STD (kHz)	1837	1539
Median (kHz)	925	925
25% quartile (kHz)	525	625
75% quartile (kHz)	2125	1775

Table 4.2: Statistical properties of maximal frequencies of type III radio bursts included in the survey.

where α and β are parameters of the fit. Initially we have assumed that the flux density S is proportional to the quasilinear relaxation growth rate of Langmuir waves γ_k being proportional to $n_{\text{beam}}/\sqrt{n_e(r)}$ (*Drummond and Pines*, 1962, *Vedenov et al.*, 1962, *Kontar*, 2001):

$$S \propto \gamma_k \propto \frac{n_{\text{beam}}(r)}{\sqrt{n_e(r)}} = \frac{\alpha r^{\beta}}{\sqrt{n_e(r)}}. \tag{4.2}$$

The electron density n_e has been retrieved from the model of *Sittler and Guhathakurta* (1999) and is presented in Figure 4.15. We have used a gradient-expansion algorithm to compute a non-linear least squares fit in order to obtain parameters α and β for both spacecraft: $\alpha_{\text{STEREO-A}} = 3.222 \times 10^{-15}$, $\beta_{\text{STEREO-A}} = -1.458$, $\alpha_{\text{STEREO-B}} = 2.187 \times 10^{-15}$, and $\beta_{\text{STEREO-B}} = -1.456$ (yellow dashed line in Figure 4.14). Our results suggest as $\beta \sim -1.5$ that electron beams expand in the IP medium sub-radially.

We now perform the same kind of analysis but assuming a different dependance of the radio flux in the form:

$$S \propto \frac{n_{\text{beam}}(r)}{n_e(r)} = \frac{\alpha r^{\beta}}{n_e(r)}. \tag{4.3}$$

We obtain these coefficients: $\alpha_{\text{STEREO-A}} = 1.246 \times 10^{-11}$, $\beta_{\text{STEREO-A}} = -3.026$, $\alpha_{\text{STEREO-B}} = 8.741 \times 10^{-12}$, and $\beta_{\text{STEREO-B}} = -3.024$. This assumption provides us with a better agreement with the observed S (green dashed line in Figure 4.14). In this case electron beams expand in the IP medium super-radially. One should note that both approaches are very simplified omitting many physical processes such as an efficiency of Langmuir and radio waves conversion, volume of source regions, scattering of radio beams by density fluctuations etc. Nevertheless these results deserve a further investigation.

Indeed we have also used the electron density model of the solar wind (*Sittler and Guhathakurta*, 1999) to determine distances of radio sources from the Sun of type III radio bursts (Figure 4.15). Frequency of 1 MHz corresponds to a radio source located at ~ 8 $R_\odot$ and ~ 14 $R_\odot$ from the Sun for the F and H component, respectively. The plasma density $n(r)$ in the corona decreases faster than r^{-2}, but starting from around ~ 8 $R_\odot$ it decreases as r^{-2}. As the plasma density decreases faster than

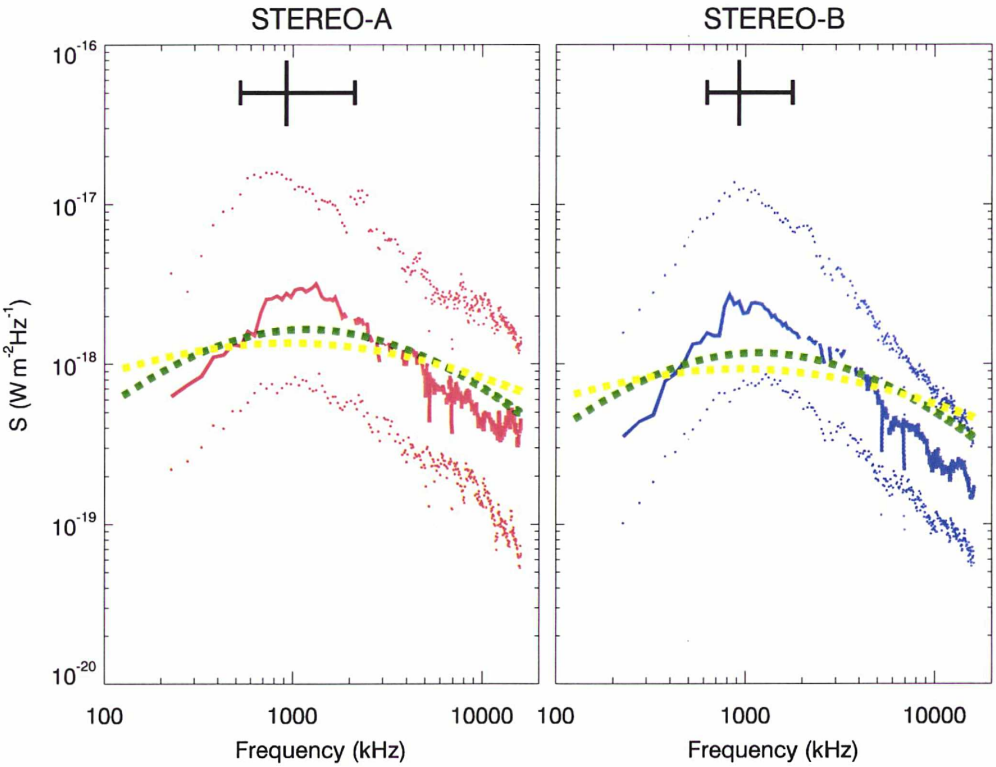

Figure 4.14: Flux density vs frequency at STEREO-A and STEREO-B for 156 type III radio bursts. Solid lines are the medians of the flux for each frequency and dotted lines represent 25% and 75% quartiles. Black crosses on the top denote median and 25% quartile/75% quartile of the maximal frequency from Table 4.2. Yellow and green dashed lines represent results of fitting from equation 4.2 and 4.3, respectively.

r^{-2}, the energy density of Langmuir waves will be growing with distance, but as the density starts to decrease as r^{-2}, the beam continue to spread due to velocity dispersion, we have this maximum.

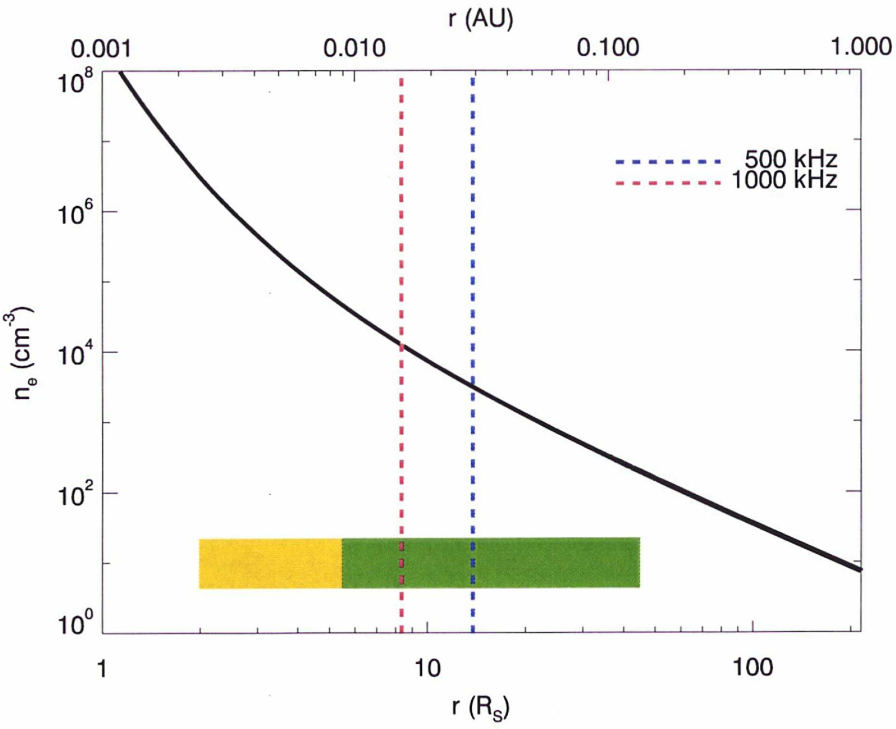

Figure 4.15: Electron density model for average solar wind parameters adapted from *Sittler and Guhathakurta* (1999). A green region indicates frequencies where the HFR instrument (STEREO/Waves) provides us with the GP data while in a yellow region we can retrieve information on wave intensity only. Red and blue dashed lines indicate radial distances from the Sun where electron density corresponds to a plasma frequency of 1 MHz and 500 kHz, respectively.

4.3 Type II Radio Burst triggered by a CME-CME Interaction

As another illustration of the GP techniques developed for S/WAVES we present here the observations of Type II Radio Burst triggered by a CME-CME interaction. Between July 31 and August 2, 2010 the Sun exhibited an increased activity by releasing several CMEs (*Temmer et al.*, 2012, *Schrijver and Title*, 2011, *Liu et al.*, 2012). On August 1, 2010 two CMEs have been observed by coronographs Cor2/SECCHI on-board STEREO (*Howard et al.*, 2008). The slower one erupted at ~2:48 UT while the faster CME followed at ~7:48 UT. The average velocities of the slow and fast CMEs have been derived from Cor2 observations to be 730 km s^{-1} and 1138 km s^{-1}, respectively.

Their interaction resulted in a type II radio burst at ~ 9:00 UT observed by the two STEREO spacecraft and *Wind* spacecraft. This process has been already described as "CME cannibalism" (*Gopalswamy et al.*, 2001). *Martínez Oliveros et al.*

(2012) have performed the GP analysis of this type II radio burst. An accurate time-of-flight examination are in agreement with calculated positions of radio sources. These results have been compared with WL images obtained by Cor2/SECCHI.

Figure 4.16 show two consecutive Cor2/SECCHI/STEREO-B images with over-plotted positions of radio sources obtained by GP analysis the STEREO-B/Waves data. *Martínez Oliveros et al.* (2012) suggest that the type II radio burst is a consequence of the CME — CME interaction. Positions of radio sources obtained by the triangulation confirm their relationship with the CME — CME interaction. More details can be found in Appendix A.3.

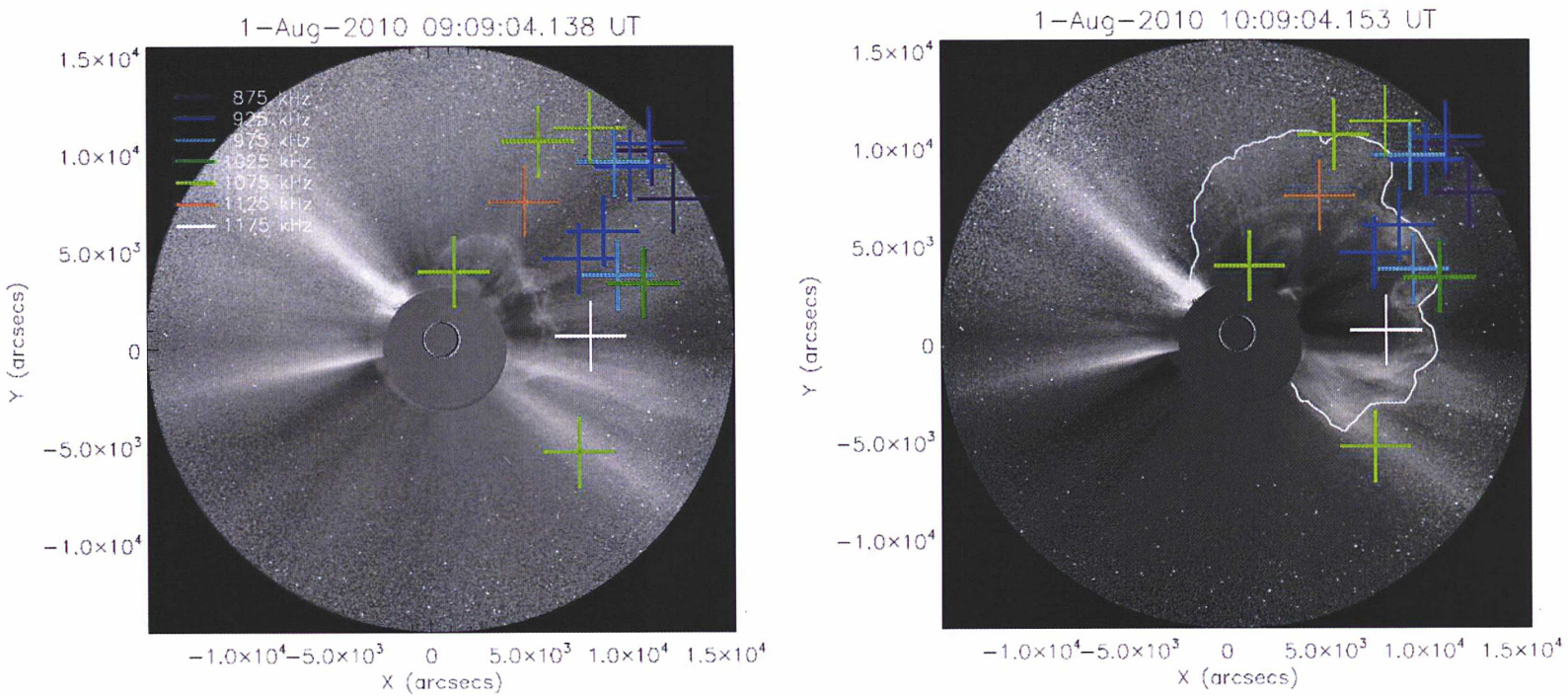

Figure 4.16: Two consecutive Cor2/SECCHI/STEREO-B images from 09:09 UT and 10:09 UT on August 1, 2010. GP results of type II radio burst from STEREO-B/WAVES are overplotted in colors. The solid white line in panel b represents the contour of CME. Adapted from *Martínez Oliveros et al.* (2012).

Chapter 5

Conclusions and Perspectives

In this thesis we have focused on stereoscopic observations of solar radio emissions by the STEREO spacecraft. Our results have been partly published in two scientific journals and two conference proceedings (see Appendix A).

In Chapter 3 we have developed a GP inversion using the SVD technique dedicated for electric measurements on three non-orthogonal antennas performed by three-axis stabilized spacecraft. This inversion may retrieve both wave vector directions and polarization properties of incident waves if observed far from their propagation cut-off.

We have investigated an influence of extended sources on a polarization ellipsoid geometry. Using extensive simulations of electromagnetic emissions with various senses, and degrees of polarization, and source shapes we have derived an empirical relation between apparent source sizes and spectral matrices decomposed by SVD. We have shown that it is not necessary to distinguish the type of polarization to calculate apparent source sizes for emissions with a polarized part below 10% . An error analysis considering receiver inaccuracies has been performed.

Abovementioned methods have been applied to measurements of STEREO which is the first three-axis stabilized spacecraft dedicated to solar observations. We have processed the STEREO/Waves/HFR data in order to confirm a validity of our methods. Several intense type III radio bursts observed by the two STEREO and *Wind* spacecraft have been used for an intercalibration during a period of short separation distances between these spacecraft (May 2007). Results of these joint observations suggest that the GP inversion can be applied on the HFR data. We also conclude that both HFR are well calibrated for intense signals while one should be cautious in a case of weak emissions.

This GP inversion can be also implemented on the RPW instrument onboard the future Solar Orbiter spacecraft which, as STEREO, will be also three-axis stabilized. Three electric antennas of Solar Orbiter are designed to be mounted on booms in a perpendicular plane to the spacecraft — Sun axis. Due to their coupling with the spacecraft body effective directions will be slightly tilted towards the Sun. We have investigated a possible accuracy of the GP inversion with respect to this tilt angle and expected uncertainties of the effective antenna parameters. We conclude that the GP analysis will be possible with the RPW instrument.

In Chapter 4 we present results of analysis solar radio emissions observed by STEREO. We have shown three examples of observations of type III radio bursts from May 2009 when the separation angle between the two STEREO was $\sim 90°$ that allows us to accurately triangulate radio sources. We have found that calculated position of radio sources, relative intensities between the spacecraft, initial flare sites, and differences in onset times are in agreement. We have shown that the triangulation requires the separation angle between the spacecraft being $60° — 120°$ (event 1). Although calculated apparent source sizes are very extended our results indicate that electrons responsible for type III radio bursts propagate along the Parker spiral (event 2). We have also demonstrated that STEREO can be used for stereoscopic investigations of radio sources even if they are located on the far side of the Sun from the Earth's perspective (Event 2). We have also compared STEREO/Waves observations with ground-based measurements of DAM and NRT in Nançay (event 3).

The natural future extension of this work would be to simulate in details and compare to the STEREO observations the propagation of type III radio emissions in the interplanetary medium using (1) an initial radio beam emissions at f_p or $2f_p$, (2) global 3D simulations of the heliospheric density (*Odstrcil and Pizzo*, 2009, *Riley et al.*, 2001), and (3) radio scattering and density fluctuations (*Thejappa et al.*, 2007).

We have performed a statistical survey of isolated 156 type III radio bursts observed by STEREO between May 2007 and September 2011. Statistical results on apparent source sizes which are very extended suggest effects of scattering by density fluctuations in the solar wind. Absolute values of deviations of wave vectors from the Sun – spacecraft line confirm that electrons responsible for type III radio bursts statistically propagate along the Parker spiral in the ecliptic plane. The 2D degree of polarization is very low being in agreement with previous observations of type III radio bursts at long wavelengths. Statistically type III radio bursts exhibit a maximum flux density at $\sim$ 1 MHz. According to electron density models in the solar wind, this frequency corresponds to a radio source located at $\sim$ 8 $R_\odot$ and $\sim$ 14 $R_\odot$ from the Sun for fundamental and harmonic component of type III radio bursts, respectively. Although we have used a very simple model of the electron beam density to interpret the maximum at $\sim$ 1 MHz, we have obtained reasonable results comparable to our observations. We have shown that this maximum is most likely due to the competing effect between the Langmuir waves growth rate and the expansion effects and is related therefore to the respective radial gradients of $n_{\mathrm{beam}}(\mathrm{r})$ and $n_e(r)$. However we plan to perform extensive simulations of the resonant interaction of an electron beam with Langmuir waves to thoroughly explain this maximum.

Abovementioned results on type III radio bursts are planned to be extended and published in a journal.

Appendix A

Publications

Contents

A.1 KRUPAR ET AL., 2010

The apparent source size of type III radio bursts: Preliminary results by the STEREO/WAVES instruments

Krupar, V., M. Maksimovic, O. Santolik, B. Cecconi, Q. N. Nguyen, S. Hoang, and K. Goetz (2010), The apparent source size of type III radio bursts: Preliminary results by the STEREO/WAVES instruments, *Twelfth International Solar Wind Conference — AIP Conference Proceedings*, Volume 1216, pp. 284-287
doi:10.1063/1.3395856

The apparent source size of type III radio bursts: Preliminary results by the STEREO/WAVES instruments

V. Krupar*,†, M. Maksimovic*, O. Santolik†, B. Cecconi*, Q.N. Nguyen*, S. Hoang* and K. Goetz**

*LESIA, UMR CNRS 8109, Observatoire de Paris, Meudon, France
†Academy of Sciences of the Czech republic/Charles University, Prague, Czech Republic
**School of Physics and Astronomy, University of Minnesota, Minneapolis, USA

Abstract. The S/WAVES instrument onboard the STEREO spacecraft measures electromagnetic waves in the solar wind. This unique project allows us to investigate properties of type III and type II radio bursts related to solar flares and propagation of coronal mass ejections (CMEs) in the interplanetary medium, respectively. We have focused on the High Frequency Receiver (HFR; a part of the STEREO/WAVES instrument) which covers the frequency range 125 kHz ~ 16.025 MHz. We present first results of a goniopolarimetric inversion for an extended source using the Singular Value Decomposition technique (SVD). We show a joint observation (including the WIND spacecraft) of the single type III radio burst connected with the X flare as a preliminary example of estimation of the apparent source size and its position.

Keywords: S/WAVES Instrument, Solar Radio Emissions, Singular Value Decomposition technique
PACS: 43.35.Ei, 78.60.Mq

INTRODUCTION

STEREO (Solar TErrestrial RElations Observatory) is the third mission in NASA's Solar Terrestrial Probes program [1]. It consists of two nearly identical spacecraft — one ahead of the Earth in its orbit, and the other one trailing behind. STEREO provides the first stereoscopic measurements of the Sun and the properties of its coronal mass ejections (CMEs). Each spacecraft is three axis stabilized and embarking four scientific instruments: Sun Earth Connection Coronal and Heliospheric Investigation (SECCHI), STEREO/WAVES (SWAVES), In-situ Measurements of Particles and CME Transients (IMPACT) and PLAsma and SupraThermal Ion Composition (PLASTIC). In this paper we discuss the calibration of the STEREO/WAVES High Frequency Receivers (HFR) [2]. One of the primary S/WAVES science goals is to make remote and in-situ measurements that may provide a deeper and more comprehensive understanding of the mechanisms that generate type III solar radio bursts. These bursts, which belong among the most intense radio emissions in the heliosphere [3], are produced by energetic electrons accelerated respectively by interplanetary CME driven shocks and by solar flares. The estimation of apparent source sizes is of prime importance of the type III radio bursts [4]. These source sizes could yield valuable information on the interplanetary density fluctuations taking into account the scattering of the primary radio beam pattern. In order to retrieve goniopolarimetric properties of the radio sources (e.g. their polarization, **k**-vector direction, estimation of the apparent source size) we have to measure accurately the auto- and cross-correlations of the voltages induced by the incident wave electric field, on three quasi-orthogonal antennas [5, 6, 7, 8].

The STEREO/WAVES instrument is composed of four radio receivers or modules:

- The Low Frequency Receiver (LFR): 2.5 ~ 160 kHz
- The High Frequency Receiver (HFR): 125 kHz ~ 16.025 MHz
- The Fixed Frequency Receiver (FFR): 30.025 or 32.025 MHz
- The Time Domain Sampler (TDS): measurements of the Langmuir waves

The LFR and HFR receivers have goniopolarimetric capabilities. HFR is more suitable for the analysis of the type III radio bursts observations. We present preliminary results of a joint observation of a type III radio burst by the WIND spacecraft, located approximately between STEREO-A & STEREO-B, and the two latter. WIND is equipped with the WAVES/WIND instrument [9] which is well-calibrated and has the goniopolarimetric capabilities using the spacecraft spin modulation (spin period $\simeq$ 3 s)[10].

HFR RECEIVER

Three monopole antenna elements (6 meters long each), made from Beryllium – Copper, are used by the S/WAVES instrument to measure the electric field of radio waves [11]. The effective length of antenna can be modeled [12, 13, 14] and as a result of these models, it is estimated to be about 1 meter. The HFR is a dual sweeping receiver operating in the frequency range 125 kHz $\sim$ 16.025 MHz with a 25 kHz effective bandwidth. This duality is necessary for processing auto- and cross-correlations products that are needed for goniopolarimetric measurements. In direction finding mode (see [2] for more details) signals from the Ex and Ey antennas are processed by channel 1. Channel 2 is dedicated to the Ey and Ez antennas. The HFR provides a total dynamic range of 80 dB and its sensitivity at the preamplifier input is 6 nV/Hz$^{1/2}$. Various antenna configurations are available by command. HFR can be switched to use either two pseudo-dipoles (Ey/Ex or Ey/Ez) or monopoles (Ex, Ey or Ez). For this study we are interested in a mode which is a three-step sequence combining successively the three monopoles (Ex – Ey, Ey – Ez and Ex – Ez). Exhaustive ground calibrations have been performed for HFR in order to convert binary telemetry data into physical parameters measured by the sensors.

ESTIMATION OF THE APPARENT SOURCE SIZE OF THE TYPE III RADIO BURST

In this section we perform a direction finding analysis. In order to validate our method we compare the STEREO WAVES observations to those obtained by the WIND spacecraft, as was done recently by Reiner et al. [15].

Cecconi [16] introduced an equation connecting a modeled spectral matrix (that we will compare with the matrix measured by the HFR) with parameters of the antennas configurations (lengths, directions and gains) and initial wave properties (**k**-vector directions, energy flux, Stokes parameters and source angular radius). The shape of the source is considered to be either uniform, radial or Gaussian. We have considered a very small fraction of the polarized part ($\sim$ 0.1 %) and a uniform source. We have applied the Singular Value Decomposition method (SVD)[17] on the modeled matrix $\widehat{\mathbf{A}}$, in order to obtain a relation for the estimation of the apparent source size:

$$\widehat{\mathbf{A}} = \mathbf{U} \cdot \mathbf{W} \cdot \mathbf{V}^T \qquad (1)$$

Using simulated data we have found an empirical relation between the apparent source size and a ratio of the smallest and largest components of the diagonal matrix **W** (see Figure 1).

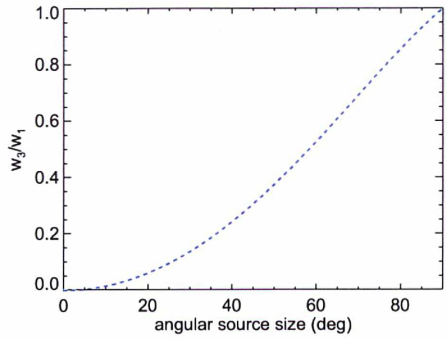

FIGURE 1. The empirical relation between the apparent source size and a ratio of the smallest and largest components of the diagonal matrix **W**.

We have compared above empirical relation applied on the corrected S/WAVES data with the WIND spacecraft. Figure 2 shows the first preliminary results of a joint observation of the single type III radio burst (15:35 – 15:55 UT on the 15 May 2007). The separation angle of the STEREO spacecraft was about 8 degrees only. WIND was located roughly between them, close to the Lagrangian point (L_1). Hence, all the spacecraft should detect almost the same emission. The type III radio burst was probably connected with the X flare located on the Sun at longitude -50 eastward and latitude +9 northward (NOAA number 10956) in HEE coordinates (where zero corresponds to the center of the Sun, the X axis is pointing to the Earth and the Z axis is perpendicular to the Earth's ecliptic plane pointing to the North). The Solar Geophysical Database (http://sgd.ngdc.noaa.gov/sgd/jsp/solarindex.jsp) has been used. We have processed the frequency channel 425 kHz (bandwidth: 25 kHz) on STEREO and 428 kHz (bandwidth: 3 kHz) on WIND. From the Solar wind density model [18] this frequency channels are related to a source region of the solar burst to be approximately at 15 Solar radii from the Sun (considering a fundamental emission at the local plasma frequency) or at 30 Solar radii (for the second harmonic). The topmost panels contain electric field spectral densities from STEREO-A & STEREO-B in mV^2/m^2/Hz, whereas for WIND the signal is in Solar Flux Units (1 sfu=10^{-22} W^2/m^2/Hz at the Earth). We can distinguish an intense peak corresponding the type III radio burst at about the same time. The angular and polarization properties measured by WIND were determined using a technique dedicated to a spinning spacecraft [19], whereas the SVD has been applied on the STEREO data [17].

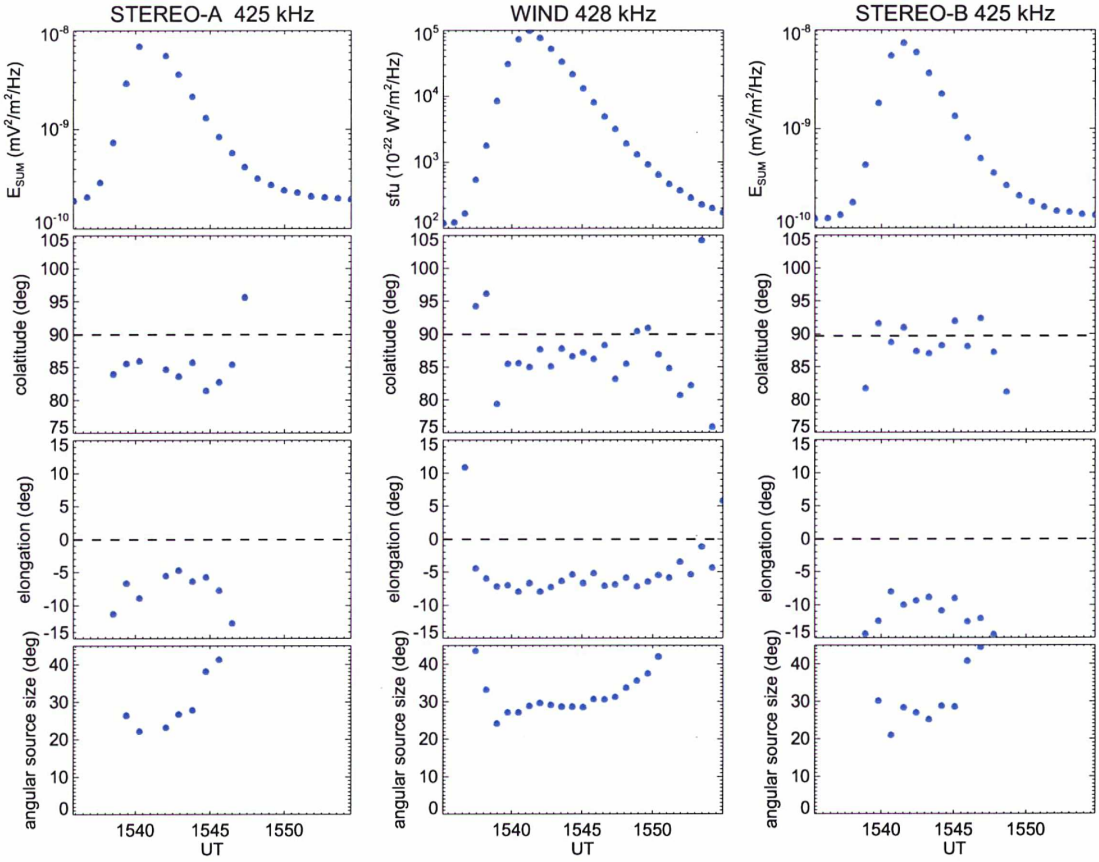

FIGURE 2. From 15:35 to 15:55 UT on the 15 May 2007, the electric field spectral density for STEREO-A (425 kHz), WIND (428 kHz) and STEREO-B (425 kHz), colatitude, elongation and apparent source size.

The second panels show colatitudes in the spacecraft frames (begin is in the the spacecraft, the X axis is pointing to the Sun and the Z axis is perpendicular to the Earth's ecliptic plane pointing to the North) being mostly between 80 and 90 degrees. This corresponds to propagation of the bursts from the northern hemisphere. Elongations measured by all spacecraft vary between 0 and -15 degrees eastward. We have estimated the apparent source size from STEREO-A & STEREO-B to be about 25 degrees during maximum flux considering a uniform source. Globally the source sizes we retrieve for the STEREO spacecraft compare well with those obtained from the WIND spacecraft.

SUMMARY AND CONCLUDING REMARKS

A case study of a single type III radio bursts observation has been presented. The STEREO data have been used to test the empirical relation, between the apparent source size and singular values of the measured spectral matrix, previously identified by analysis of simulated spectral matrices. The results were found to be consistent with the WIND measurements. This method can be used either for statistical studies if robust and fast data processing is needed or for estimation of initial values for a standard non-linear χ^2 method.

ACKNOWLEDGMENTS

The authors thank Pierre-Luc Astier (from LESIA) for providing the S/WAVES data and useful engineering insights on the receiver functions and Xavier Bonnin (also from LESIA) for the association of the observed event with the active region on the Sun. The present work was supported by a scholarship from the French government, a CNRS PICS program, a KONTAKT grant ME9107 and grants GAAV A301120601 and M100420903 from

the Academy of Sciences of the Czech republic. The S/WAVES experiment was built by LESIA with support from both CNES and CNRS.

REFERENCES

1. D. A. Biesecker, D. F. Webb, and O. C. St. Cyr, *Space Science Reviews* **136**, 45–65 (2008).
2. J. L. Bougeret, K. Goetz, M. L. Kaiser, S. D. Bale, P. J. Kellogg, M. Maksimovic, N. Monge, S. J. Monson, P. L. Astier, S. Davy, M. Dekkali, J. J. Hinze, R. E. Manning, E. Aguilar-Rodriguez, X. Bonnin, C. Briand, I. H. Cairns, C. A. Cattell, B. Cecconi, J. Eastwood, R. E. Ergun, J. Fainberg, S. Hoang, K. E. J. Huttunen, S. Krucker, A. Lecacheux, R. J. MacDowall, W. Macher, A. Mangeney, C. A. Meetre, X. Moussas, Q. N. Nguyen, T. H. Oswald, M. Pulupa, M. J. Reiner, P. A. Robinson, H. Rucker, C. Salem, O. Santolik, J. M. Silvis, R. Ullrich, P. Zarka, and I. Zouganelis, *Space Science Reviews* **136**, 487–528 (2008).
3. J. P. Wild, *Australian Journal of Scientific Research A Physical Sciences* **3**, 541 (1950).
4. J. L. Steinberg, S. Hoang, A. Lecacheux, M. G. Aubier, and G. A. Dulk, *Astronomy and Astrophysics* **140**, 39–48 (1984).
5. A. Lecacheux, *Astronomy and Astrophysics* **70**, 701 (1978).
6. H. P. Ladreiter, P. Zarka, and A. Lecacheux, *Planetary and Space Science* **42**, 919–931 (1994).
7. B. Cecconi, and P. Zarka, *Radio Science* **40**, 3003 (2005).
8. B. Cecconi, X. Bonnin, S. Hoang, M. Maksimovic, S. D. Bale, J.-L. Bougeret, K. Goetz, A. Lecacheux, M. J. Reiner, H. O. Rucker, and P. Zarka, *Space Science Reviews* **136**, 549–563 (2008).
9. J.-L. Bougeret, M. L. Kaiser, P. J. Kellogg, R. Manning, K. Goetz, S. J. Monson, N. Monge, L. Friel, C. A. Meetre, C. Perche, L. Sitruk, and S. Hoang, *Space Science Reviews* **71**, 231–263 (1995).
10. M. J. Reiner, Y. Kasaba, M. L. Kaiser, H. Matsumoto, I. Nagano, and J.-L. Bougeret, *Geophysical Research Letters* **24**, 919–922 (1997).
11. S. D. Bale, R. Ullrich, K. Goetz, N. Alster, B. Cecconi, M. Dekkali, N. R. Lingner, W. Macher, R. E. Manning, J. McCauley, S. J. Monson, T. H. Oswald, and M. Pulupa, *Space Science Reviews* **136**, 529–547 (2008).
12. W. Macher, T. H. Oswald, G. Fischer, and H. O. Rucker, *Measurement Science and Technology* **18**, 3731–3742 (2007).
13. T. H. Oswald, W. Macher, H. O. Rucker, G. Fischer, U. Taubenschuss, J. L. Bougeret, A. Lecacheux, M. L. Kaiser, and K. Goetz, *Advances in Space Research* **43**, 355–364 (2009).
14. H. O. Rucker, W. Macher, G. Fischer, T. Oswald, J. L. Bougeret, M. L. Kaiser, and K. Goetz, *Advances in Space Research* **36**, 1530–1533 (2005).
15. M. J. Reiner, K. Goetz, J. Fainberg, M. L. Kaiser, M. Maksimovic, B. Cecconi, S. Hoang, S. D. Bale, and J.-L. Bougeret, *Solar Physics* pp. 100–+ (2009).
16. B. Cecconi, *Radio Science* **42**, 2003–+ (2007).
17. O. Santolík, M. Parrot, and F. Lefeuvre, *Radio Science* **38**, 010000–1 (2003).
18. P. A. Robinson, and I. H. Cairns, *"Solar Physics"* **181**, 429–437 (1998).
19. R. Manning, and J. Fainberg, *Space Science Instrumentation* **5**, 161–181 (1980).

A.2 KRUPAR ET AL., 2011

An Influence of Antenna Tilt Angle to the RPW/Solar Orbiter Direction Finding

Krupar, V., M. Maksimovic, O. Santolik, and B. Cecconi (2011), An Influence of Antenna Tilt Angle to the RPW/Solar Orbiter Direction Finding, *Planetary, Solar and Heliospheric Radio Emissions (PRE VII)*, pp. 389-390

AN INFLUENCE OF ANTENNA TILT ANGLE TO THE RPW/SOLAR ORBITER DIRECTION FINDING

V. Krupar*, M. Maksimovic†, O. Santolik‡, and B. Cecconi†

Extended Abstract

Solar Orbiter is an M-class mission in the ESA Science Programme Cosmic Vision 2015 – 2025 having an orbit with perihelion as low as 0.28 AU. The Radio Plasma Waves (RPW) Analyzer on board will provide new insights into the micro-scale phenomenon, the propagation modes of the radio waves and the localization of their source regions. The three electric antennas (each 5 meters long) are designed to be mounted on booms in a perpendicular plane to the spacecraft-Sun axis. Effective antenna lengths and directions are different from the physical ones due to their coupling with the spacecraft body. These parameters have been investigated considering various antenna placements on the spacecraft body [Rucker et al., this issue]. Results indicate that all effective antenna directions will be slightly tilted towards the Sun.

This paper discusses a possible accuracy of the Direction Finding (DF) with respect to this tilt angle and uncertainties of the effective antenna parameters. We have modeled spectral matrices that represent an unpolarized wave (Stokes parameters: $Q = 0$, $U = 0$, and $V = 0$) propagating from a point source located on the Sun (an apparent source size: $\gamma = 0°$, a wave vector direction: $\theta = 90°$, and $\phi = 90°$) as modeled by Cecconi [2007]. Effective antenna lengths have been assumed to be equal ($h_1 = h_2 = h_3$), while effective antenna directions are varying with respect to the tilt angle ($\xi_1 = 0°$, $\xi_2 = -125°$, and $\xi_3 = 125°$; $\zeta_1 = \zeta_2 = \zeta_3 = 90° - 65°$). We have performed various simulations for each set of parameters considering different sources of errors. The wave vector directions have been calculated using the Singular Value Decomposition method [Santolík et al., 2003; Krupar et al., 2010]. Figure 1a displays a mean difference in estimation of the wave vector directions (deviations from the Sun direction) as a function of the tilt angle ζ. We have used normal distributions of lengths centered on the nominal lengths h_j with sigma$(h_j)/h_j = 0.01, 0.03,$ and 0.05 (dotted, dashed, and solid line, respectively). An error analysis for uncertainty of the effective antenna direction is contained in Figure 1b. We have considered normal distributions of absolute deviations centered on the nominal

* *Faculty of Mathematics and Physics, Charles University, 12116 Prague 2, Czech Republic*
† *LESIA, Observatoire de Paris, UMR CNRS 8109, 92195 Meudon, France*
‡ *Institute of Atmospheric Physics, Academy of Sciences of the Czech Republic, 14131 Prague 4, Czech Republic*

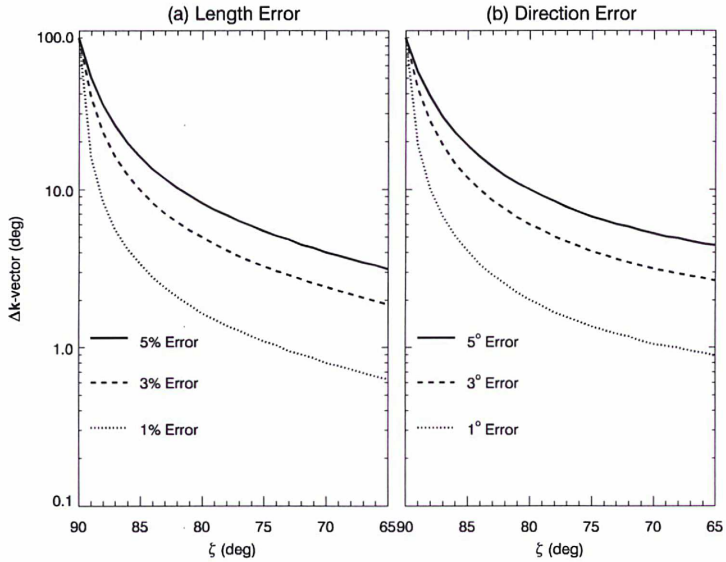

Figure 1: The average difference between input and output wave vector direction as a function of antenna tilt angle ζ.

directions, with sigma$(h_j)/h_j = 0.01, 0.03,$ and 0.05 (dotted, dashed, and solid line, respectively) and uniform distributions of azimuth.

Our results indicate that we need the effective antenna tilt angle of at least $5° - 10°$ to obtain the DF accuracy better than $10°$ with reasonable experimental uncertainties.

References

Cecconi, B., Influence of an extended source on goniopolarimetry (or direction finding) with Cassini and Solar Terrestrial Relations Observatory radio receivers, *Rad. Sci.*, **42**, RS2003, 2007.

Krupar, V., M. Maksimovic, O. Santolik, B. Cecconi, Q. N. Nguyen, S. Hoang, and K. Goetz, The apparent source size of type III radio bursts: Preliminary results by the STEREO/WAVES instruments, 12th Int. Solar wind conference, *AIP Conf. Proc.*, **1216**, 284–287, 2010.

Rucker, H. O., M. Sampl, M. Panchenko, T. Oswald, D. Plettemeier, M. Maksimovic, and W. Macher, Implications of Antenna System Calibration on Spacecraft Design and Radio Data Analysis, in *Planetary Radio Emissions VII*, edited by H. O. Rucker, W. S. Kurth, P. Louarn, and G. Fischer, Austrian Acadademy of Sciences Press, Vienna, this issue, 475–485, 2011.

Santolík, O., M. Parrot, and Lefeuvre, F., Singular value decomposition methods for wave propagation analysis, *Rad. Sci.*, **38**, 1, 2003.

A.3 MARTÍNEZ OLIVEROS ET AL., 2012

The 2010 August 1 Type II Burst: A CME-CME Interaction and its Radio and White-light Manifestations

Martínez Oliveros, J. C., C. L. Raftery, H. M. Bain, Y. Liu, **V. Krupar**, S. Bale, and S. Krucker (2012), The 2010 August 1 Type II Burst: A CME-CME Interaction and its Radio and White-light Manifestations, *The Astrophysical Journal*, Volume 748, pp. 66
doi:10.1088/0004-637X/748/1/66

NOT TO APPEAR IN NONLEARNED J., 45.
Preprint typeset using LaTeX style emulateapj v. 12/16/11

THE 2010 AUGUST 01 TYPE II BURST: A CME–CME INTERACTION, AND ITS RADIO AND WHITE-LIGHT MANIFESTATIONS

JUAN CARLOS MARTÍNEZ OLIVEROS[1], CLAIRE L. RAFTERY[1], HAZEL M. BAIN[1], YING LIU[1], VRATISLAV KRUPAR[2,3], STUART BALE[1,4] AND SÄM KRUCKER[1,5]

Not to appear in Nonlearned J., 45.

ABSTRACT

We present observational results of a type II burst associated with a CME–CME interaction observed in the radio and white-light wavelength range. We applied radio direction-finding techniques to observations from the *STEREO* and *Wind* spacecraft, the results of which were interpreted using white-light coronagraphic measurements for context. The results of the multiple radio-direction finding techniques applied were found to be consistent both with each other and with those derived from the white-light observations of coronal mass ejections (CMEs).The results suggest that the Type II burst radio emission is causally related to the CMEs interaction.

Keywords: solar-terrestrial relations – Sun: coronal mass ejections (CMEs) – Sun: radio radiation,

1. INTRODUCTION

Over periods of increased solar activity, several coronal mass ejections (CMEs) can be launched by the same or nearby active regions (Gopalswamy et al. 2005). During these times of high activity, one or more of these CMEs may interact while propagating through the interplanetary medium. Almost a decade after the rst observations of *CME-associated* shock *regions* (Burlaga et al. 1987), CME–CME interactions were observed, at long wavelengths and in white-light coronagraphic images, by Gopalswamy et al. (2001, 2002) and Gopalswamy (2004). The radio observations were obtained by the Radio and Plasma Wave Experiment (WAVES, Bougeret et al. 1995) on board the *Wind* spacecraft, while the white-light observations were obtained by the Large Angle and Spectroscopic Coronagraph (Brueckner et al. 1995) on board the *Solar and Heliospheric Observatory* mission. Based on the observational characteristics of the CMEs from white-light coronagraph and radio observations, Gopalswamy (2004) concluded that the type II radio emission is enhanced and modified due to the interaction between two CMEs. Gopalswamy et al. (2001) suggested that the observed radio enhancements result from the increased density in the upstream medium that reduces the Alfvén speed, thereby increasing the Mach number of the shock. This is in agreement with results from numerical simulations, confirming that the radio enhancement was likely to be produced at the interaction region shock (e.g., Vandas and Odstrcil 2004). Gopalswamy et al. (2001) also mentioned additional possibilities for electron acceleration, such as reconnection between the two CMEs (see also Gopalswamy 2004).

White-light (WL) imagers such as those on board the *Solar TErrestrial RElations Observatory* (*STEREO*; Kaiser et al. 2008) allow us to observe CMEs out to ~1 AU with the Sun–Earth Connection Coronal and Heliospheric Investigation (SECCHI; Howard et al. 2008). The Cor1 and Cor2 coronagraphs, along with the heliospheric imagers (HI1 and HI2) on board, observe CMEs at visible wavelengths as they propagate through the heliosphere. Coronograph observations typically reveal the three part configuration of CMEs: the bright, dense core that is thought to be the erupting filament; the dark, low density cavity surrounding the core; and the bright front, or the leading edge.

The stereoscopic observations of the *STEREO* mission allow us to determine the location of different CME features in three dimensions (e.g., Frazin et al. 2009; Aschwanden and Wülser 2011; Liu et al. 2009, 2010; Moran et al. 2010). A similar approach can be used to determine the position of radio sources in what is called radio direction-finding. Several direction-finding techniques have been implemented using observations made either by spinning spacecraft like *Wind* (e.g., Fainberg et al. 1972; Reiner et al. 1998) or three-axis stabilized spacecraft such as *STEREO* or *Cassini* (e.g., Cecconi et al. 2008; Santolík et al. 2003). The stereoscopic capability of *STEREO*/WAVES (Bougeret et al. 2008) can be used to triangulate the three dimensional position of a radio source at a particular frequency, provided both spacecraft observe the same source quasi-simultaneously. This process can be repeated for different frequencies. This technique has been applied with great success in the past in the study of type III emission (Gurnett et al. 1978; Reiner et al. 2009) but rarely in the study of type II bursts. Several successful campaigns were undertaken using a combination of spacecraft, such as *Helios*, *Ulysses* and *Wind* (e.g., Baumback et al. 1976; Reiner et al. 1995), demonstrating the success of direction-finding, by mapping the path of accelerated electrons during type III bursts.

In this paper we study the relationship between the interaction of two CMEs and the location of the associated radio sources during an event which occurred on 2010 August 1. We made use of three space-based

[1] Space Sciences Laboratory, University of California, Berkeley, USA
[2] Institute of Atmospheric Physics, Academy of Sciences of the Czech Republic, Prague, Czech Republic
[3] Faculty of Mathematics and Physics, Charles University, Prague, Czech Republic
[4] Physics Department, University of California, Berkeley, USA
[5] Institute of 4D Technologies, School of Engineering, University of Applied Sciences North Western Switzerland, 5210 Windisch, Switzerland

instruments with direction-finding capabilities, namely *STEREO*/WAVES experiments (Kaiser et al. 2008; Bale et al. 2008) and *Wind*, along with white-light data from the SECCHI suite onboard *STEREO*.

2. OBSERVATIONS AND ANALYSIS

The period 2010 July 31 to August 2 was characterized by increased solar activity, exhibiting small flares, filament eruptions and coronal mass ejections (Schrijver and Title 2011; Temmer et al. 2011; Liu et al. 2011). Of particular interest here is the time during which two CMEs (one slow(CME1), erupted at 02:00UT and one fast(CME2), erupted at 07:00UT) interacted with each other, resulting in a low frequency type II radio burst observed on 2010 August 1 at about 09:00 UT). The two CMEs in question can be seen in Figure 1 (left panels - Cor2 A, right panels - Cor2 B). Each row corresponds to a time either before (top and middle rows) or during (bottom rows) the interaction period.

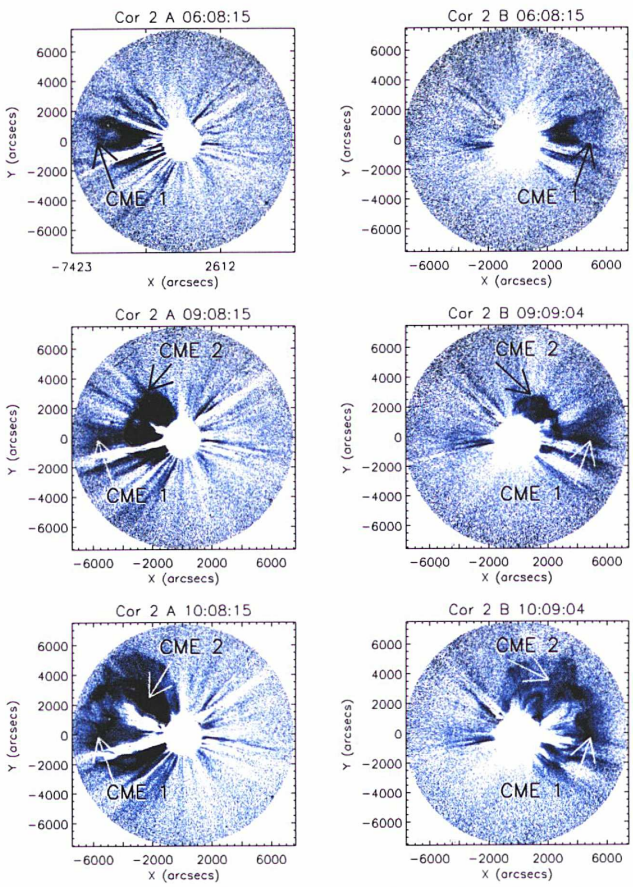

Figure 1. White-light observations of the two CMEs labeled as CME1 and CME2 at three different times during the evolution of the event. The interaction between the CMEs is clearly seen in the bottom frames.

From these white-light observations, we determined the velocity and time of interaction of the expanding CMEs. An elongation map was constructed from running-difference images of Cor2 and HI1 along the ecliptic plane of *STEREO-A* and *-B*, as described in Liu et al. (2010). The filamentary structures in the elongation map (Figure 2) are the propagating CMEs observed in the period 2010 August 1 – 3. Figure 2 shows a fast CME (CME2) that intersects and overtakes a slow CME launched earlier (CME1); the region of interaction is shown by a dashed box. The average speed of the fast CME, derived from Cor2 observations is ∼1138 $\mathrm{km\,s^{-1}}$ with a liftoff time of ∼07:48 UT from the Sun. The liftoff time of the slow CME was calculated to be 02:48 UT with an average propagation velocity of 730 $\mathrm{km\,s^{-1}}$ in Cor2 (Temmer et al. 2011; Liu et al. 2011).

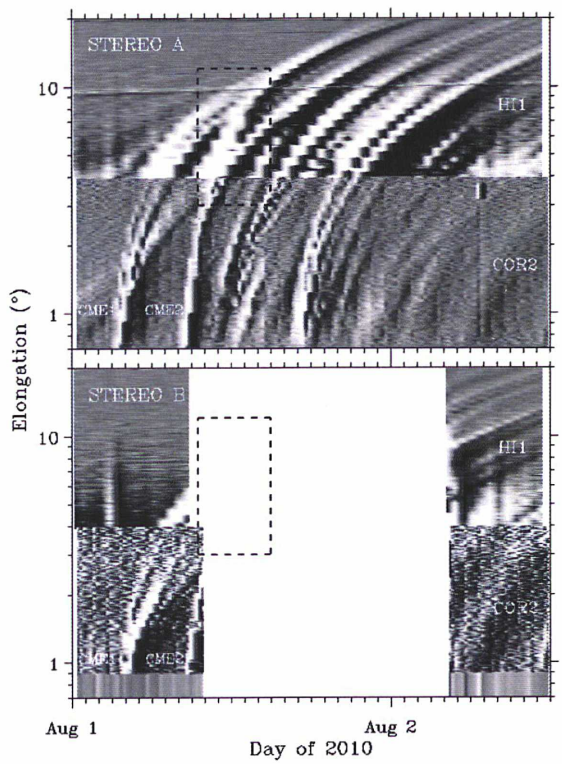

Figure 2. Time−elongation maps constructed from running-difference images of Cor2 and HI1 along the ecliptic plane for *STEREO* A and B. The dashed box shows the interaction region between the two CMEs labeled CME1 and CME2.

Unfortunately, the *STEREO-B* Cor1 and HI1 had a data gap of about 18 hours starting at 9:20 UT, which restricted our analysis. It is important to mention that the speed estimates presented above were obtained using an algorithm that fits the distance with a linear model. These results were then compared to the speed derived from adjacent distances with a three-point Lagrangian interpolation, obtaining similar results. From the Lagrangian algorithm, it is possible to derive the error of the computation giving ± 315 $\mathrm{km\,s^{-1}}$ and ± 206 $\mathrm{km\,s^{-1}}$ for the fast and slow CMEs, respectively. It should be noted that such large errors are present in all methods that measure distances and are not only present in the triangulation method used in this study.

2.1. *Radio emission*

The type II radio burst of interest and its modification by CME interaction is shown in Figure 3. This event was detected simultaneously by both *STEREO* and *Wind* spacecraft. The radio emission was characterized by a slow drifting feature, first observed by *STEREO-B* at about 9:10 UT and ending around 11:30 UT. The drift velocity observed by *Wind*/WAVES, starts at 2000 kHz and ends at about 700 kHz.

As Figure 3 shows, the drifting feature in the radio spectra appears to split into two bands at about 9:50 UT. This may be related to the properties of the ambient plasma or, as we show here, the signatures of two interacting CMEs. We fit the *STEREO*/WAVES radio spectra to determine the propagation velocity and the distance at which the emission could be produced, assuming an interplanetary density model (Leblanc et al. 1998). The radio spectrum was divided in two regions, termed upper and lower branches following the observed division in the spectrogram. Table 1 shows the radial distance to the Sun derived from the model. From the model the drift velocity was calculated (Table 1), revealing that the lower branch has a higher drift velocity, indicating that this part of the type II radio emission was associated with the fast CME (CME2). The upper branch demonstrated a slower drift velocity which is consistent with original velocity of the first and slower CME, indicating that this was the signature of the slow CME or merged CME front.

Distance (AU)

Branch	*STEREO-A*	*STEREO-B*
Lower	0.025 – 0.033	0.022 – 0.036
Upper	0.025 – 0.027	0.025 – 0.027

Velocity ($km\,s^{-1}$)

Branch	*STEREO-A*	*STEREO-B*
Lower	1370	1600
Upper	290	400

Table 1
Estimated radial distances to the Sun and drift velocities derived from Leblanc et al. (1998) density model for both branches in the radio spectra and for each *STEREO* spacecraft.

Since the velocities are determined using an interplanetary density model, the results are highly sensitive to any change of the 1 AU electron density (in the model) used for this computation. An uncertainty estimate of $100-200\ km\,s^{-1}$ was obtained by calculating the speed using the Leblanc et al. (1998) density model for variety of ambient electron density values which range from 4 to $7\ cm^{-3}$ (as observed in in situ data 4 days after the event by *Wind*). These velocities are comparable to the propagation velocities derived from Cor2 observations within the errors of the measurements, suggesting that the split branches observed at 09:50 UT in radio spectra are the signatures of the two interacting CMEs.

2.1.1. *Direction-finding*

This event was observed by three spacecraft which, with radio direction-finding capabilities, gives a unique opportunity to study and locate the region or regions responsible for the radio emission in the interplanetary medium. There are different techniques that allow us to determine the distance at which the emission was produced relative to the observer. Some of these make use of electron density models, as demonstrated in the previous section, which provide a direct correlation between the observed frequency and the distance (height) at which they occur (e.g., Leblanc et al. 1998; Reiner et al. 2007). However, these techniques do not take into account inhomogeneities that may occur in both the interplanetary space and/or the ejected material. Also, the propagation direction cannot be determined by a density model. Other "direction-finding" techniques, which locate the region of emission by triangulating the position of the radio source at distances of ~0.1-0.5 AU, have been developed during the last four decades (e.g., Fainberg et al. 1972; Cecconi et al. 2008; Santolík et al. 2003; Martinez-Oliveros et al. 2012).

We applied eigenvector and singular value decomposition algorithms (Martinez-Oliveros et al. 2012; Santolík et al. 2003, respectively) to determine the arrival direction of radio waves in the frequency range of the High Frequency Receiver 1 instrument onboard *STEREO*. For *Wind*/WAVES data, a modulation technique was applied to retrieve the radio waves' direction of arrival (Fainberg et al. 1972) in the range of the Radio Receiver Band 2. The direction of arrival was then characterized by unitary vectors, defined by the azimuths and elevations found by the direction-finding procedure for all observations in the time range. The spatial positions of the radio sources in interplanetary space were found using a geometrical triangulation algorithm based on Liu et al. (2010). For simplicity, we will refer to the combined direction-finding and triangulation techniques as "direction-finding".

In order to determine the location of the type II radio burst relative to the CMEs, white-light images from SECCHI were used. Data from the Cor2 instrument on board *STEREO* B prior to and at the time of the radio burst were used to compare the projected radio direction-finding results (see Figure 4). This type of comparison has been applied before in the study of type II bursts (e.g., Wagner 1982). The results of our analysis suggest a close relationship between CME – CME interaction region and the type II radio burst. This agrees with the findings of Gopalswamy et al. (2001) who reported a similar result for a different event.

The dual views of the *STEREO* spacecraft were exploited to identify the location of the radio burst in 3D space, relative to the CME structure. Figure 5 shows the front of the CME in heliographic coordinates obtained using the SolarSoft package suite (Freeland and Handy 1998). The three dimensional locations of two CMEs are shown in Figure 5: the position of the slow CME launched at about 02:00 UT is shown as yellow dots, while the position of the fast CME launched at approximately 07:00 UT is represented by blue and green dots. Two evolutionary times are shown, 09:00 and 10:00 UT, as during this period the interaction between the two CMEs occurred, with the fast CME overtaking the slow one slightly after 09:00 UT (see Figure 2). Note that these three-dimensional observations, shown in Figure 5, are projected on the ecliptic plane.

Figure 5 (left) shows the triangulated position of the radio source for the three combinations of *STEREO-A*, -*B* and *Wind* spacecraft at the time of the most prominent peaks in the radio flux for three frequencies (925, 975,

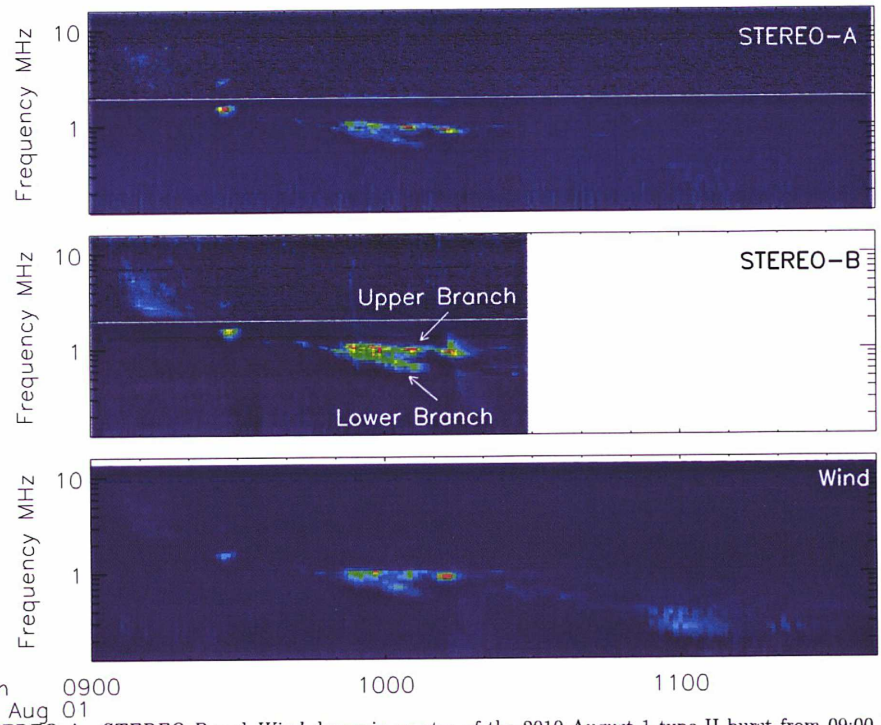

Figure 3. *STEREO-A* , *STEREO-B* and *Wind* dynamic spectra of the 2010 August 1 type II burst from 09:00 UT to 12:00 UT. The plotted frequency range from 125 kHz to 16.025 MHz for *STEREO* and *Wind*. The color shading represents the intensity of the radio emission measured in arbitrary units.

and 1025 kHz[6], see Figure 6).

The apparent misalignment between the triangulated locations from different spacecraft can be explained by understanding that the triangulation algorithm searches for the position in space where the vectors intersect. This intersection does not necessarily occur at the front of the emitting region, or its centroid (Figure 5, right frame). Here, it is likely that the source observed is highly extended and complex. Therefore, each spacecraft identified different regions of the extended source (blue dashed ellipse) due to, e.g. the structure of the region and the surrounding local plasma density. Another possible explanation for the apparent discrepancy is that a dense region was located somewhere between the type II radio source and *STEREO-A*. This region could scatter the radio waves, leading to an apparent shift of the line-of-sight source position.

2.1.2. *Time-of-flight analysis*

We examined the timing of the radio profiles at the three spacecraft as a control technique to validate the locations and results determined by direction-finding. We do this by first computing the distance to each spacecraft from the extrapolated locations. Then, times of flight for each spacecraft are computed assuming that the radio emission travels in a straight line from the source centroid to the spacecraft at a constant velocity (the speed of light). The difference between these two times is compared with the time shift between radio flux profiles at the three spacecraft (see Figure 6) to determine whether they are consistent with the source locations found using the direction-finding method. This "time-of-flight analysis" assumes that the onsets of the signals at the two spacecraft are the signature of radio emission simultaneously emitted from a single compact source. The limitations of this "time-of-flight" analysis are in the temporal resolution of the measurements and errors inherent in the assumptions of compactness and simultaneity.

We find that the time shift (delay) computed from the direction-finding results ranges from $\approx$2 minutes at the lowest frequencies decreasing to $\approx$1 minute at the highest, while the observed delay between the peaks of the emission received by *STEREO-A* and *-B* ranges from $\approx$1 to $\approx$0 minute, respectively. In our analysis we also make use of *Wind* data. Comparing the times of arrivals at the *Wind* and the STEREO spacecraft computed from the direction-finding results, we find an average time delay between $\approx$5.2 minutes and $\approx$1 minute, while the observed time delay between the radio signatures is about $\approx$2 minutes. We found that the direction-finding and the time-of-flight analysis results are consistent within the errors inherent to both techniques. The geometrical configuration suggested by the time-of-flight analysis is consistent to the one obtained by the direction-finding, in which *Wind* is located closer to the radio source that either of the STEREO spacecraft, and also that the radio source is located almost at the same distance from each STEREO spacecraft.

[6] For context, the Parker spiral is plotted in Figure 5 and was calculated using the formula $\phi = \phi_0 - (\Theta_\odot / V_{sw})r$, where r, is the radial distance to the Sun, ϕ_0 is an arbitrary angle, $\theta_\odot$ is the rotational velocity of the Sun (2 km s^{-1}), and V_{sw} is the solar wind velocity (400 km s^{-1}).

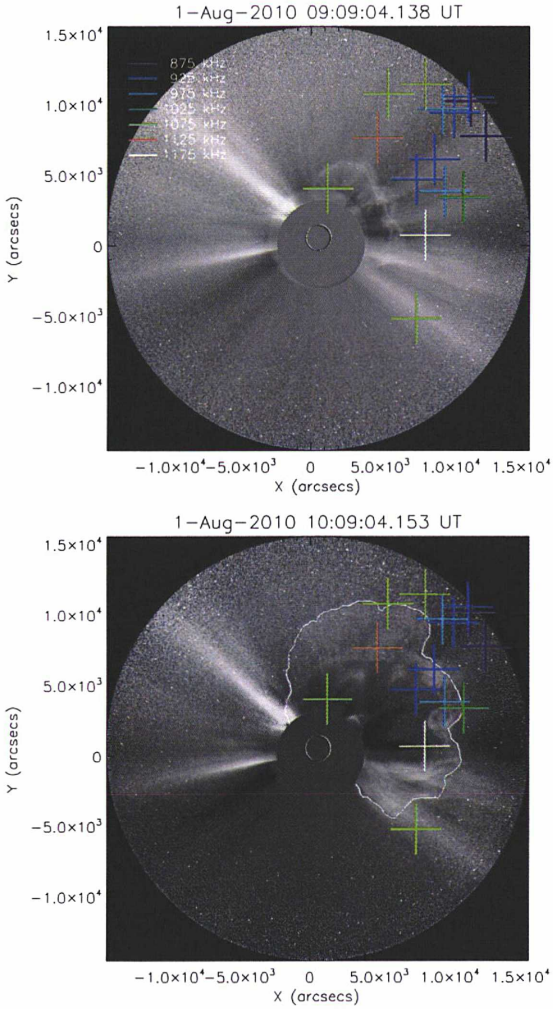

Figure 4. *STEREO-B* observation of the 2010 August 1 CME from Cor2 at two representative times of type II radio burst, 09:09 UT and 10:09 UT, with line-of-sight direction-finding results from *STEREO-B*/WAVES overplotted in color, where color represents different frequencies. The solid white line in lower panel shows the contour of the expanding CME.

3. CONCLUSIONS

During 2010 July 31 – August 2 a series of CMEs and their associated type II and type III radio bursts were observed. In particular, an interplanetary type II burst was detected by instruments onboard the STEREO and *Wind* spacecraft on 2010 August 1 at about 09:00 UT. The close timing between the type II radio burst and the interaction of two coronal mass ejections suggests that the radio emission is a consequence of this interaction. A similar event was analyzed previously by Gopalswamy et al. (2001), who concluded that the interaction between slow CME and a fast one resulted in the enhancement of the radio emission during the transit of the fast CME shock front through the core of the slow CME.

Using white-light and radio observations we estimated the propagation velocities of the two CMEs. We found that the velocities derived from radio observations are comparable to the propagation velocities derived from coronagraph observations. This suggests that the branches in the radio spectra, observed at 09:50 UT, are the signatures of the two interacting CMEs. Using the density model of Leblanc et al. (1998) we also estimated the distance at which the radio emission was produced, was between 0.025 and 0.043 AU. This is in agreement with the radio direction-finding results, which give a distance about 0.01 – 0.05 AU. From white-light observations, we determined that the shock front propagated ~20° east of the Sun – Earth line (i.e. between *STEREO-B* and *Wind*), which is about the same angular separation derived by the direction-finding technique. The obtained propagation direction is in agreement with finding of Temmer et al. (2011) and Liu et al. (2011).

We successfully applied three radio direction-finding techniques (Fainberg et al. 1972; Santolík et al. 2003; Martinez-Oliveros et al. 2012) to the 2010 August 1 type II radio burst and determined the direction of arrival of the radio emission. The data analysis shows that the radio sources locations are spread over a large area covering about 4°, suggesting that the radio source has an extended and complex structure in nature, perhaps composed of multiple radio emitting regions which may have a common origin. We found good consistency between the triangulated white-light positions and the *Wind* – *STEREO-B* triangulated positions. Using STEREO-A, we found a discrepancy that can be explained by the complexity of the source and the surrounding material. Since neither the emitting region nor the medium are homogenous, it is possible that the radio source was partially occulted in the direction of STEREO-A by a dense solar wind region. This may explain the relatively low power observed in the STEREO-A spectrogram and can also account for scattering of radio waves, which consequently will shift the apparent position of the radio source.

By comparing these positions with white-light features in the STEREO coronagraph data and their derived positions as described in Section 2.1.1, we found that the radio emission is the result of the interaction between two expanding CMEs. Figure 4 shows that the positions derived from the direction-finding match the features observed in the coronagraph images, suggesting the relation between the type II radio emission and the interaction region of two expanding CMEs.

Radio direction-finding has proven to be a powerful technique in the study of CMEs and associated type II radio bursts. By using these techniques, it is possible to determine the heliographic distance of a radio source, which is independent of any density model. In general, the limitation of these techniques is given by the frequency of observations and the properties of the radio emission region. In the case of metric wavelengths this error can be about 1° in azimuth and elevation. Nevertheless,our study shows that with good observations, the techniques give results that can be directly compared with observations at other wavelengths and show the likely emission region. The application of radio direction-finding methods to data acquired by future missions, such as Solar Probe Plus and Solar Orbiter, will prove to be crucial in

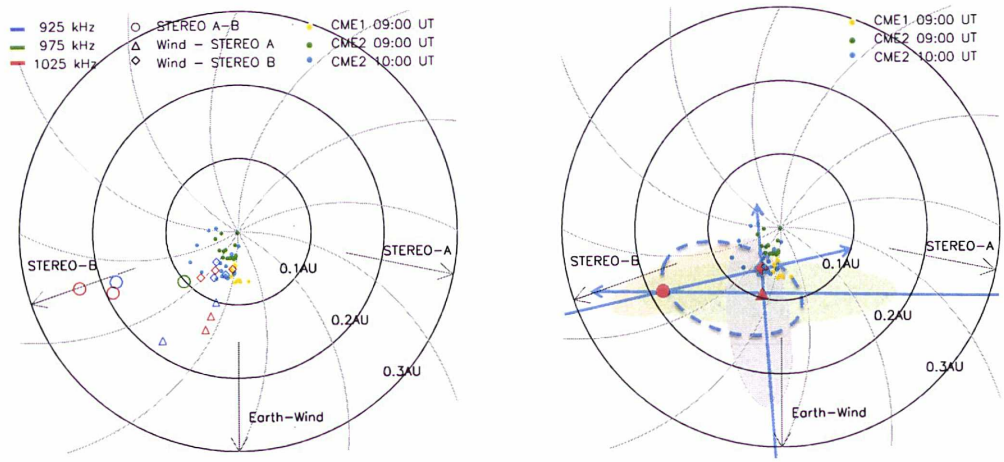

Figure 5. Left: location of the geometrically triangulated positions of the radio sources in interplanetary space for all operational frequencies as seen from the top. The Parker spiral is plotted in gray for context. Right: radio emission scenario, showing the possible emission region as an extended source propagating between *STEREO-B* and *Wind*. The dots represent positions of the two associated coronal mass ejections at different times. The red symbols show the intersection between line-of-sight vectors from the spacecraft represented by the arrows. These are results projected on the ecliptic plane. The overall regions where the direction-nding positions are located are represented by the color shaded areas. The dashed ellipse shows the area covering all direction results.

our understanding of CMEs and type II radio bursts.

REFERENCES

Aschwanden, M. J. and J.-P. Wülser (2011, June). 3-D reconstruction of active regions with STEREO. *Journal of Atmospheric and Solar-Terrestrial Physics 73*, 1082–1095.

Bale, S. D., R. Ullrich, K. Goetz, N. Alster, B. Cecconi, M. Dekkali, N. R. Lingner, W. Macher, R. E. Manning, J. McCauley, S. J. Monson, T. H. Oswald, and M. Pulupa (2008, April). The Electric Antennas for the STEREO/WAVES Experiment. *Space Sci. Rev. 136*, 529–547.

Baumback, M. M., W. S. Kurth, and D. A. Gurnett (1976, June). Direction-finding measurements of type III radio bursts out of the ecliptic plane. *Sol. Phys. 48*, 361–380.

Bougeret, J., M. L. Kaiser, P. J. Kellogg, R. Manning, K. Goetz, S. J. Monson, N. Monge, L. Friel, C. A. Meetre, C. Perche, L. Sitruk, and S. Hoang (1995, February). Waves: The Radio and Plasma Wave Investigation on the Wind Spacecraft. *Space Sci. Rev. 71*, 231–263.

Bougeret, J. L., K. Goetz, M. L. Kaiser, S. D. Bale, P. J. Kellogg, M. Maksimovic, N. Monge, S. J. Monson, P. L. Astier, S. Davy, M. Dekkali, J. J. Hinze, R. E. Manning, E. Aguilar-Rodriguez, X. Bonnin, C. Briand, I. H. Cairns, C. A. Cattell, B. Cecconi, J. Eastwood, R. E. Ergun, J. Fainberg, S. Hoang, K. E. J. Huttunen, S. Krucker, A. Lecacheux, R. J. MacDowall, W. Macher, A. Mangeney, C. A. Meetre, X. Moussas, Q. N. Nguyen, T. H. Oswald, M. Pulupa, M. J. Reiner, P. A. Robinson, H. Rucker, C. Salem, O. Santolik, J. M. Silvis, R. Ullrich, P. Zarka, and I. Zouganelis (2008, April). S/WAVES: The Radio and Plasma Wave Investigation on the STEREO Mission. *Space Sci. Rev. 136*, 487–528.

Brueckner, G. E., R. A. Howard, M. J. Koomen, C. M. Korendyke, D. J. Michels, J. D. Moses, D. G. Socker, K. P. Dere, P. L. Lamy, A. Llebaria, M. V. Bout, R. Schwenn, G. M. Simnett, D. K. Bedford, and C. J. Eyles (1995, December). The Large Angle Spectroscopic Coronagraph (LASCO). *Sol. Phys. 162*, 357–402.

Burlaga, L. F., K. W. Behannon, and L. W. Klein (1987, June). Compound streams, magnetic clouds, and major geomagnetic storms. *J. Geophys. Res. 92*, 5725–5734.

Cecconi, B., X. Bonnin, S. Hoang, M. Maksimovic, S. D. Bale, J. Bougeret, K. Goetz, A. Lecacheux, M. J. Reiner, H. O. Rucker, and P. Zarka (2008, April). STEREO/Waves Goniopolarimetry. *Space Science Reviews 136*, 549–563.

Fainberg, J., L. G. Evans, and R. G. Stone (1972, November). Radio Tracking of Solar Energetic Particles through Interplanetary Space. *Science 178*, 743–745.

Frazin, R. A., M. Jacob, W. B. Manchester, H. Morgan, and M. B. Wakin (2009, April). Toward Reconstruction of Coronal Mass Ejection Density from Only Three Points of View. *ApJ 695*, 636–641.

Freeland, S. L. and B. N. Handy (1998, October). Data Analysis with the SolarSoft System. *Sol. Phys. 182*, 497–500.

Gopalswamy, N. (2004, December). Recent advances in the long-wavelength radio physics of the Sun. *Planet. Space Sci. 52*, 1399–1413.

Gopalswamy, N., S. Yashiro, M. L. Kaiser, R. A. Howard, and J. Bougeret (2001, February). Radio Signatures of Coronal Mass Ejection Interaction: Coronal Mass Ejection Cannibalism? *ApJ 548*, L91–L94.

Gopalswamy, N., S. Yashiro, S. Krucker, and R. A. Howard (2005). CME Interaction and the Intensity of Solar Energetic Particle Events. In K. Dere, J. Wang, & Y. Yan (Ed.), *Coronal and Stellar Mass Ejections*, Volume 226 of *IAU Symposium*, pp. 367–373.

Gopalswamy, N., S. Yashiro, G. Michałek, M. L. Kaiser, R. A. Howard, D. V. Reames, R. Leske, and T. von Rosenvinge (2002, June). Interacting Coronal Mass Ejections and Solar Energetic Particles. *ApJ 572*, L103–L107.

Gurnett, D. A., M. M. Baumback, and H. Rosenbauer (1978, February). Stereoscopic direction finding analysis of a type III solar radio burst - Evidence for emission at 2f/p-/. *J. Geophys. Res. 83*, 616–622.

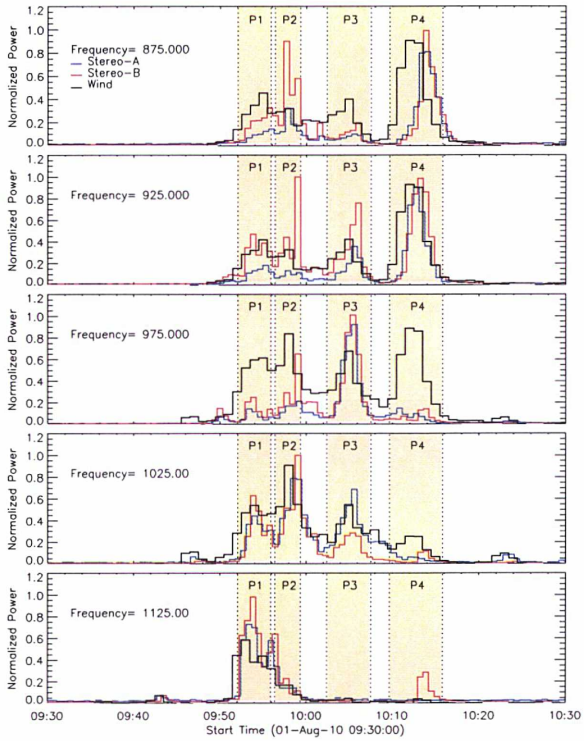

Figure 6. Type II radio burst flux at the observational frequencies. The shaded areas show the most significant peaks of the radio emission. The flux was normalized by the maximum in the observational interval.

Howard, R. A., J. D. Moses, A. Vourlidas, J. S. Newmark, D. G. Socker, S. P. Plunkett, C. M. Korendyke, J. W. Cook, A. Hurley, J. M. Davila, W. T. Thompson, O. C. St Cyr, E. Mentzell, K. Mehalick, J. R. Lemen, J. P. Wuelser, D. W. Duncan, T. D. Tarbell, C. J. Wolfson, A. Moore, R. A. Harrison, N. R. Waltham, J. Lang, C. J. Davis, C. J. Eyles, H. Mapson-Menard, G. M. Simnett, J. P. Halain, J. M. Defise, E. Mazy, P. Rochus, R. Mercier, M. F. Ravet, F. Delmotte, F. Auchere, J. P. Delaboudiniere, V. Bothmer, W. Deutsch, D. Wang, N. Rich, S. Cooper, V. Stephens, G. Maahs, R. Baugh, D. McMullin, and T. Carter (2008, April). Sun Earth Connection Coronal and Heliospheric Investigation (SECCHI). *Space Science Reviews 136*, 67–115.

Kaiser, M. L., T. A. Kucera, J. M. Davila, O. C. St. Cyr, M. Guhathakurta, and E. Christian (2008, April). The STEREO Mission: An Introduction. *Space Science Reviews 136*, 5–16.

Leblanc, Y., G. A. Dulk, and J. Bougeret (1998, November). Tracing the Electron Density from the Corona to 1au. *Sol. Phys. 183*, 165–180.

Liu, Y., J. A. Davies, J. G. Luhmann, A. Vourlidas, S. D. Bale, and R. P. Lin (2010, February). Geometric Triangulation of Imaging Observations to Track Coronal Mass Ejections Continuously Out to 1 AU. *ApJ 710*, L82–L87.

Liu, Y., J. Luhmann, C. Möstl, J. Martinez-Oliveros, S. Bale, R. Lin, R. Harrison, and M. Temmer (2011, November). Interactions between Coronal Mass Ejections Viewed in Coordinated Imaging and In Situ Observations. *ApJ 746*, L15.

Liu, Y., J. G. Luhmann, S. D. Bale, and R. P. Lin (2009, February). Relationship Between a Coronal Mass Ejection-Driven Shock and a Coronal Metric Type II Burst. *ApJ 691*, L151–L155.

Liu, Y., A. Thernisien, J. G. Luhmann, A. Vourlidas, J. A. Davies, R. P. Lin, and S. D. Bale (2010, October). Reconstructing Coronal Mass Ejections with Coordinated Imaging and in Situ Observations: Global Structure, Kinematics, and Implications for Space Weather Forecasting. *ApJ 722*, 1762–1777.

Martinez-Oliveros, J. C., C. Lindsey, S. D. Bale, and S. Krucker (2012). Determination of Electromagnetic Source Direction and Polarization as an Eigenvalue Problem. *Sol. Phys.* in preparation.

Moran, T. G., J. M. Davila, and W. T. Thompson (2010, March). Three-Dimensional Polarimetric Coronal Mass Ejection Localization Tested Through Triangulation. *ApJ 712*, 453–458.

Reiner, M. J., J. Fainberg, and R. G. Stone (1995, April). Interplanetary Type III Radio Bursts Observed from High Southern Heliographic Latitudes. *Space Sci. Rev. 72*, 255–260.

Reiner, M. J., K. Goetz, J. Fainberg, M. L. Kaiser, M. Maksimovic, B. Cecconi, S. Hoang, S. D. Bale, and J. Bougeret (2009, October). Multipoint Observations of Solar Type III Radio Bursts from STEREO and Wind. *Sol. Phys. 259*, 255–276.

Reiner, M. J., M. L. Kaiser, and J.-L. Bougeret (2007, July). Coronal and Interplanetary Propagation of CME/Shocks from Radio, In Situ and White-Light Observations. *ApJ 663*, 1369–1385.

Reiner, M. J., M. L. Kaiser, J. Fainberg, and R. G. Stone (1998, December). A new method for studying remote type II radio emissions from coronal mass ejection-driven shocks. *J. Geophys. Res. 103*, 29651–29664.

Santolík, O., M. Parrot, and F. Lefeuvre (2003, February). Singular value decomposition methods for wave propagation analysis. *Radio Science 38*(1), 010000–1.

Schrijver, C. J. and A. M. Title (2011, April). Long-range magnetic couplings between solar flares and coronal mass ejections observed by SDO and STEREO. *Journal of Geophysical Research (Space Physics) 116*, 4108.

Temmer, M., B. Vršnak, T. Rollett, B. Bein, C. deKoning, Y. Liu, E. Bosman, C. Möstl, R. Harrison, N. Nitta, M. Bisi, J. Davies, A. Veronig, O. Flor, J. Eastwood, D. Odstrcil, V. Bothmer, R. Forsyth, and T. Howard (2011, November). Behavior of CME kinematics during the 2010 August 1 CME-CME interaction event. *ApJ*, submitted.

Vandas, M. and D. Odstrcil (2004, February). Acceleration of electrons by interacting CMEs. *A&A 415*, 755–761.

Wagner, W. J. (1982). Serf studies of mass motions arising in flares. *Advances in Space Research 2*, 203–219.

A.4 KRUPAR ET AL., 2012

Goniopolarimetric inversion using SVD: an application to type III radio bursts observed by STEREO

Krupar, V., O. Santolik, B. Cecconi, M. Maksimovic, X. Bonnin, M. Panchenko, and A. Zaslavsky (2012), Goniopolarimetric inversion using SVD: An application to type III radio bursts observed by STEREO, *Journal of Geophysical Research*, Volume 117, pp. 284-287
10.1029/2011JA017333

Goniopolarimetric inversion using SVD: An application to type III radio bursts observed by STEREO

V. Krupar,[1,2,3] O. Santolik,[2,3] B. Cecconi,[1] M. Maksimovic,[1] X. Bonnin,[1] M. Panchenko,[4] and A. Zaslavsky[1]

Received 4 November 2011; revised 27 March 2012; accepted 2 April 2012; published 5 June 2012.

[1] Type III radio bursts are intense solar radio emissions generated by beams of energetic electrons injected into the interplanetary medium. They can be routinely observed by the S/Waves instruments on-board the STEREO (Solar Terrestrial Relation Observatory) spacecraft. We describe goniopolarimetric (GP) inversion of a signal measured on non-orthogonal antennas using the Singular Value Decomposition (SVD) technique. This wave propagation analysis can be applied to spectral matrices built from measurements by the High Frequency Receiver (HFR; a part of the S/Waves experiment). We have found an empirical relation between the decomposed spectral matrices and apparent source sizes for waves with a low degree of polarization. Simulations of electromagnetic emissions with various senses and degrees of polarization, and source shapes show that SVD gives us reasonable results with respect to the polarization ellipsoid geometry. An error analysis considering inaccuracies of HFR has been performed in order to test the validity of the **k**-vector direction estimation and the obtained empirical relation. We present a joint observation of a type III radio burst by the STEREO and *Wind* spacecraft during small separation distances. We obtain consistent results for the **k**-vector direction and apparent source size using different analysis methods for the measurements of the STEREO and *Wind* spacecraft. We demonstrate that SVD can be an effective tool for the wave analysis of radio emissions measured on non-orthogonal antennas even with very extended sources.

Citation: Krupar, V., O. Santolik, B. Cecconi, M. Maksimovic, X. Bonnin, M. Panchenko, and A. Zaslavsky (2012), Goniopolarimetric inversion using SVD: An application to type III radio bursts observed by STEREO, *J. Geophys. Res.*, *117*, A06101, doi:10.1029/2011JA017333.

1. Introduction

[2] Type III radio bursts are among the most intense electromagnetic emissions in the heliosphere [*Wild*, 1950] . They are generated by beams of suprathermal electrons (~0.1c) accelerated near the Sun's surface and streaming outward along the open magnetic field lines and connected with solar flares and/or coronal mass ejections (CMEs) driven shocks. The electron beams, when they pass through the medium along the Parker spiral magnetic field lines, produce locally a bump-on-tail instability in the local electron distribution function. This change of plasma parameters can lead to generation of electrostatic Langmuir waves at the local plasma frequency f_p, which can be afterwards converted by a nonlinear conversion into electromagnetic waves: type III radio bursts. This conversion involves interaction with low frequency plasma waves and/or scattering at ion density fluctuations resulting in radio bursts at f_p (fundamental emission) and/or $2f_p$ (harmonic emission) beamed tangent to the Parker spiral. Although a basis of this conversion has been formulated by *Ginzburg and Zhelezniakov* [1958], the whole process is still not well understood and several theories remain under debate, e.g., stochastic-growth theory (SGT) [*Cairns and Robinson*, 1995]. As electron beams propagate outward from the Sun, these emissions are generated at lower frequencies corresponding to a decreasing of f_p which is related to the local plasma density: $f_p(\mathrm{kHz}) \approx 9\sqrt{\mathrm{n}(\mathrm{cm}^{-3})}$. Type III radio bursts display maximal flux density approximately at 1 MHz [*Weber*, 1978]. In comparison with other electromagnetic emissions, their sources are apparently extended [*Steinberg et al.*, 1984, 1985; *Bonnin et al.*, 2008], which can be explained by either properties of an intrinsic beaming pattern and/or scattering by density fluctuations of the interplanetary medium. Hence an estimation of their apparent

[1]Laboratoire d'Etudes Spatiales et d'Instrumentation en Astrophysique, UMR CNRS 8109, Observatoire de Paris, Meudon, France.
[2]Faculty of Mathematics and Physics, Charles University, Prague, Czech Republic.
[3]Institute of Atmospherical Physics, Czech Academy of Science, Prague, Czech Republic.
[4]Space Research Institute, Austrian Academy of Sciences, Graz, Austria.

Corresponding author: V. Krupar, Laboratoire d'Etudes Spatiales et d'Instrumentation en Astrophysique, UMR CNRS 8109, Observatoire de Paris, 5, Place Jules Janssen, F-92195 Meudon CEDEX, France. (vratislav.krupar@obspm.fr)

0148-0227/12/2011JA017333

source size could yield important information about density fluctuations in the solar wind. Although coronal type III radio bursts ($f \sim 200$ MHz) can have up to 35% of the circular polarization, the degree of polarization of type III radio bursts at long wavelengths ($f \sim 1$ MHz) is negligible [*Dulk*, 2000]. Multipoint observations of type III radio bursts using goniopolarimetric (GP, also referred to as direction-finding) products have already been obtained by spinning spacecraft [*Gurnett et al.*, 1978; *Manning and Fainberg*, 1980; *Hoang et al.*, 1981]. This paper presents general GP methods for three axis stabilized spacecraft.

[3] For determining the wave vector (**k**) directions and polarization parameters we need instruments allowing multicomponent measurements of auto-correlations and cross-correlations of the voltages induced by the wave electric and/or magnetic field. These instruments provide us with the GP data, which can be used for advanced analysis of an incoming wave [*Lecacheux*, 1978; *Ladreiter et al.*, 1995; *Cecconi et al.*, 2008]. With such data we are able to compose an orthogonal spectral matrix S_{ij} containing the information about the incident wave:

$$S_{ij} = \left\langle E_i E_j^* \right\rangle, \tag{1}$$

where E_k is a vector of complex amplitudes, indices i and j represent three Cartesian components, $\langle\rangle$ means time averaging on a time interval much longer than the observed wave period and * corresponds to a complex conjugate. The Singular Value Decomposition (SVD) is an efficient tool for wave analysis [*Santolík et al.*, 2003] that can be directly utilized on a 6×3 matrix **A** containing separated real and imaginary parts of a 3×3 complex spectral matrix S_{ij}:

$$A = \begin{pmatrix} S_{11} & \mathcal{R}e(S_{12}) & \mathcal{R}e(S_{13}) \\ \mathcal{R}e(S_{12}) & S_{22} & \mathcal{R}e(S_{23}) \\ \mathcal{R}e(S_{13}) & \mathcal{R}e(S_{23}) & S_{33} \\ 0 & -\mathcal{I}m(S_{12}) & -\mathcal{I}m(S_{13}) \\ \mathcal{I}m(S_{12}) & 0 & -\mathcal{I}m(S_{23}) \\ \mathcal{I}m(S_{13}) & \mathcal{I}m(S_{23}) & 0 \end{pmatrix}. \tag{2}$$

Applying SVD on this special real form of the complex spectral matrix we obtain real matrices **U**, **W** and $\mathbf{V}^T$:

$$\mathbf{A} = \mathbf{U} \cdot \mathbf{W} \cdot \mathbf{V}^T. \tag{3}$$

The SVD inversion retrieves information about the axis directions/lengths of the polarization ellipsoid (the wave vector direction/ellipticity) and estimators of the planarity of polarization. The **U** matrix is a 6×3 matrix with orthonormal columns used in the decomposition of **A**. Polarization properties and estimation of an angular source size are defined by the matrix **W**, which is a diagonal matrix 3×3 of three positive or null singular values that represent the axis lengths of the polarization ellipsoid. The 3×3 matrix $\mathbf{V}^T$ with orthonormal rows contains directions of the axes of the polarization ellipsoid. This method was originally designed for 3×3 magnetic spectral matrices by assuming that $\mathbf{B} \cdot \mathbf{k} = 0$ [*Santolík et al.*, 2003]. It can also be used for electric spectral matrices if the condition $\mathbf{E} \cdot \mathbf{k} = 0$ is fulfilled, which is the case of radio waves when observed far from their propagation mode cutoff.

[4] The influence of extended sources on the measured spectral matrix, which are typical for type III radio bursts at long wavelengths, has been efficiently described by *Cecconi* [2007] in equations (4)–(10):

$$\begin{aligned} P_{ij} = \frac{Z_0 G h_i h_j S_0}{2} \Bigg[& (1+Q)\left(A_i A_j \frac{\Gamma_2}{2} + C_i C_j \left(\Gamma_1 - \frac{\Gamma_2}{2}\right)\right) \\ & + (U - iV)\left(A_i B_j \frac{\Gamma_2}{2}\right) + (U + iV)\left(A_j B_i \frac{\Gamma_2}{2}\right) \\ & + (1-Q)\left(A_i A_j \frac{1}{2}\left(\Gamma_1 - \Gamma_2 + \frac{\Gamma_3 + \Gamma_1}{4}\right)\right. \\ & \left. + B_i B_j \frac{1}{2}\left(\Gamma_1 + \frac{\Gamma_3 + \Gamma_1}{4}\right) + C_i C_j \left(\frac{\Gamma_2}{2} - \frac{\Gamma_3 + \Gamma_1}{4}\right)\right)\Bigg], \end{aligned} \tag{4}$$

$$A_k = -\sin\theta_k \cos\theta \cos(\phi - \phi_k) + \cos\theta_k \sin\theta, \tag{5}$$

$$B_k = -\sin\theta_k \sin(\phi - \phi_k), \tag{6}$$

$$C_k = \sin\theta_k \sin\theta \cos(\phi - \phi_k) + \cos\theta_k \cos\theta, \tag{7}$$

$$\Gamma_k^a(\gamma) = \frac{1}{1 - \cos\gamma} \int_0^\gamma \sin(k\theta'_M) d\theta'_M = \frac{1 - \cos(k\gamma)}{k(1 - \cos\gamma)}, \tag{8}$$

$$\Gamma_k^b(\gamma) = \frac{3}{2} \frac{1}{1 - \cos\gamma} \int_0^\gamma \left(1 - \frac{\tan^2\theta'_M}{\tan^2\gamma}\right)^{1/2} \cdot \sin(k\theta'_M) d\theta'_M, \tag{9}$$

$$\Gamma_k^c(\gamma) = \frac{\ln 2}{1 - \cos\gamma} \int_0^{\pi/2} \exp\left(-\ln(2) \frac{\tan^2\theta'_M}{\tan^2\gamma}\right) \cdot \sin(k\theta'_M) d\theta'_M. \tag{10}$$

[5] The P_{ij} matrix on the left hand side of equation (4) represents a modeled spectral matrix that we will compare with the matrix measured by the instrument. P_{ij} is generally a non-orthogonal matrix unlike S_{ij} defined in equation (1). The right hand side of equation (4) contains the impedance of free space (Z_0); parameters of the electrical antennas: effective lengths (h_k), directions (θ_k and ϕ_k) and gain (G); and incident wave properties: the **k**-vector directions (θ and ϕ), the Stokes parameters (the energy flux: S_0; the linear polarization degrees: Q and U; and the circular polarization degree: V) [*Kraus*, 1966] and the angular half aperture of the source (γ), as seen by a spacecraft and contained in the Γ_k coefficients. The shape of the source (see Figure 1), that reflects a radial cut of a source brightness distribution, is considered to be either uniform (equation (8): model 1a), spherical (equation (9): model 1b) or Gaussian (equation (10): model 1c).

[6] In this paper we present results of a GP inversion using the SVD technique considering extended sources of solar radio emissions. In section 2 we describe an empirical relationship between a decomposed spectral matrix and the apparent source size in more detail regarding features of type III radio bursts at long wavelengths. An extensive application of SVD to simulated data with various properties of a source is shown in section 3. Section 4 contains an application of SVD on a single type III radio burst observed by

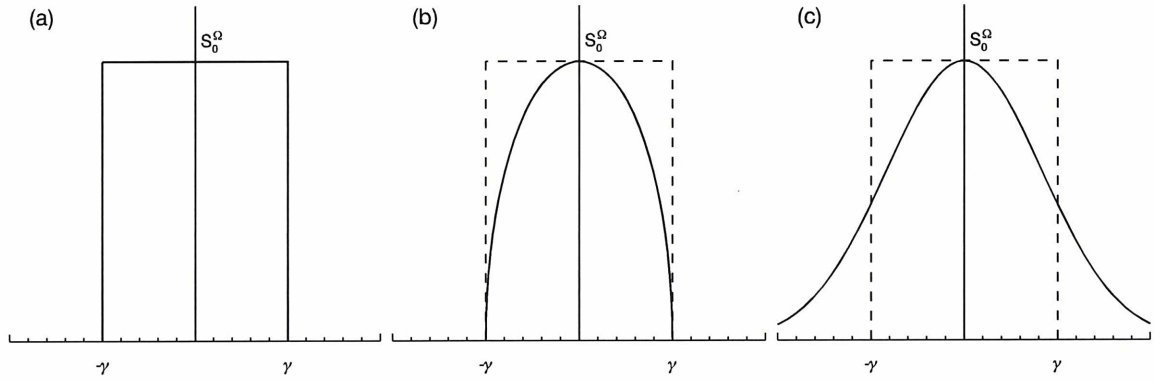

Figure 1. Radial cuts of three source brightness distributions: (a) uniform source, (b) spherical source, and (c) Gaussian source (adapted from *Cecconi* [2007]).

the Solar Terrestrial Relation Observatory (STEREO) and *Wind* spacecraft during small separation distances. We show that results obtained from *Wind* using different techniques (designed for spinning spacecraft) are consistent with the results of the SVD analysis of STEREO data. Finally we discuss an application of the SVD method for the radio emissions with extended sources.

2. Determination of the Source Direction, Coherence and Apparent Size

[7] As already mentioned above, SVD is an efficient method for a wave analysis of multicomponent measurements of the magnetic field with a point source [*Santolík et al.*, 2003]. SVD can also be applied to the electric field of radio emissions by assuming $\mathbf{E}\cdot\mathbf{k} = 0$. Contrary to the three-axial search-coil magnetometers, effective antenna directions and lengths are different from the physical ones due to their electric coupling with the spacecraft body. Therefore one has to perform a transformation from the antenna frame into the orthonormal spacecraft system before we apply SVD (see section 4 for details). SVD provides us with a unity vector $\kappa = \mathbf{k}/|\mathbf{k}|$ contained in a column of the $\mathbf{V}^T$ matrix that corresponds to the minimum of the matrix $\mathbf{W}$ of singular values. In other words, SVD yields the direction where $\mathbf{E}$ has the minimum of its variance. For the GP analysis of the solar radio emissions we define the angles θ and ϕ:

$$\begin{aligned} \theta &= \arctan\left(\sqrt{\kappa_1^2+\kappa_2^2}/\kappa_3\right) \quad \text{for } \kappa_3 \geq 0, \\ \theta &= \pi - \arctan\left(\sqrt{\kappa_1^2+\kappa_2^2}/\kappa_3\right) \quad \text{for } \kappa_3 < 0, \\ \phi &= \arctan(\kappa_2/\kappa_1), \end{aligned} \tag{11}$$

where κ_1, κ_2, and κ_3 are the components of the vector κ. As an estimator of the wave polarization we use coherence in the polarization plane calculated by SVD. A spectral matrix is transformed into the polarization plane where we obtain coherence by comparing auto- and cross-spectra products: $|R_{12}|/\sqrt{R_{11}R_{22}}$, where R_{11} and R_{22} are the autopower spectra in the polarization plane, and R_{12} their cross-power spectrum. A zero coherence implies that Stokes parameters Q, U, and V are null. We expect a very low degree of polarization in the case of type III radio bursts. Information about the apparent source size is hidden in the $\mathbf{W}$ matrix containing the axis lengths of the polarization ellipsoid. In an ideal case of an unpolarized radio wave with a point source, the minimum value of $\mathbf{W}$ (w_1) should be zero. Because of the diffusion in the solar wind, the observed radio signal is a superimposition of radio waves spread over a wide apparent source size. The ratio w_1/w_3 (w_3 is the maximum of $\mathbf{W}$) is then nonzero and can yield information about the apparent source size. Figure 2 shows w_1/w_3 as a function of the apparent source size γ. We have used equations (4)–(10) for modeling spectral matrices that well reflect properties of type III radio bursts at long wavelengths. We have assumed an unpolarized emission ($Q = 0$, $U = 0$, $V = 0$). The shape of the source is considered to be uniform. For a point source ($\gamma = 0°$) the polarization ellipsoid changes to an ellipse contained in a single plane and the ratio of its smallest and largest axis of the ellipsoid (w_1/w_3) is zero. On the other hand, the polarization

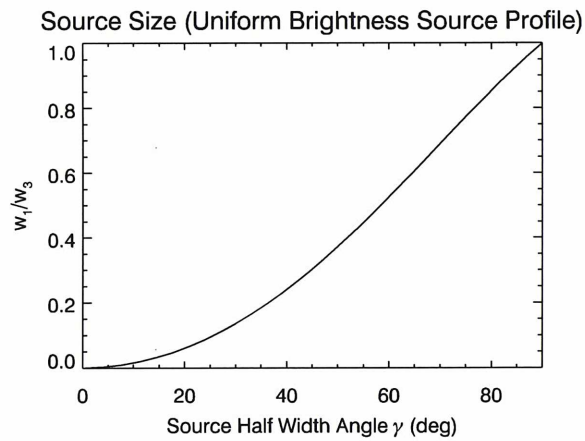

Figure 2. The ratio of the smallest and largest components of the diagonal matrix $\mathbf{W}$ (w_1/w_3) as a function of the apparent source size (γ). A uniform brightness of the source and an unpolarized emission have been assumed.

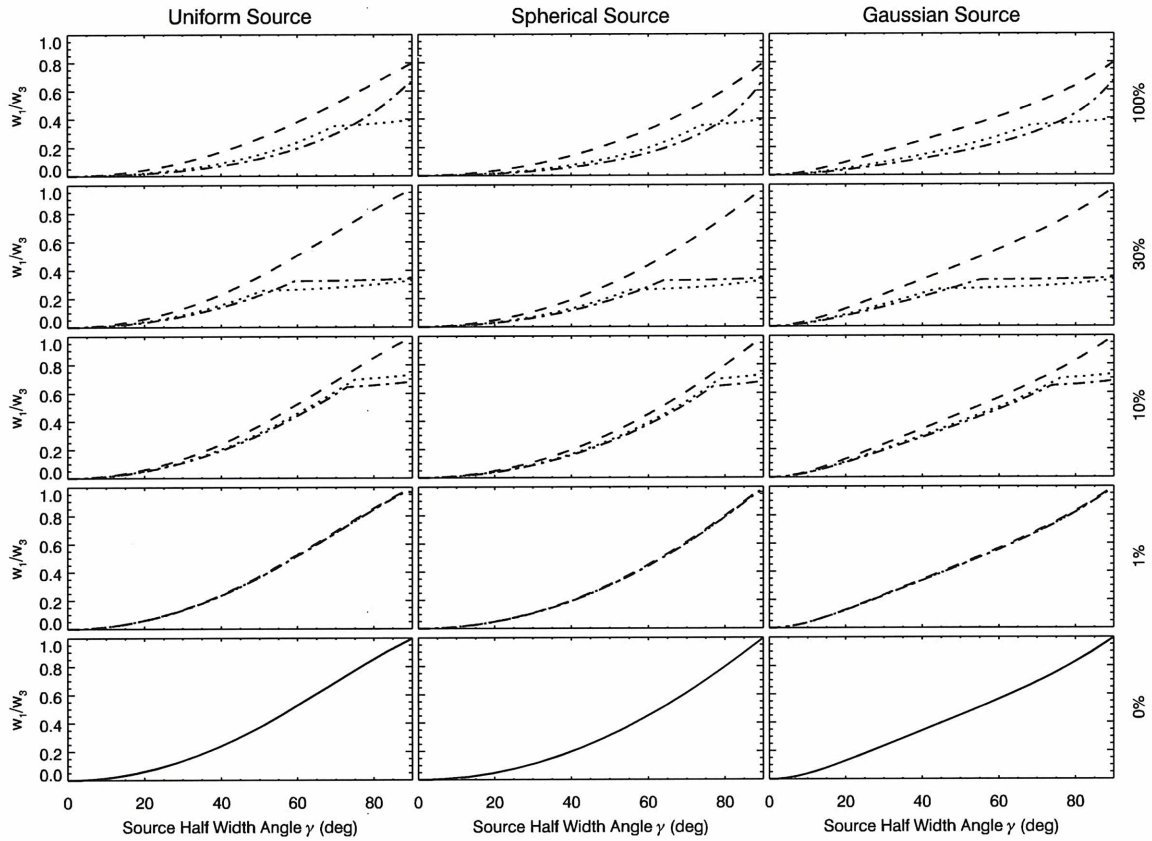

Figure 3. The ratio of the smallest and largest components of the diagonal matrix **W** as a function of the apparent source size (γ) with the assumption of no error of the measurements. Results for (left) uniform, (middle) spherical and (right) Gaussian brightness source profiles are shown. Degree of polarization is 100% (the first row), 30% (the second row), 10% (the third row), 1% (the fourth row) and 0% (the last row). The type of polarization has been considered to be linear (dotted lines), circular (dashed lines), or elliptical (dash-dotted lines). In case of an unpolarized emission a solid line has been used.

ellipsoid of emissions propagating from an half plane ($\gamma = 90°$) becomes a sphere: $w_1/w_3 = 1$.

3. Tests With Simulated Data

[8] Extensive simulations have been performed in order to validate the SVD method for estimating the apparent source size. Equations (4)–(10) have been used for modeling spectral matrices with various types and degrees of polarization computed by decreasing the normalization coefficient of the Stokes parameters (i.e., 100% polarized wave corresponds to $\sqrt{Q^2 + U^2 + V^2} = 1$, while 30% corresponds to $\sqrt{Q^2 + U^2 + V^2} = 0.3$, etc.). The SVD analysis has been applied on these simulated matrices. Figure 3 shows w_1/w_3 for three shapes of the source (in columns: uniform, spherical and Gaussian) and five degrees of polarization (in rows: 100%, 30%, 10%, 1% and 0%) as a function of the apparent source size. We have investigated three possible types of polarization: the linear polarization (dashed line: 100%: $Q = \sqrt{2}/2$, $U = \sqrt{2}/2$, $V = 0$), the right-handed circular polarization (dotted line: 100%: $Q = 0$, $U = 0$, $V = 1$) and the elliptical polarization (dashed dotted line: 100%: $Q = \sqrt{3}/3$, $U = \sqrt{3}/3$, $V = \sqrt{3}/3$). A solid line in the last row refers to unpolarized emissions. When the degree of polarization is significant (>10%), the estimated apparent source size depends on the type of polarization. This dependence disappears if the degree of polarization is negligible. Deviations between particular source shapes are minor.

[9] The obtained empirical formulas can also be efficiently described as a 4th order polynomial regression with the independent variable as the square root of w_1/w_3:

$$\gamma(^\circ) = a_0 + a_1\sqrt{\frac{w_1}{w_3}} + a_2\left(\frac{w_1}{w_3}\right) + a_3\left(\sqrt{\frac{w_1}{w_3}}\right)^3 + a_4\left(\frac{w_1}{w_3}\right)^2, \tag{12}$$

where a_k are coefficients given in Table 1 for a case of an unpolarized wave that corresponds to the last row of

Table 1. Coefficients of a Polynomial Regression for a Case of an Unpolarized Wave for Equation (12)

a_k	Uniform	Spherical	Gaussian
a_0	0.20	−0.01	−0.42
a_1	75.51	90.35	60.30
a_2	32.70	2.86	−80.3
a_3	−67.62	−12.85	240.53
a_4	48.79	9.61	−129.53

Figure 3. Equation (12) has been used to determine γ in the following section.

4. Analysis of a Single Type III Radio Burst Observed Simultaneously by STEREO and *Wind*

[10] STEREO are two nearly identical spacecraft dedicated to stereoscopic investigation of solar processes with varying separation angles with respect to the Sun in the ecliptic plane [*Kaiser et al.*, 2008]. Whereas STEREO-A moves ahead of the Earth in its orbit, STEREO-B trails behind. Both spacecraft are three axis stabilized and embarking the S/Waves instrument [*Bougeret et al.*, 2008]. The High Frequency Receiver (HFR, a part of S/Waves) provides us with GP data between 125 kHz and 1975 kHz in 38 separated bands with a 25 kHz effective bandwidth. This frequency range is well adapted to interplanetary type III radio bursts observations. HFR is a sweeping receiver with two channels from which auto- and cross-correlations are produced a posteriori. Its time resolution is about 30 s per sweep between all frequencies and antenna configurations. Three mutually orthogonal monopole antenna elements (each 6 meters in length) form the sensor part of the S/Waves instrument [*Bale et al.*, 2008]. The effective antenna lengths and directions are different from the physical ones and can be modeled by computer simulations, estimated by rheometric measurements [*Macher et al.*, 2007; *Rucker et al.*, 2005; *Oswald et al.*, 2009], or obtained by an in-flight calibration. We use the in-flight calibration using observations of the Auroral Kilometric Radiation (AKR) by STEREO-B (M. Panchenko, unpublished data, 2010). These directions are slightly different from the the w/base caps (Graz) effective antenna directions (see bottom row of *Bale et al.* [2008, Figure 14]). The used antenna directions can be found in the auxiliary material of this article.[1] As no AKR has been observed by STEREO-A during the calibration period, the effective antenna directions are assumed to be the same. The galactic background radiation has been used to determine the effective antenna lengths [*Zaslavsky et al.*, 2011].

[11] In order to validate our GP technique, we have compared the STEREO observations with those obtained by *Wind* (located in the solar wind). Indeed this latter spacecraft which is now operating for more than 15 years can be considered to be well calibrated. The Waves instrument on-board *Wind* provides us with GP data in a frequency range from 20 up to 1040 kHz with a 3 kHz effective bandwidth [*Bougeret et al.*, 1995]. For the GP analysis with *Wind*/Waves specific methods have been developed for spinning spacecraft [*Manning and Fainberg*, 1980; *Hoang et al.*, 1981]. These techniques provide highly accurate GP measurements using the spacecraft spin demodulation. We have considered the standard deviation of the *Wind* GP data to be 2° for the **k**-vector direction as well as for the apparent source size γ (S. Hoang, personal communication, 2010).

[12] Figures 4 and 5 show results from STEREO-A and STEREO-B, respectively. A separation angle of STEREO-A and STEREO-B with Earth was 4.83° and 2.30° in the ecliptic plane. Both spacecraft observed an intense type III radio burst from 22:53 to 23:09 UT on May 8, 2007. It was a first intense type III radio burst recorded after both STEREO started to operate in the GP mode. To define the spacecraft positions we have used the Heliocentric Earth Ecliptic (HEE) coordinate system, which is centered on the Sun, X being the Sun-Earth line and Z pointing toward the North pole of the ecliptic. STEREO-A was located at $[0.96, 0.08, 0.00]_{HEE}$ AU, whereas STEREO-B was at $[1.05, -0.04, -0.01]_{HEE}$ AU. Figures 4a and 5a display the intensity of electric field fluctuations in Solar Flux Units (1 sfu = 10^{-22} W^2/m^2/Hz). An intensity threshold of 5×10^3 sfu has been applied to the following figures in order to suppress background and to have a good signal to noise ratio for the GP analysis. Figures 4b and 5b show the coherency in the plane of polarization calculated by the SVD. For direction finding analysis we have used Radial-Tangential-Normal (RTN) coordinates: the X axis points from the spacecraft to Sun center, the Y axis is the cross product of the solar rotational axis and X, and lies in the solar equatorial plane (toward the West limb). The observed type III radio burst propagates roughly in the ecliptic plane ($\theta = 90°$), as can be seen in Figures 4c and 5c containing the polar angle θ. The azimuthal angle ϕ is displayed in Figures 4d and 5d. The estimated apparent source size γ is contained in the Figures 4e and 5e. Figure 6 shows the same event recorded at the 925 kHz (916 kHz for *Wind*) frequency channel from both STEREO and *Wind* (located at $[0.99, 0.00, 0.00]_{HEE}$ AU, i.e., roughly between the two STEREO). The plotted error bars for STEREO are obtained from Figures 7 and 8 with a receiver gain of 0.5 dB error (see Appendix A). The plotted error bars of the *Wind* GP data correspond to the standard deviation of 2°. Second and third rows contain the polar angle θ and the azimuth angle ϕ, respectively. Dashed lines represent the direction to the Sun. The last row contains the apparent source γ with the assumption of a uniform source brightness distribution. Dotted lines indicate values corresponding to the maximum flux at the given spacecraft. As can be seen in Figure 6, we have achieved a good agreement between STEREO and *Wind*: the estimated apparent source size γ is $\sim 20°$ on all three spacecraft. Table 2 contains results of the same analysis applied on intense type III radio bursts observed in May 2007, when separation angles between all spacecraft were below 12°.

5. Discussion and Conclusion

[13] The two STEREO spacecraft provide a great opportunity for stereoscopic observations of solar radio emissions at long wavelengths. The *Wind* spacecraft, located roughly between them, is ideal for complementary measurements. The S/Waves instruments on-board STEREO provide GP

[1] Auxiliary material data sets are available at ftp://ftp.agu.org/apend/ja/2011ja017333. Other auxiliary material files are in the HTML. doi:10.1029/2011JA017333.

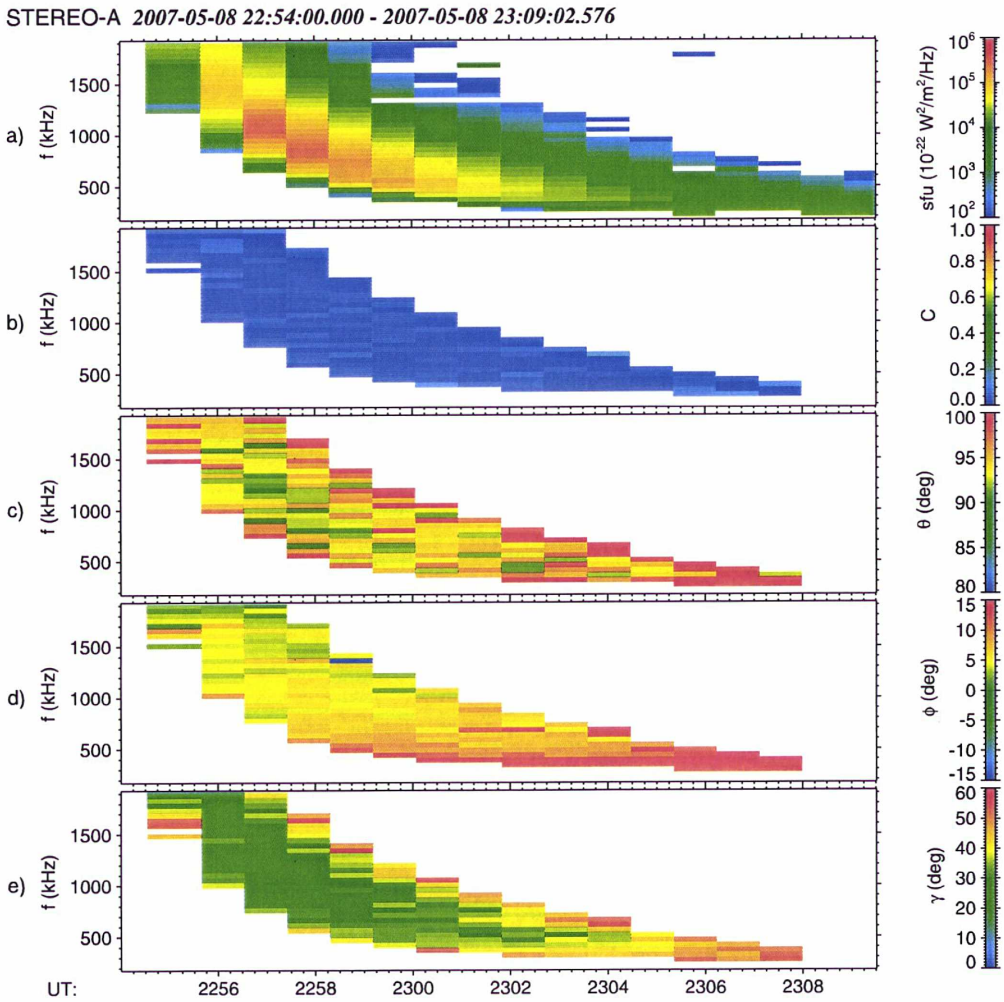

Figure 4. From 22:53 to 23:09 UT on 8 May 2007: (a) the electric field spectral density, (b) the coherence, (c) the polar angle θ, (d) the azimuthal angle ϕ, and (e) the apparent source size γ for STEREO-A.

data that allow to retrieve the **k**-vector direction and polarization properties. An analysis of three type III radio bursts recorded by both STEREO and *Wind*, and using different methods than in this paper, has been done by *Reiner et al.* [2009]. Preliminary results of an application of SVD to measurements of emissions with very extended sources has been recently published by *Krupar et al.* [2010]. Results of a triangulation of radio sources can be also compared with the coronagraph images [*Howard et al.*, 2008; *Martínez Oliveros et al.*, 2012]. A combination of a suitable separation angle between two spacecraft (a triangulation works best for 40°–60°) and the increased solar activity (when more phenomena may be observed) will be reached in 2014. GP capabilities of STEREO may improve our understanding of generation mechanisms of type II and type III radio bursts.

[14] The main result of the paper is the GP inversion using SVD of a signal measured on non-orthogonal antennas with a focus on investigating type III radio bursts at long wavelengths, which have very extended sources and a low degree of polarization. This is the first time that such a technique is applied for a three axis stabilized spacecraft. In section 2 we have obtained an empirical relation between the decomposed spectral matrices, that contains lengths of the polarization ellipsis, and the apparent source sizes for unpolarized emissions with a uniform source shape (Figure 2). For a point source ($\gamma = 0°$) the polarization ellipsoid degenerates to an ellipse ($w_1/w_3 = 0$), whereas for a very extended source ($\gamma = 90°$) it becomes a sphere ($w_1/w_3 = 1$).

[15] An extensive study of various types and degrees of polarization has been performed in section 3. A uniform, spherical and Gaussian source profiles have been considered (Figure 3). We have shown that the empirical relations for these particular shapes of source brightness are similar. If the degree of polarization is below 10% then the differences between the various types of polarization vanish. Otherwise one has to identify the type of polarization in order to apply the appropriate empirical relation.

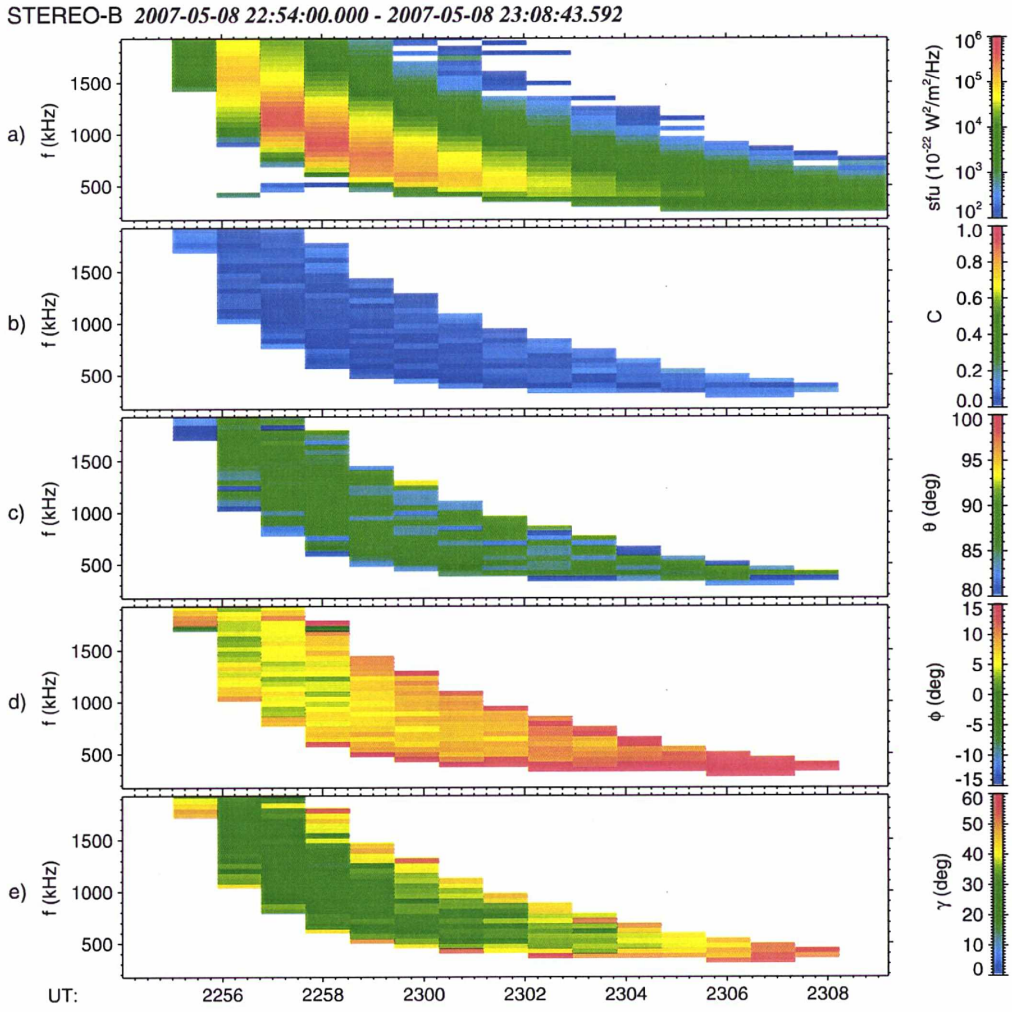

Figure 5. From 22:53 to 23:09 UT on 8 May 2007: (a) the electric field spectral density, (b) the coherence, (c) the polar angle θ, (d) the azimuthal angle ϕ, and (e) the apparent source size γ for STEREO-B.

[16] As an example we present an observation of a type III radio burst obtained simultaneously by the two STEREO and *Wind* spacecraft during small separation distances. Figures 4b and 5b which display the coherency show that the observed type III radio burst has almost no polarized part, as expected at these wavelengths. The type III radio burst propagates roughly in the ecliptic plane (θ = 90°, see Figures 4c and 5c) and eastward from the Sun (ϕ > 0°) accordingly to the Parker spiral geometry (see Figures 4d and 5d). For higher frequencies the radio source is located roughly in the Sun direction, whereas the source moves eastward as the frequency decreases (see Figures 4d and 5d). Scattering effects due to density fluctuations of the solar wind are more significant for lower frequencies. The apparent source sizes vary between 20° and 40° on both spacecraft (see Figures 4e and 5e) with a slight increase of gamma for lower frequencies. The time and frequency center core of the burst has smaller γ than its surrounding.

[17] Figure 6 shows results for the same event from the 925 kHz (916 kHz for *Wind*) frequency channel. Errors induced by the uncertainty on the HFR receiver gain have been taken into account (see Appendix A). We can distinguish an intense peak at 22:58 (the first row of Figure 6). The measured fluxes are about the same for both STEREO. We obtain a better agreement in **k**-vector directions at both frequency channels between *Wind* and STEREO-B, within their respective error bars, than between STEREO-A and *Wind*. The apparent source size is shown in the last row. Although a Gaussian source shape would probably better reflect real observations, the parameter γ from *Wind* has been obtained from previously processed data considering a uniform source shape (S. Hoang, personal communication, 2010). During the maximum of intensity the source size calculated by SVD on STEREO is about the same ($\gamma_{925} \sim 20°$) as on *Wind* which is using a different method dedicated for spinning spacecraft. The best agreement

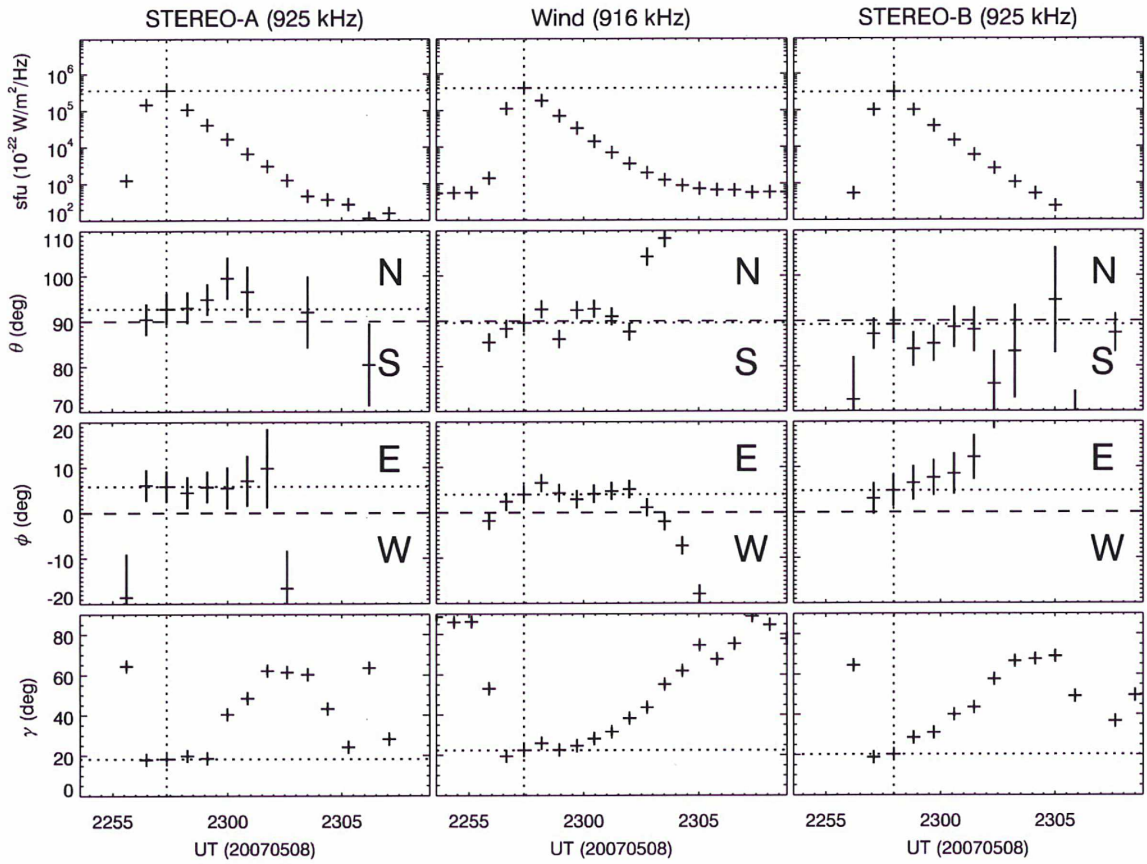

Figure 6. From 22:53 to 23:09 UT on 8 May 2007: the electric field spectral density, the polar angle θ, the azimuthal angle ϕ (in the RTN coordinate system) and the apparent source size γ for STEREO-A (925 kHz), Wind (916 kHz) and STEREO-B (925 kHz). Dashed lines represent the direction to the Sun. Dotted lines indicate values corresponding to the maximum flux at the given spacecraft.

Table 2. Apparent Source Sizes γ Calculated for Six Intense Type III Radio Bursts From May 2007 During Peak Fluxes[a]

$Time_{STEREO-A}$	f_{STEREO} (kHz)	f_{Wind} (kHz)	$\gamma_{STEREO-A}$ (deg)	γ_{Wind} (deg)	$\gamma_{STEREO-B}$ (deg)
2007-05-08T23:07:47.459	225	224	35.67	41.30	49.06
2007-05-08T22:58:10.809	625	624	17.28	24.30	22.68
2007-05-08T22:57:20.523	925	916	18.28	22.50	20.20
2007-05-15T15:46:29.454	225	224	52.12	39.10	57.18
2007-05-15T15:39:30.276	625	624	21.16	25.30	11.75
2007-05-15T15:37:49.166	925	916	24.33	23.90	24.41
2007-05-19T13:11:22.259	225	224	35.07	33.90	25.13
2007-05-19T12:57:26.010	625	624	24.69	24.90	14.10
2007-05-19T12:56:37.721	925	916	17.09	23.80	23.47
2007-05-22T14:37:42.407	225	224	42.58	49.00	43.09
2007-05-22T14:31:38.545	625	624	24.74	24.50	16.71
2007-05-22T14:30:47.751	925	916	19.57	23.70	14.51
2007-05-23T07:35:03.647	225	224	44.91	34.90	37.43
2007-05-23T07:23:39.854	625	624	23.54	23.70	22.73
2007-05-23T07:22:51.070	925	916	21.03	19.90	11.78
2007-05-30T20:44:02.645	225	224	45.94	45.40	50.13
2007-05-30T20:36:13.137	625	624	21.51	28.20	17.73
2007-05-30T20:34:30.031	925	916	19.96	24.00	11.67

[a]The first column corresponds to peak fluxes observed by STEREO-A. A VOTable formatted version is available in the auxiliary material (see Data Set S1).

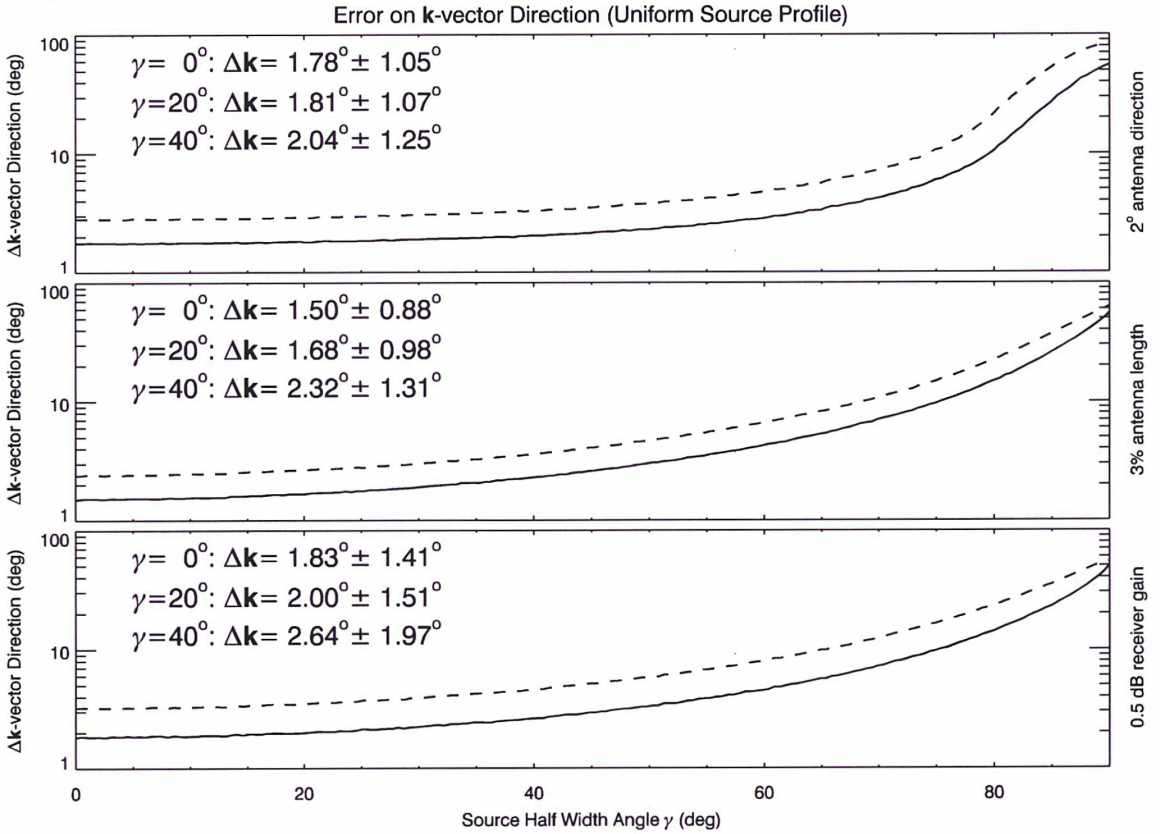

Figure 7. An average angle difference between an input **k**-vector direction and the obtained one by SVD as a function of the apparent source size γ is represented by a solid line, a dashed line is the average plus its standard deviation. (top) An inaccuracy of effective antenna directions of 2°; (middle) an inaccuracy of effective antenna lengths of 3%; (bottom) an uncertainty on the receiver gain of 0.5 dB.

between STEREO and Wind is achieved during a peak flux since the polarization is nearly zero (an initial assumption of the empirical relation in this paper) and the signal-to-noise ratio is relatively high. It confirms the validity of our empirical relation for estimating the apparent source size. Other case studies of joint STEREO and *Wind* observations with small separation distances give similar results (see Table 2). We have obtained a better agreement for the first three events. One should note here that the effective bandwidth of both STEREO is 25 kHz whereas *Wind* has 3 kHz only. It indicates that the SVD method we use and the empirically derived relations can be used for type III radio bursts GP observations. This method can either be used for statistical studies where one needs a robust and fast data processing or for the estimation of initial values that can be used for a more complete GP method using a standard nonlinear χ^2 fitting.

[18] Our study leads us to the following conclusions: 1. We have demonstrated that the SVD allows to directly retrieve the **k**-vector direction from electric field measurements in the case of type III radio bursts. 2. We have found the empirical relation between the decomposed spectral matrices and the apparent source sizes for unpolarized radio emissions with a special focus on type III radio bursts observed by STEREO; 3. Other possible degrees and types of polarization have been also studied with our method and we have shown that below 10% of polarized part it is not necessary to distinguish the type of polarization; 4. Finally one should note that such GP method will also be implemented on the Radio Plasma Waves instrument [*Boudjada et al.*, 2005] on-board the Solar Orbiter spacecraft which, as STEREO, will be three-axis stabilized.

Appendix A: Error Analysis on the Estimation of the Wave Vector Direction and Apparent Size

[19] We have investigated the influence of several possible errors that can affect the current GP inversion applied to Type III bursts. We have performed an error analysis taking into account inaccuracies of the effective antenna directions (2°) and lengths (3%) and an uncertainty on the receiver gain (0.5 dB). The amplitudes of these errors correspond to values estimated from properties of the S/Waves HFR receiver which has been used in section 4 for a demonstration of our analysis. We have simulated antenna directions with normal distributions of absolute deviations centered on the nominal direction with sigma of 2°, and uniform distributions of azimuth. We have also applied the Gaussian noise with a standard deviation of 3% on antenna lengths. As another source of an error an uncertainty on the receiver gain

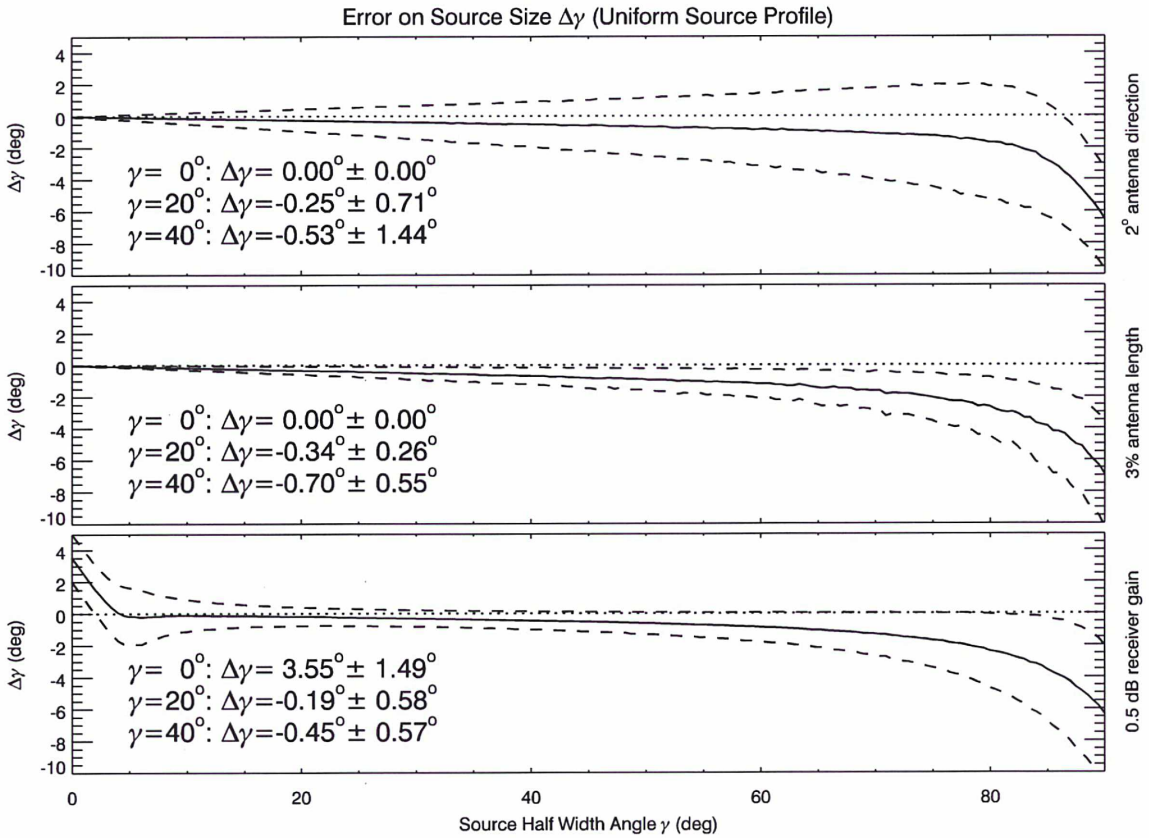

Figure 8. An average angle difference between an input γ and the obtained one by SVD as a function of the apparent source size γ is represented by a solid line, a dashed line is the average plus/minus its standard deviation. First row: an inaccuracy of effective antenna directions of 2°; Second row: an inaccuracy of effective antenna lengths of 3%; Third row: an uncertainty on the receiver gain of 0.5 dB.

has been considered when we have applied the Gaussian noise on the final auto/cross-correlation products (normal distributions of the uncertainties in dB centered at 0 dB). Figure 7 shows an angle difference between an input **k**-vector direction and an output one obtained by SVD as a function of the apparent source size with an assumption of the errors mentioned above. As γ is larger the uncertainty of estimation of the **k**-vector direction increases, as it has been expected. Figure 8 contains an angle difference between an input γ and an output one obtained by SVD (the empirical relation) as a function of the apparent source size. For small sources ($\gamma < 5°$) the empirical relation overestimates the source size. On the other hand, the empirical relation underestimates the source size for large sources ($\gamma > 60°$). Regarding Figures 7 and 8 we conclude that the largest influence that can affect our measurements is an uncertainty on the receiver gain. Therefore it has been considered as a main source of errors in the paper.

[20] **Acknowledgments.** The authors thank Pierre-Luc Astier and Quynh Nhu Nguyen (from LESIA) for providing the S/Waves data and useful engineering insights on the receiver functions. The present work was supported by a scholarship from the French government, grants KONTAKT ME9107, GACR P205102279, and GACR P209122394. The French sub-systems of the S/Waves experiment have been built by LESIA with the support from both CNES and CNRS. M. Panchenko acknowledges the Austrian Fond zur Foerderung der wissenschaftlichen Forschung (FWF project P20680-N16).

[21] Philippa Browning thanks the reviewers for their assistance in evaluating this paper.

References

Bale, S. D., et al. (2008), The electric antennas for the STEREO/WAVES experiment, *Space Sci. Rev.*, *136*, 529–547, doi:10.1007/s11214-007-9251-x.

Bonnin, X., S. Hoang, and M. Maksimovic (2008), The directivity of solar type III bursts at hectometer and kilometer wavelengths: Wind-Ulysses observations, *Astron. Astrophys.*, *489*, 419–427, doi:10.1051/0004-6361:200809777.

Boudjada, M. Y., W. Macher, H. O. Rucker, and G. Fischer (2005), Solar orbiter: Physical aspects towards a better knowledge of the solar corona, *Adv. Space Res.*, *36*, 1439–1443, doi:10.1016/j.asr.2005.05.118.

Bougeret, J.-L., et al. (1995), Waves: The radio and plasma wave investigation on the Wind spacecraft, *Space Sci. Rev.*, *71*, 231–263, doi:10.1007/BF00751331.

Bougeret, J. L., et al. (2008), S/WAVES: The radio and plasma wave investigation on the STEREO mission, *Space Sci. Rev.*, *136*, 487–528, doi:10.1007/s11214-007-9298-8.

Cairns, I. H., and P. A. Robinson (1995), Ion acoustic wave frequencies and onset times during type III solar radio bursts, *Astrophys. J.*, *453*, 959–972, doi:10.1086/176456.

Cecconi, B. (2007), Influence of an extended source on goniopolarimetry (or direction finding) with Cassini and Solar Terrestrial Relations

Observatory radio receivers, *Radio Sci.*, *42*, RS2003, doi:10.1029/2006RS003458.

Cecconi, B., et al. (2008), STEREO/waves goniopolarimetry, *Space Sci. Rev.*, *136*, 549–563, doi:10.1007/s11214-007-9255-6.

Dulk, G. A. (2000), Type III solar radio bursts at long wavelengths, in *Radio Astronomy at Long Wavelengths*, *Geophys. Monogr. Ser.*, vol. 119, edited by R. G. Stone et al., pp. 115–122, AGU, Washington D. C.

Ginzburg, V. L., and V. V. Zhelezniakov (1958), On the possible mechanisms of sporadic solar radio emission (radiation in an isotropic plasma), *Sov. Astron., Engl. Transl.*, *2*, 653–664.

Gurnett, D. A., M. M. Baumback, and H. Rosenbauer (1978), Stereoscopic direction finding analysis of a type III solar radio burst: Evidence for emission at $2f_p$, *J. Geophys. Res.*, *83*, 616–622, doi:10.1029/JA083iA02p00616.

Hoang, S., J. L. Steinberg, R. G. Stone, R. H. Zwickl, and J. Fainberg (1981), The $2f_p$ circumterrestrial radio radiation as seen from ISEE 3, *J. Geophys. Res.*, *86*, 4531–4536, doi:10.1029/JA086iA06p04531.

Howard, R. A., et al. (2008), Sun Earth Connection Coronal and Heliospheric Investigation (SECCHI), *Space Sci. Rev.*, *136*, 67–115, doi:10.1007/s11214-008-9341-4.

Kaiser, M. L., T. A. Kucera, J. M. Davila, O. C. St. Cyr, M. Guhathakurta, and E. Christian (2008), The STEREO mission: An introduction, *Space Sci. Rev.*, *136*, 5–16, doi:10.1007/s11214-007-9277-0.

Kraus, J. D. (1966), *Radio Astronomy*, McGraw-Hill, New York.

Krupar, V., M. Maksimovic, O. Santolik, B. Cecconi, Q. N. Nguyen, S. Hoang, and K. Goetz (2010), The apparent source size of type III radio bursts: Preliminary results by the STEREO/WAVES instruments, *AIP Conf. Proc.*, *1216*, 284–287, doi:10.1063/1.3395856.

Ladreiter, H. P., P. Zarka, A. Lecacheux, W. Macher, H. O. Rucker, R. Manning, D. A. Gurnett, and W. S. Kurth (1995), Analysis of electromagnetic wave direction finding performed by spaceborne antennas using singular-value decomposition techniques, *Radio Sci.*, *30*, 1699–1712, doi:10.1029/95RS02479.

Lecacheux, A. (1978), Direction finding of a radiosource of unknown polarization with short electric antennas on a spacecraft, *Astron. Astrophys.*, *70*, 701–706.

Macher, W., T. H. Oswald, G. Fischer, and H. O. Rucker (2007), Rheometry of multi-port spaceborne antennas including mutual antenna capacitances and application to STEREO/WAVES, *Meas. Sci. Technol.*, *18*, 3731–3742, doi:10.1088/0957-0233/18/12/008.

Manning, R., and J. Fainberg (1980), A new method of measuring radio source parameters of a partially polarized distributed source from spacecraft observations, *Space Sci. Instrum.*, *5*, 161–181.

Martínez Oliveros, J. C., C. L. Raftery, H. M. Bain, Y. Liu, V. Krupar, S. Bale, and S. Krucker (2012), The 2010 August 1 type II burst: A CME-CME interaction and its radio and white-light manifestations, *Astrophys. J.*, *748*, 66, doi:10.1088/0004-637X/748/1/66.

Oswald, T. H., W. Macher, H. O. Rucker, G. Fischer, U. Taubenschuss, J. L. Bougeret, A. Lecacheux, M. L. Kaiser, and K. Goetz (2009), Various methods of calibration of the STEREO/WAVES antennas, *Adv. Space Res.*, *43*, 355–364, doi:10.1016/j.asr.2008.07.017.

Reiner, M. J., K. Goetz, J. Fainberg, M. L. Kaiser, M. Maksimovic, B. Cecconi, S. Hoang, S. D. Bale, and J.-L. Bougeret (2009), Multipoint observations of solar type III radio bursts from STEREO and Wind, *Sol. Phys.*, *259*, 255–276, doi:10.1007/s11207-009-9404-z.

Rucker, H. O., W. Macher, G. Fischer, T. Oswald, J. L. Bougeret, M. L. Kaiser, and K. Goetz (2005), Analysis of spacecraft antenna systems: Implications for STEREO/WAVES, *Adv. Space Res.*, *36*, 1530–1533, doi:10.1016/j.asr.2005.07.060.

Santolík, O., M. Parrot, and F. Lefeuvre (2003), Singular value decomposition methods for wave propagation analysis, *Radio Sci.*, *38*(1), 1010, doi:10.1029/2000RS002523.

Steinberg, J. L., S. Hoang, A. Lecacheux, M. G. Aubier, and G. A. Dulk (1984), Type III radio bursts in the interplanetary medium: The role of propagation, *Astron. Astrophys.*, *140*, 39–48.

Steinberg, J. L., S. Hoang, and G. A. Dulk (1985), Evidence of scattering effects on the sizes of interplanetary type III radio bursts, *Astron. Astrophys.*, *150*, 205–216.

Weber, R. R. (1978), Low frequency spectra of type III solar radio bursts, *Sol. Phys.*, *59*, 377–385, doi:10.1007/BF00951843.

Wild, J. P. (1950), Observations of the spectrum of high-intensity solar radiation at metre wavelengths: III. Isolated bursts, *Aust. J. Sci. Res., Ser. A*, *3*, 541–557.

Zaslavsky, A., N. Meyer-Vernet, S. Hoang, M. Maksimovic, and S. D. Bale (2011), On the antenna calibration of space radio instruments using the galactic background: General formulas and application to STEREO/WAVES, *Radio Sci.*, *46*, RS2008, doi:10.1029/2010RS004464.

Appendix B

Coordinate systems

Contents

This appendix contains descriptions of coordinate systems used in the thesis.

B.1 Heliocentric Earth Ecliptic (HEE)

In this coordinate system the X axis points from the Sun's center to the planet Earth while Z being the north pole of the ecliptic plane.

B.2 Heliocentric Earth Equatorial (HEEQ)

The Z axis denotes the solar rotation axis, and the X axis is in the plane containing the Z axis and Earth. When converted to longitude and latitude, this is known as Stonyhurst heliographic coordinates (*Cortie*, 1897).

B.3 Radial-Tangential-Normal (RTN)

The X axis points from Sun's center to the spacecraft, and the Y axis is the cross product of the solar rotational axis and X lying in the solar equatorial plane towards the West limb.

Acknowledgments

Bibliography

Abalde, J. R., M. V. Alves, and A. C.-L. Chian (1998), Nonlinear generation of type III solar radio bursts by the hybrid modulational instability, *Astronomy and Astrophysics*, *331*, L21–L24.

Bale, S. D., et al. (2008), The Electric Antennas for the STEREO/WAVES Experiment, *Space Science Reviews*, *136*, 529–547, doi:10.1007/s11214-007-9251-x.

Bonnin, X. (2008), *Etude stereoscopique de la directivite des sursauts radio solaires de type III aux frequences inferieures a 10 MHz. PhD thesis.*

Bonnin, X., S. Hoang, and M. Maksimovic (2008), The directivity of solar type III bursts at hectometer and kilometer wavelengths: Wind-Ulysses observations, *Astronomy and Astrophysics*, *489*, 419–427, doi:10.1051/0004-6361:200809777.

Boudjada, M. Y., W. Macher, H. O. Rucker, and G. Fischer (2005), Solar Orbiter: Physical aspects towards a better knowledge of the solar corona, *Advances in Space Research*, *36*, 1439–1443, doi:10.1016/j.asr.2005.05.118.

Bougeret, J.-L., et al. (1995), Waves: The Radio and Plasma Wave Investigation on the Wind Spacecraft, *Space Science Reviews*, *71*, 231–263, doi:10.1007/BF00751331.

Bougeret, J. L., et al. (2008), S/WAVES: The Radio and Plasma Wave Investigation on the STEREO Mission, *Space Science Reviews*, *136*, 487–528, doi:10.1007/s11214-007-9298-8.

Cairns, I. H., and P. A. Robinson (1995), Ion Acoustic Wave Frequencies and Onset Times during Type III Solar Radio Bursts, *"Astrophysical Journal"*, *453*, 959, doi:10.1086/176456.

Cecconi, B. (2007), Influence of an extended source on goniopolarimetry (or direction finding) with Cassini and Solar Terrestrial Relations Observatory radio receivers, *Radio Science*, *42*, 2003–+, doi:10.1029/2006RS003458.

Cecconi, B., and P. Zarka (2005), Direction finding and antenna calibration through analytical inversion of radio measurements performed using a system of two or three electric dipole antennas on a three-axis stabilized spacecraft, *Radio Science*, *40*, 3003, doi:10.1029/2004RS003070.

Cecconi, B., et al. (2008), STEREO/Waves Goniopolarimetry, *Space Science Reviews*, *136*, 549–563, doi:10.1007/s11214-007-9255-6.

Cortie, A. L. (1897), Heliographic coordinates of Sun-spots and faculæ on the Stonyhurst drawings, *Monthly Notices of the Royal Astronomical Society*, *57*, 141.

Drummond, W., and D. Pines (1962), Non-Linear Stability of Plasma Oscillations, *Nuclear Fusion*, (3), 1049–1057.

Dulk, G. A. (2000), Type III Solar Radio Bursts at Long Wavelengths, in *Radio Astronomy at Long Wavelengths*, edited by R. G. Stone, K. W. Weiler, M. L. Goldstein, & J.-L. Bougeret , pp. 115–+.

Dulk, G. A., and S. Suzuki (1980), The position and polarization of Type III solar bursts, *Astronomy and Astrophysics*, *88*, 203–217.

Dulk, G. A., M. V. Goldman, J. L. Steinberg, and S. Hoang (1987), The speeds of electrons that excite solar radio bursts of type III, *Astronomy and Astrophysics*, *173*, 366–374.

Ginzburg, V. L., and V. V. Zhelezniakov (1958), On the Possible Mechanisms of Sporadic Solar Radio Emission (Radiation in an Isotropic Plasma), *Soviet Astronomy*, *2*, 653–+.

Golub, G., and C. Van Loan (1996), *Matrix Computations*, Johns Hopkins Studies in the Mathematical Sciences, Johns Hopkins University Press.

Gopalswamy, N., S. Yashiro, M. L. Kaiser, R. A. Howard, and J.-L. Bougeret (2001), Radio Signatures of Coronal Mass Ejection Interaction: Coronal Mass Ejection Cannibalism?, *Astrophysical Journal Letters*, *548*, L91–L94, doi:10.1086/318939.

Gurnett, D. A., M. M. Baumback, and H. Rosenbauer (1978), Stereoscopic direction finding analysis of a type III solar radio burst - Evidence for emission at 2f/p-/, *Journal of Geophysical Research*, *83*, 616–622, doi:10.1029/JA083iA02p00616.

Gurnett, D. A., et al. (2004), The Cassini Radio and Plasma Wave Investigation, *Space Science Reviews*, *114*, 395–463, doi:10.1007/s11214-004-1434-0.

Hoang, S., J. L. Steinberg, R. G. Stone, R. H. Zwickl, and J. Fainberg (1981), The 2f/p/ circumterrestrial radio radiation as seen from ISEE 3, *Journal of Geophysical Research*, *86*, 4531–4536, doi:10.1029/JA086iA06p04531.

Howard, R. A., et al. (2008), Sun Earth Connection Coronal and Heliospheric Investigation (SECCHI), *Space Science Reviews*, *136*, 67–115, doi:10.1007/s11214-008-9341-4.

Kaiser, M. L., T. A. Kucera, J. M. Davila, O. C. St. Cyr, M. Guhathakurta, and E. Christian (2008), The STEREO Mission: An Introduction, *Space Science Reviews*, *136*, 5–16, doi:10.1007/s11214-007-9277-0.

Kallenrode, M.-B. (2004), *Space physics : an introduction to plasmas and particles in the heliosphere and magnetospheres.*

Kerdraon, A., and J.-M. Delouis (1997), The Nançay Radioheliograph, in *Coronal Physics from Radio and Space Observations, Lecture Notes in Physics, Berlin Springer Verlag*, vol. 483, edited by G. Trottet, p. 192, doi:10.1007/BFb0106458.

Kivelson, M. G., and C. T. Russell (1995), *Introduction to Space Physics.*

Kontar, E. P. (2001), Dynamics of electron beams in the solar corona plasma with density fluctuations, *Astronomy and Astrophysics*, *375*, 629–637, doi:10.1051/0004-6361:20010807.

Kraus, J. D. (1966), *Radio astronomy.*

Kraus, J. D., and R. J. Marhefka (2002), *Antennas for all applications.*

Krupar, V., M. Maksimovic, O. Santolik, B. Cecconi, Q. N. Nguyen, S. Hoang, and K. Goetz (2010), The apparent source size of type III radio bursts: Preliminary results by the STEREO/WAVES instruments, in *American Institute of Physics Conference Series, American Institute of Physics Conference Series*, vol. 1216, edited by M. Maksimovic, K. Issautier, N. Meyer-Vernet, M. Moncuquet, & F. Pantellini, pp. 284–287, doi:10.1063/1.3395856.

Krupar, V., M. Maksimovic, O. Santolik, and B. Cecconi (2011), An Influence of Antenna Tilt Angle to the RPW/Solar Orbiter Direction Finding, *Planetary, Solar and Heliospheric Radio Emissions (PRE VII)*, pp. 389–390.

Krupar, V., O. Santolik, B. Cecconi, M. Maksimovic, X. Bonnin, M. Panchenko, and A. Zaslavsky (2012), Goniopolarimetric inversion using SVD: An application to type III radio bursts observed by STEREO, *Journal of Geophysical Research (Space Physics)*, *117*, A06101, doi:10.1029/2011JA017333.

Kurth, W. S., M. M. Baumback, and D. A. Gurnett (1975), Direction-finding measurements of auroral kilometric radiation, *Journal of Geophysical Research*, *80*, 2764–2770, doi:10.1029/JA080i019p02764.

Ladreiter, H. P., P. Zarka, A. Lecacheux, W. Macher, H. O. Rucker, R. Manning, D. A. Gurnett, and W. S. Kurth (1995), Analysis of electromagnetic wave direction finding performed by spaceborne antennas using singular-value decomposition techniques, *Radio Science*, *30*, 1699–1712, doi:10.1029/95RS02479.

Lang, K. R. (2001), *The Cambridge Encyclopedia of the Sun.*

Lecacheux, A. (1978), Direction Finding of a Radiosource of Unknown Polarization with Short Electric Anten- nas on a Spacecraft, *Astronomy and Astrophysics*, *70*, 701.

Lecacheux, A. (2000), The Nançay Decameter Array: A Useful Step Towards Giant, New Generation Radio Telescopes for Long Wavelength Radio Astronomy, in *Radio Astronomy at Long Wavelengths*, edited by R. G. Stone, K. W. Weiler, M. L. Goldstein, and J.-L. Bougeret, p. 321.

Liu, Y. D., et al. (2012), Interactions between Coronal Mass Ejections Viewed in Coordinated Imaging and in situ Observations, *Astrophysical Journal Letters*, *746*, L15, doi:10.1088/2041-8205/746/2/L15.

Macher, W., T. H. Oswald, G. Fischer, and H. O. Rucker (2007), Rheometry of multi-port spaceborne antennas including mutual antenna capacitances and application to STEREO/WAVES, *Measurement Science and Technology*, *18*, 3731–3742, doi:10.1088/0957-0233/18/12/008.

Maksimovic, M., et al. (2007), *A Radio and plasma wave experiment for the Solar orbiter mission, Proceedings of the 2nd Solar Orbiter Workshop, 16 - 20 October 2006, Athens, Greece, ESA SP-641.*

Manning, R., and G. A. Dulk (2001), The Galactic background radiation from 0.2 to 13.8 MHz, *Astronomy and Astrophysics*, *372*, 663–666, doi:10.1051/0004-6361:20010516.

Manning, R., and J. Fainberg (1980), A new method of measuring radio source parameters of a partially polarized distributed source from spacecraft observations, *Space Science Instrumentation*, *5*, 161–181.

Martens, P. C. H., and N. P. M. Kuin (1989), A circuit model for filament eruptions and two-ribbon flares, *Solar Physics*, *122*, 263–302, doi:10.1007/BF00912996.

Martínez-Oliveros, J. C., C. Lindsey, S. D. Bale, and S. Krucker (2012), Determination of Electromagnetic Source Direction as an Eigenvalue Problem, *Solar Physics*, *279*, 153–171, doi:10.1007/s11207-012-9998-4.

Martínez Oliveros, J. C., C. L. Raftery, H. M. Bain, Y. Liu, V. Krupar, S. Bale, and S. Krucker (2012), The 2010 August 1 Type II Burst: A CME-CME Interaction and its Radio and White-light Manifestations, *Astrophysical Journal Letters*, *748*, 66, doi:10.1088/0004-637X/748/1/66.

Melrose, D. B. (1980), The emission mechanisms for solar radio bursts, *Space Science Reviews*, *26*, 3–38, doi:10.1007/BF00212597.

Meyer-Vernet, N., and C. Perche (1989), Tool kit for antennae and thermal noise near the plasma frequency, *Journal of Geophysical Research*, *94*, 2405–2415, doi:10.1029/JA094iA03p02405.

Novaco, J. C., and L. W. Brown (1978), Nonthermal galactic emission below 10 megahertz, *Astrophysical Journal Letters*, *221*, 114–123, doi:10.1086/156009.

Odstrcil, D., and V. J. Pizzo (2009), Numerical Heliospheric Simulations as Assisting Tool for Interpretation of Observations by STEREO Heliospheric Imagers, *Solar Physics*, *259*, 297–309, doi:10.1007/s11207-009-9449-z.

Oswald, T. H., W. Macher, H. O. Rucker, G. Fischer, U. Taubenschuss, J. L. Bougeret, A. Lecacheux, M. L. Kaiser, and K. Goetz (2009), Various methods of calibration of the STEREO/WAVES antennas, *Advances in Space Research*, *43*, 355–364, doi:10.1016/j.asr.2008.07.017.

Panchenko, M., H. O. Rucker, W. Macher, B. Cecconi, T. H. Oswald, and G. Fischer (2010), STEREO/WAVES antennas calibrated by AKR, in *European Planetary Science Congress 2010*, p. 872.

Parker, E. N. (1958), Suprathermal Particle Generation in the Solar Corona., *Astrophysical Journal*, *128*, 677, doi:10.1086/146580.

Priest, E. R. (1984), *Solar magneto-hydrodynamics*.

Priestley, M. (1989), *Spectral Analysis and Time Series*, Probability and mathematical statistics, Academic Press.

Reiner, M. J., M. Karlický, K. Jiřička, H. Aurass, G. Mann, and M. L. Kaiser (2000), On the Solar Origin of Complex Type III-like Radio Bursts Observed at and below 1 MHZ, *"Astrophysical Journal"*, *530*, 1049–1060, doi:10.1086/308394.

Reiner, M. J., K. Goetz, J. Fainberg, M. L. Kaiser, M. Maksimovic, B. Cecconi, S. Hoang, S. D. Bale, and J.-L. Bougeret (2009), Multipoint Observations of Solar Type III Radio Bursts from STEREO and Wind, *Solar Physics*, pp. 100–+, doi:10.1007/s11207-009-9404-z.

Riley, P., J. A. Linker, and Z. Mikić (2001), An empirically-driven global MHD model of the solar corona and inner heliosphere, *Journal of Geophysical Research*, *106*, 15,889–15,902, doi:10.1029/2000JA000121.

Rucker, H. O., W. Macher, G. Fischer, T. Oswald, J. L. Bougeret, M. L. Kaiser, and K. Goetz (2005), Analysis of spacecraft antenna systems: Implications for STEREO/WAVES, *Advances in Space Research*, *36*, 1530–1533, doi:10.1016/j.asr.2005.07.060.

Rucker, H. O., M. Sampl, M. Panchenko, T. Oswal, D. Plettemeier, M. Maksimovic, and W. Macher (2011), Implications of Antenna System Calibration on Spacecraft Design and Radio Data Analysis, *Planetary, Solar and Heliospheric Radio Emissions (PRE VII)*, pp. 475–485.

Sampl, M., H. O. Rucker, T. H. Oswald, D. Plettemeier, M. Maksimovic, and W. Macher (2011), Numerical Simulations of the Solar Orbiter Antenna System RPW ANT, *Planetary, Solar and Heliospheric Radio Emissions (PRE VII)*, pp. 487–494.

Santolík, O., J. S. Pickett, D. A. Gurnett, and L. R. O. Storey (2002), Magnetic component of narrowband ion cyclotron waves in the auroral zone, *Journal of Geophysical Research (Space Physics)*, *107*, 1444, doi:10.1029/2001JA000146.

Santolík, O., M. Parrot, and F. Lefeuvre (2003), Singular value decomposition methods for wave propagation analysis, *Radio Science*, *38*(1), 010,000–1, doi:10.1029/2000RS002523.

Schelkunoff, S. A. (1952), Book Reviews: Antennas: Theory and Practice; Advanced Antenna Theory, *Science*, *116*, 263–264, doi:10.1126/science.116.3010.263.

Schrijver, C. J., and A. M. Title (2011), Long-range magnetic couplings between solar flares and coronal mass ejections observed by SDO and STEREO, *Journal of Geophysical Research (Space Physics)*, *116*, A04108, doi:10.1029/2010JA016224.

Sittler, E. C., Jr., and M. Guhathakurta (1999), Semiempirical Two-dimensional MagnetoHydrodynamic Model of the Solar Corona and Interplanetary Medium, *Astrophysical Journal*, *523*, 812–826, doi:10.1086/307742.

Steinberg, J. L., S. Hoang, A. Lecacheux, M. G. Aubier, and G. A. Dulk (1984), Type III radio bursts in the interplanetary medium - The role of propagation, *Astronomy and Astrophysics*, *140*, 39–48.

Steinberg, J. L., S. Hoang, and G. A. Dulk (1985), Evidence of scattering effects on the sizes of interplanetary Type III radio bursts, *Astronomy and Astrophysics*, *150*, 205–216.

Stone, R. G., et al. (1992), The Unified Radio and Plasma wave investigation, *Astronomy and Astrophysics Supplement Series*, *92*, 291–316.

Sturrock, P. A. (1964), Type III Solar Radio Bursts, *NASA Special Publication*, *50*, 357.

Temmer, M., et al. (2012), Characteristics of Kinematics of a Coronal Mass Ejection during the 2010 August 1 CME-CME Interaction Event, *Astrophysical Journal*, *749*, 57, doi:10.1088/0004-637X/749/1/57.

Thejappa, G., R. J. MacDowall, and M. L. Kaiser (2007), Monte Carlo Simulation of Directivity of Interplanetary Radio Bursts, *Astrophysical Journal*, *671*, 894–906, doi:10.1086/522664.

Vedenov, A., E. Velikhov, and R. Sagdeev (1962), Quasi-Linear Theory of Plasma Oscillations, *Nuclear Fusion*, (2), 465–475.

Vogl, D. F., et al. (2004), In-flight calibration of the Cassini-Radio and Plasma Wave Science (RPWS) antenna system for direction-finding and polarization measurements, *Journal of Geophysical Research (Space Physics)*, *109*, A09S17, doi:10.1029/2003JA010261.

Weber, R. R. (1978), Low frequency spectra of type III solar radio bursts, *"Solar Physics"*, *59*, 377–385, doi:10.1007/BF00951843.

Wild, J. P. (1950), Observations of the Spectrum of High-Intensity Solar Radiation at Metre Wavelengths. III. Isolated Bursts, *Australian Journal of Scientific Research A Physical Sciences*, *3*, 541.

Zaslavsky, A., N. Meyer-Vernet, S. Hoang, M. Maksimovic, and S. D. Bale (2011), On the antenna calibration of space radio instruments using the galactic background: General formulas and application to STEREO/WAVES, *Radio Science*, *46*, RS2008, doi:10.1029/2010RS004464.

Zouganelis, I., M. Maksimovic, N. Meyer-Vernet, S. D. Bale, J. P. Eastwood, A. Zaslavsky, M. Dekkali, K. Goetz, and M. L. Kaiser (2010), Measurements of stray antenna capacitance in the STEREO/WAVES instrument: Comparison of the measured voltage spectrum with an antenna electron shot noise model, *Radio Science*, *45*, RS1005, doi:10.1029/2009RS004194.